Volume 11 | Issue 3 | 2025

Journal of Biomedical Photonics & Engineering

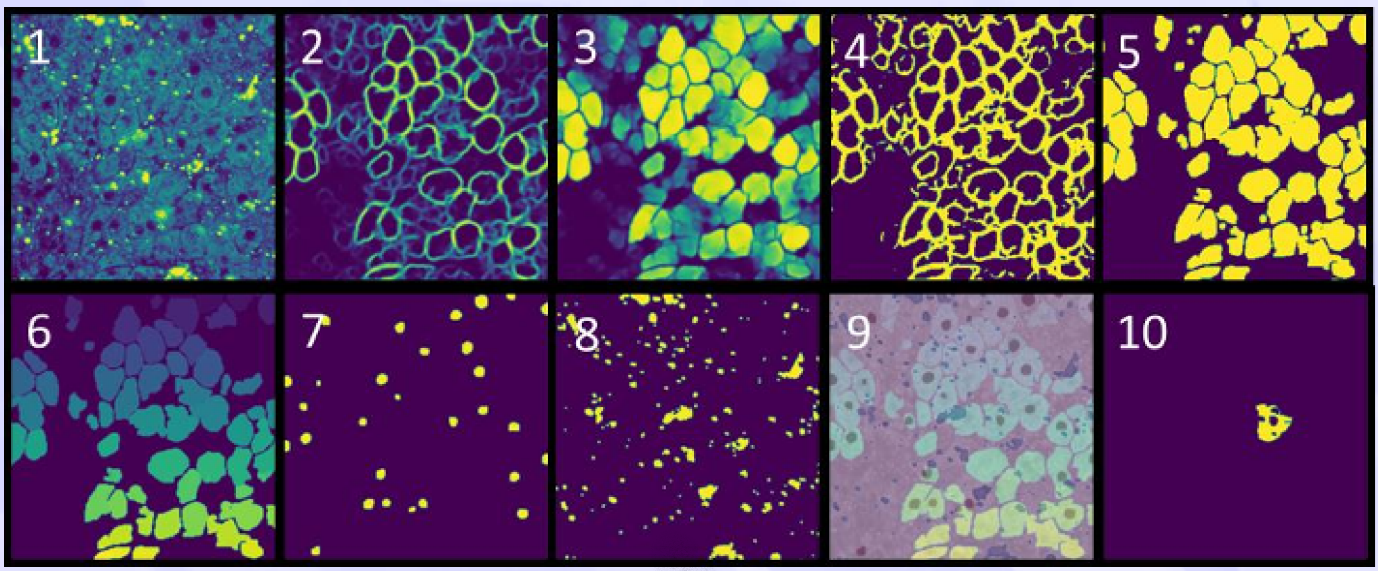

Editor-in-Chief:
V V Tuchin

Journal of Biomedical Photonics & Engineering

by Samara National Research University

Volume 11, Issue 3 (September 2025)

Special Issue
“Advanced Photonic Technologies in Biomedicine”

Used Figures from this issue on the Cover

Ilya Shchechkin et al., Neural Networks for Medical Data Processing: Segmentation of Fluorescence Lifetime Imaging Microscopy, 030304, Fig. 1.

Contents

Articles

Experimental Correction of Arbitrary Instrument Functions in Optical Coherence Tomography Using Only Relative Measurements

Alexander A. Sovetsky, Alexander L. Matveyev, Lev A. Matveev, Peter A. Chizhov, and Vladimir Y. Zaitsev*

A.V. Gaponov-Grekhov Institute of Applied Physics of the Russian Academy of Sciences, 46 Uljanova str., Nizhny Novgorod 603950, Russian Federation

*e-mail: vyuzai@mail.ru

Abstract. One of recent trends in optical coherence tomography (OCT) is the development of various functional modalities beyond straightforward structural imaging. One of such modalities is extraction of optical attenuation coefficient (OAC) from OCT scans. The OAC distributions may be rather informative, however, their extraction from OCT scans can be seriously distorted by the instrument function of OCT setup which may seriously affect the observed depth-dependence of the OCT-signal amplitude. Various procedures for correcting the influence of the instrument function of the OCT setup on the estimated OAC distribution in the sample have been discussed in the literature. To introduce the corresponding correction factors theoretically such procedures, require sufficiently detailed knowledge of the OCT setup parameters. Alternative experimental methods make it possible to obviate the necessity of knowing the OCT-setup parameters, for example, by using a specially prepared calibration phantom with a known value of spatially uniform OAC. In this manuscript we propose an efficient experimental method which is based on exclusively relative measurements, for performing which neither OCT-setup parameters, nor absolute OAC value for the calibration phantom are required. The method makes it possible to correct instrument functions of arbitrary types in either spectral domain or time-domain OCT. Examples of application of the correction method for different OCT-setups are presented to emphasize that the use of uncorrected data may lead to rather strong errors of OAC-distribution estimation in both axial and lateral directions. The proposed method should be helpful to improve the diagnostic accuracy OCT examinations relying on the OAC extraction from OCT data.

Keywords: optical coherence tomography; optical attenuation coefficient; optical attenuation imaging; instrument function.

Paper #9285 received 23 Jun 2025; revised manuscript received 5 Jul 2025; accepted for publication 6 Jul 2025; published online 11 Sep 2025. doi: 10.18287/JBPE25.11.030301.

1 Introduction

One of main trends in Optical Coherence Tomography (OCT) in recent years is the development of new modalities (functional extensions) to complement conventional structural imaging [1]. In particular, such modalities as various realizations OCT-based angiography were developed [2−4], as well as OCT-based variants of elastography [5−8]. Other functional extensions of OCT are based on sophisticated analysis of speckle-pattern parameters (e.g., [9−11]). These modalities allow one to significantly increase the diagnostic value of OCT examinations.

Besides the above-mentioned modalities much attention has also been paid in recent years to the

development of OCT-based methods for estimation of optical attenuation coefficient (OAC) by analyzing the depth dependence of signal intensity in OCT scans (e.g. [12, 13]). The interest to OAC estimation was additionally stimulated in the last decade by study [14], where as elegant approach to reconstruction of depth-resolved OAC distribution was proposed for situations, in which the optical attenuation is dominated by scattering rather than by absorption. The latter situation is quite typical for biological tissues and OCT setups operating in the near-infrared range. Although the optical-signal attenuation for forward propagation of a plane wave in a spatially homogeneous medium is described by a simple exponential factor, estimation of the attenuation coefficient by analyzing the depth-dependence of signals in OCT scans is less trivial, even if it is known that the attenuation is strongly dominated by scattering. The point is that in OCT, besides the energy losses during the forth-and-back light propagation through the scattering tissue, the depth-dependence of the received signal is affected by a number of various factors, first of all, the influence of focusing (which may cause appreciable distortions even for not very large numerical apertures) and the sensitivity fall-off (or roll-off effect) intrinsic to spectral-domain OCT.

Even if the origin of such distortions is qualitatively clear [13−17], purely theoretical derivation of the correcting depth-dependent factors related to the focusing influence, sensitivity roll-off (and other instrument features) is challenging because all required parameters of the used OCT setup usually are not known in detail. As an alternative approach, experimental determining of the correcting depth-dependent factor could be made using a spatially homogeneous reference material with an *a priori* known OAC value. For example, Ref. [18] demonstrated the utilization of such a reference phantom in the form of diffuse-scattering homogeneous suspensions of polystyrene microspheres diluted in distilled water. Their optical properties were calculated using Mie theory for known refractive indices of water and polystyrene, known mean diameter of microspheres and standard deviation, as well as concentration of the microspheres in water. From these data, the scattering coefficient was calculated, the value of which was then compared with the slope of depth dependences of the OCT signal to estimate the correction depth-dependent profile.

Such determining of the correction profile involved more straightforward calculations of the scattering properties of the reference phantom in comparison with the theoretical correction of the instrument function of OCT setup, for which parameters usually are not sufficiently well known if known at all. Yet, even such simpler calculations of phantom scattering properties still require rather detailed knowledge of several parameters to sufficiently accurately predict the OAC for the reference-phantom. In view of this, it would be rather desirable to propose an experimental procedure of finding the correction profile, for which only relative calibration measurements would be sufficient without the necessity to know quantitative scattering properties of the phantom.

In this paper, we describe such a calibration procedure based on exclusively relative measurements and demonstrate its application to real OCT setups. To illustrate the efficiency of the proposed correction procedure, instructive examples are given to demonstrate the difference between the OAC estimates extracted with and without such preliminary calibration procedures.

2 Correction Procedure Principle

Generally speaking, the optical signal attenuation caused by energy losses due to scattering and absorption along the propagation path can be accounted for in a similar manner using exponential factors $\exp(-\mu_a z)$ and $\exp(-\mu_s z)$, where μ_a is the absorption coefficient, μ_s is the scattering coefficient and z is the propagation distance to the depth of the material. For a spatially-inhomogeneous material, the argument of the exponential function has an integral form, $\exp(-\mu_{a,s} z) \to \exp[-\int_0^z \mu_{a,s}) z')]dz'$. However, in OCT the depth-dependence of the received signal is not reduced to the simple exponential form because of the influence of several additional factors. If the intensity of the wave incident on the sample surface is J_0, then the intensity of the received signal can be represented in the following form [14, 18]:

$$I(z) = K \cdot J_0 F(z) S(z) \theta(z) \cdot \mu_s(z) \cdot \cdot \exp\{-2\int_0^z [\mu_s(z') + \mu_a(z')]dz'\}, \quad (2)$$

where coefficient K characterizes the reception sensitivity; function $F(z)$ describes the focusing influence (confocal function); depth-dependence $S(z)$ describes the sensitivity fall-off with increasing depth, which is typical for spectral-domain OCT systems. Function $\theta(z)$ describes the portion of the total scattered radiation propagated back from scatterers and collected over the receiving aperture.

Generally speaking, in biological tissues the optical signal attenuation is caused by combined action of scattering and absorption as in Eq. (2). However, usually the operating wavelength of OCT signals is chosen taking into account the so-called transparency windows of biotissues, in which the attenuation is minimal. In particular, near infra-red range is often chosen for creation OCT devices. For example, an often used wavelength in OCT is 1300 nm, for which numerous independent studies consistently indicate that in biological tissues the optical signal attenuation is strongly dominated by scattering rather that absorption ($\mu_a << \mu_s$), see, e.g., [19−21]. Under this condition for sufficiently small optical paths typical of OCT, in Eq. (2) it may be considered that the influence of absorption can be neglected and the exponential factor

$\exp\{-2\int_0^z[\mu_a(z')]dz'\}\to 1$. Then Eq. (2) reduces to a simpler form

$$I(z)=K\cdot J_0F(z)S(z)\theta(z)\cdot\mu_s(z)\cdot \cdot\exp\{-2\int_0^z\mu_s(z')dz'\}. \quad (3)$$

Then under the additional assumption that prefactor $F(z)S(z)\theta(z)$ in Eq. (3) is depth-independent an elegant method was proposed in Ref. [14] for finding the depth-resolved distribution of $\mu_s(z)$ of arbitrary form in the absence of additive measurement noises and in the case of complete decay of the observed signal intensity $I(z)$ within the visualized region:

$$\mu_s(z)=\frac{I(z)}{2\int_z^\infty I(z')dz'}. \quad (4)$$

However, while the assumptions about $\exp\{-2\int_0^z[\mu_a(z')]dz'\}\to 1$ and the sufficiently strong scattering-induced decay of $I(z)$ within the visualization depth are fairly realistic in OCT, the assumption about depth independence of the instrument-related prefactor $F(z)S(z)\theta(z)=const$ is often appreciably violated and may seriously distort the reconstructed distribution $\mu_s(z)$ based on the use of Eq. (3). Thus, the raw measured dependence $I(z)$ should be somehow corrected to exclude the distorting influence of the depth-dependent prefactor $F(z)S(z)\theta(z)$.

For theoretical correction, the parameters of the OCT setup required to estimate the prefactor $F(z)S(z)\theta(z)$ are often insufficiently well known to the users. A natural alternative may be an experimental calibration method that could be used to find the correction profile $F(z)S(z)\theta(z)$ (in which possibly some other unknown distorting instrumental factors may enter).

At first glance, a good variant could be to perform calibration measurements using a phantom with an *a priori* uniform distribution of the scattering parameter $\mu_s=const$ and negligibly small absorption. In this case Eq. (2) reduces to a simpler form

$$I(z)=K\cdot J_0F(z)S(z)\theta(z)\cdot\mu_s\cdot\exp\{-2\mu_s z\}. \quad (5)$$

However, even if it is known that $\mu_s(z)=const$, still the unknown depth-dependent factor $\exp\{-2\mu_s\cdot z\}$ enters Eq. (5) and prevents the direct estimation of the sought profile $F(z)S(z)\theta(z)$. In view of this in work [18] the authors prepared a special phantom containing scattering microspheres with known optical parameters and concentration to find the factor $\exp\{-2\mu_s\cdot z\}$ by estimating μ_s of the prepared phantom from Mie theory. The advantage of this procedure is that it does not require knowing the OCT-system parameters. However, such a calibration method is rather laborious and requires special qualifications and components to prepare the calibration phantom with well controllable properties.

Thus, it is very desirable to develop an even simpler calibration method which requires neither knowledge of OCT-system parameters, nor parameter μ_s of the calibration sample, so that only relative measurements should be sufficient for determining the depth-dependent calibration profile.

To this end, one has to somehow exclude the unknown exponential factor $\exp\{-2\mu_s z\}$ in Eq. (5), so that purely relative measurements would suffice, even is μ_s is non-zero and unknown. These requirements can be achieved in the following measurement configuration shown in Fig. 1.

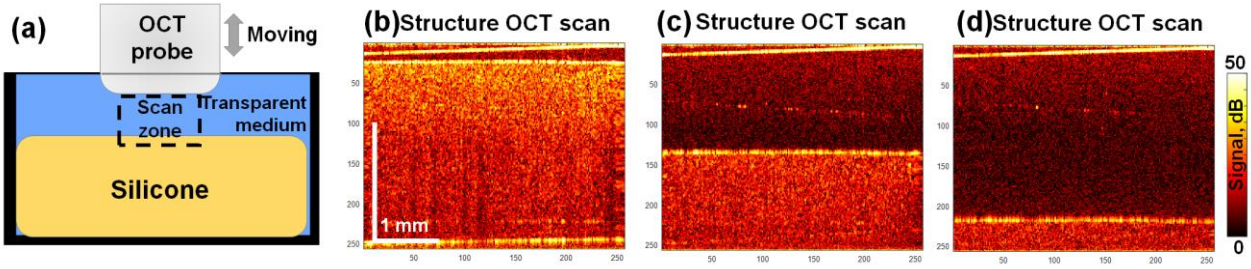

Fig. 1 Configuration of the calibration measurements with a non-scattering immersion medium placed between the OCT probe and the scattering sample, from which only the signal scattered from the near-surface region is analyzed. When the distance between the sample surface and the probe varies, the intensity of this signal is exclusively determined by the sought profile of the instrument function. (a) Schematic of the experiment; (b), (c) and (d) typical experimental scans for various distances between the silicone surface and the OCT probe of a spectral-domain OCT setup. Scans (b), (c) and (d) demonstrate that with increasing distance between the OCT probe and phantom the brightness of the phantom boundary and the near-surface region demonstrate noticeable decrease due to the influence of the sought instrument function.

In this configuration, instead of OCT-signal propagation in the bulk of a spatially uniform medium, it is proposed to acquire the backscattered optical signal from a near-surface layer of a laterally-homogeneous phantom sample. The sample surface should not be strongly scattering/reflecting to avoid the appearance of bright artefacts and overloading of the receiving system. For example, translucent silicones similar to those utilized as reference layers in compression optical coherence elastography [22−24] or sufficiently strongly scattering hydrogels [25] can be used. The sample should be gradually shifted (for example, upward from the bottom of the visualization zone towards the OCT probe) and the depth-dependent brightness of the sample surface should be acquired when the distance to the OCT probe is varied. The medium located above the surface of the gradually moving sample should be optically transparent. Consequently, in this configuration the functional form of the depth-dependent intensity $I_{cal}(z)$ of the received signal is determined exclusively by the sought combination $F(z)S(z)\theta(z)$ entering Eq. (4) before the exponential function. For compactness, this depth-dependent correction profile will be denoted $P_{corr}(z) = F(z)S(z)\theta(z)$. Notice that the pre-exponent depth-dependent multiplier $P_{corr}(z)$ may even comprise some other unknown instrument-dependent factors which would be also accounted for in the measured calibration dependence $I_{cal}(z)$ in the described experimental configuration.

Here, and in the above-presented equations we explicitly discuss only the OCT-probe motion along the axial coordinate *z* for given lateral coordinates. However, it is assumed that the OCT probe itself usually enables scanning in lateral directions (at least along one or both lateral coordinates), so that the described calibration procedures actually enable obtaining of a 2D or 3D map of the depth-dependent correction profiles.

It is important to emphasize an important requirement to such a calibration procedure, namely, the optically transparent medium between the OCT probe and the scattering phantom should have the refractive index close to that of the phantom imitating the biological tissue. Indeed, if the calibration would be performed in the non-absorbing air with $n = 1$, the so-found correction profile in air may noticeably differ from that in biotissues. A fairly good option is to use water with the refractive index $n = 1.33$ which is reasonably close to typical values of the refractive index of biotissues, $n = 1.35-1.4$. If necessary, some other liquid with the refractive index closer to that of biotissues may be used.

After obtaining the calibration dependence $I_{cal}(z)$ for gradually varying depth coordinate *z* (for each lateral coordinate of interest) in the experimental configuration shown in Fig. 1, the calibration profile $P_{corr}(z)$ for given lateral coordinate can be obtained by normalizing the raw dependence $I_{cal}(z)$ to the intensity in the chosen reference point, for example,

$$P_{corr}(z) = I_{cal}(z) / I_{cal}(0) . \qquad (6)$$

Such a calibration procedure does not require knowing the OCT setup parameters, as well as the scattering coefficient μ_s of the scattering phantom.

After dividing any other the intensity profile $I(z)$ described by Eq. (2) by the correction profile given by Eq. (6), $I(z) \to I(z) / P_{corr}(z)$, the depth dependence in Eq. (2) found with an unknown instrument function transforms to a simpler form

$$I_{corr}(z) = \bar{J}_0 \cdot \mu_s(z) \cdot \exp\{-2\int_0^z \mu_s(z')dz'\} , \qquad (7)$$

where $\bar{J}_0$ after such normalization gets somewhat different from the initial J_0 in Eq. (2), which does not prevent finding the unknown μ_s. For example, Vermeer's method [14] can be applied to the corrected profile $I_{corr}(z)$ given by Eq. (7) to find the depth-resolved OAC already cleaned from the distorting influence of the instrument factor.

It should also be noted that even if the immersion layer separating the phantom is non-scattering with $\mu_s \to 0$, still it may exhibit non-negligible absorption $\mu_a \neq 0$. For example, during the calibration the layer of transparent water without any scattering particles may introduce some signal attenuation described by the exponential factor $\exp(-2\mu_a z)$. However, the absorption parameter μ_a for water is well known in the entire optical range [26], as well as in the near infra-red range [27]. For example, according to Ref. [27], for 1.3 μm wavelength often used in OCT, the absorption parameter $\mu_a \approx 0.11$ 1/mm, so that for forth-and-back propagation within 1 mm depth, the absorption-induced reduction in the signal intensity is ~22% or ~0.9 dB, whereas the instrument function of OCT setups often varies by 15−30 dB within the same depth range. Therefore, although the contribution of absorption often may be much smaller than contributions of other factors, if necessary the absorption-related attenuation given by the factor $\exp(-2\mu_a z)$ can readily be introduced in Eq. (7) for the corrected intensity: $I_{corr}(z) \to I_{corr}(z)\exp(2\mu_a z)$.

In the next section we give some examples of utilization of the above described method, as well as compare results of OAC estimation using uncorrected and corrected OCT scans.

3 Experimental Examples of Correction Procedure Utilization

In this section we present results for two types (spectral-domain and time domain) OCT setups designed and produced in the Institute of Applied Physics RAS. Both OCT-setup types have a central wavelength of 1.3 μm, for which in biological tissues the observed attenuation is

strongly dominated by scattering rather than absorption. Consequently, Vermeer's approach [14] can be applied to OCT scans of those setups for obtaining depth-resolved OAC maps.

The first example shown in Fig. 2 is obtained for a spectral-domain OCT setup, for which several examples of OCT scans corresponding to various distances between the reference silicone surface and the OCT probe were shown in Fig. 1(b−d), where the bright slightly inclined line at the top of the scan is the boundary of the output window of the OCT probe. The darker region between the output glass of the probe and silicone surface is filled with immersing water by the above-discussed reasons. It is clear from the presented examples that the brightness of the near-surface region of the silicone phantom gradually decreases with increasing depth of the phantom. This fact is due to the instrument-function influence that we have to compensate. During the calibration measurement, a series of B-scans was acquired when an automated translation device gradually changed the distance between the OCT probe and the phantom. Then in each B-scan similar to those in Fig. 1(a−d) the position of the phantom surface and its intensity was automatically found for every A-scan. Then by combining the so-found positions and intensities of the phantom surface, a pseudo-B-scan was synthesized as shown in Fig. 2(a). Although the silicone was in average fairly uniform, random variations of the near-surface scattering intensity resulted in the appearance of a peculiar vertically-oriented streaky pattern in the synthesized pseudo-B-scan (Fig. 2(a)). Since this streaky structure was unrelated to the instrument-function influence, it was averaged within a sliding window 10×10 pixels in size. The resultant smoothed distribution is shown in Fig. 2(b). The pseudo-B-scan in Fig. 2(b) is subdivided in five vertical stripes with the boundaries marked by different colors. The respective five vertical profiles of OCT-signal intensity determined by the sought instrument function are shown by the corresponding colors in Fig. 2(c). If the instrument function was uniform, the signal intensity would not exhibit depth dependence. Thus, the so-found depth-dependent intensity dependence in each A-scans were used to obtain correction profiles via Eq. (6), for which the 2D map is presented in the color-coded form in Fig. 2(d). Notice that the signal intensity in Fig. 2(a) and 2(b) demonstrates a clear decrease caused by the combined influence of defocusing, the sensitivity roll-off and possibly by other instrument features typical of spectral-domain OCT systems. The total intensity decrease caused by the instrument function and yet unrelated to the signal attenuation reaches 15−20 dB within the visualized depth range (see the individual correction profiles in Fig. 2(c)). After application of the correcting profiles, the raw depth-dependent OCT signals are transformed to the corrected form corresponding to Eq. (7) after which the spatially-resolved maps of the optical attenuation coefficient could be obtained using Vermeer's approach [14]. When necessary, the correction for the presence of noise and incomplete decay of the OCT signal within the visualization depth could be introduced as discussed in Refs. [14, 28].

It is visible in Fig. 2 (especially in Panel (a)) that the trajectories of scatterers look slightly inclined from the vertical direction. This is caused by the slight inclination of the output-glass surface of the OCT probe, which is often introduced in spectral-domain setups to mitigate artefacts caused by light reflections from parallel surfaces of the optical elements of OCT probes. It made no sense to specially correct this small inclination so that the correction profile map in Fig. 4(d) was represented within the rectangular region. It can be noted that some OCT probes may use tilting optical beam for enabling lateral scanning, so that the resultant scans acquire sector shape similar to that for ultrasound medical scans. In the latter case the reconstructed instrument function map would also have a sector shape.

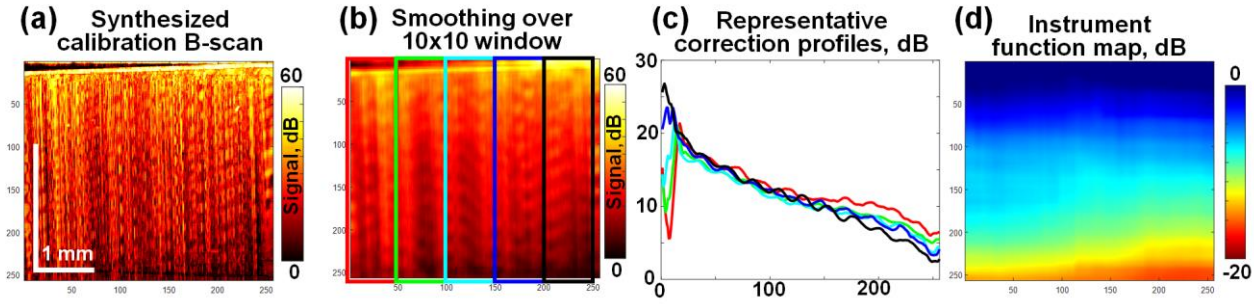

Fig. 2 Application of the calibration procedure to a spectral-domain OCT setup, for which examples of OCT scans are shown in Fig. 1(b−d). Panel (a) shows the synthesized pseudo-B-scan corresponding to the gradually varying distance between the OCT-probe and phantom surface with immersion water layer placed between them as shown in Fig. 1. Panel (b) is the same pseudo-B-scan smoothed using a sliding averaging window 10×10 pixels in size; panel (c) shows 5 representative correction profiles for 5 vertical regions with the boundaries marked by the respective colors; panel (d) is the summarizing 2D map of the so-found correction profiles normalized to the unity value at the surface of the scan using Eq. (6).

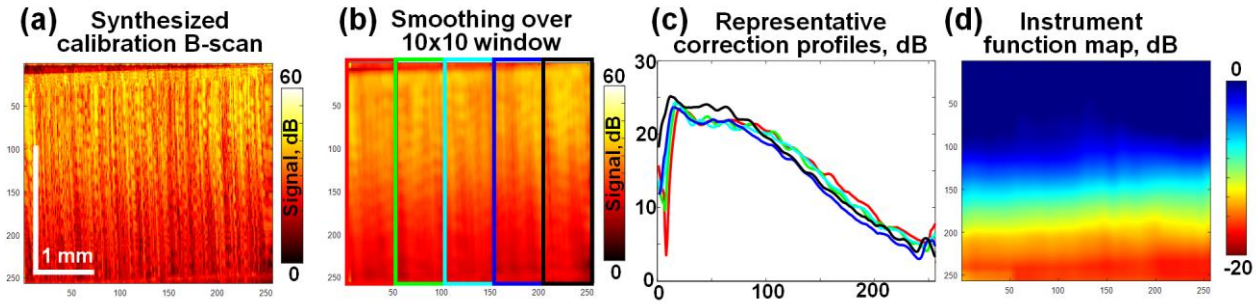

Fig. 3 Application of the calibration procedure to the same spectral-domain OCT setup as in Fig. 2, but preformed in air without the immersion water layer. Panel (a) shows the synthesized pseudo-B-scan corresponding to the gradually varying distance between the OCT-probe and phantom surface in air; (b) the same pseudo-B-scan smoothed using a sliding averaging window 10×10 pixels in size; panel (c) shows 5 representative correction profiles for 5 vertical regions with the boundaries marked by the respective colors in panel (b); (d) the summarizing 2D map of correction profiles normalized to the unity value at the surface of the scan via Eq. (6).

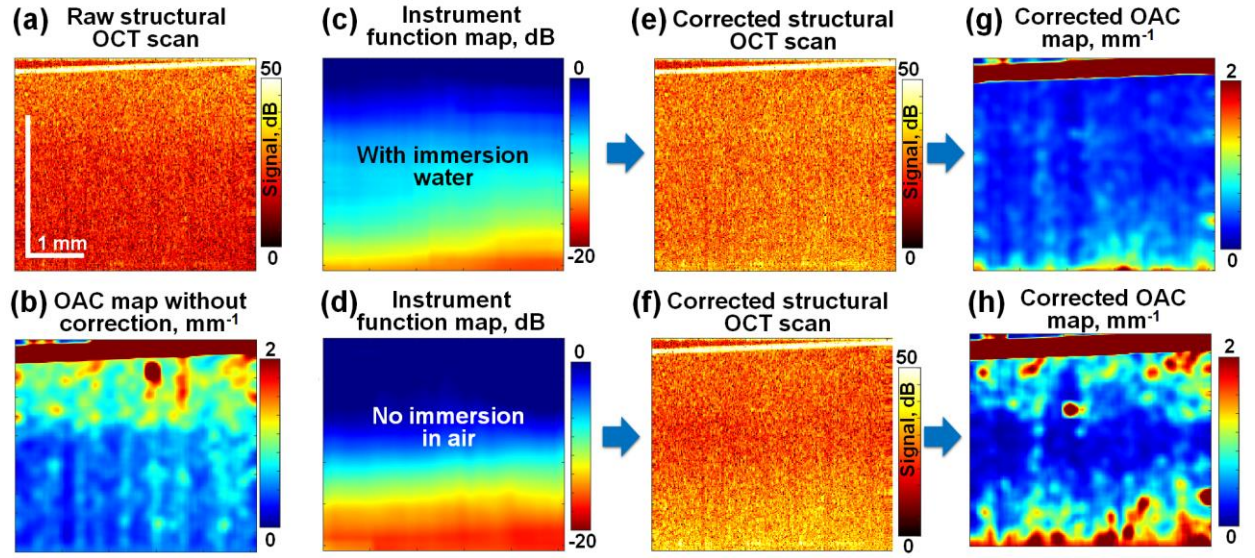

Fig. 4 Comparison of OAC maps derived from scans of a homogeneous silicone sample using the same OCT setup as in Fig. 2 without and with correction for the distorting influence of the instrument function. (a) The raw structural scan; (b) the OAC map derived directly from the initial structural scan without any correction; (c) the map of correction profiles obtained using the immersion water layer above the silicone sample and (d) the correction-profile map obtained for the same silicone phantom in air; (e) and (f) the corrected structural scans for the correction-profile map (c) obtained with immersion water layer and map (d) obtained without immersion in air, respectively; (g) and (h) the corresponding corrected OAC maps.

The next Fig. 3 also shows the results of the calibration procedure for the same OCT setup, but in contrast to Fig. 2 the calibration is performed in air without the immersion water layer between the phantom surface and OCT probe. It is clear that in the absence of the immersion layer the focus depth experienced noticeable axial shift, so that the individual calibration profiles in Fig. 3(c) and the summarizing 2D map of the correction profiles in Fig. 3(d) demonstrate well visible difference from their counterparts in Fig. 2(c) and 2(d).

The comparative results of OAC-map reconstruction without any correction and with application correction-profile maps (instrumental functions) obtained either using the immersion water layer (like in Fig. 2) or in air (like in Fig. 3) are demonstrated in Fig. 4. Figure 4(b) demonstrates that the OAC map found without any correction of the instrument function exhibits well-visible artefactual depth dependence (clearly elevated OAC in the upper part of the scan, although the phantom silicone sample is homogeneous). Figures 4(e) and 4(f) show the structural OCT scans obtained from the raw scan in Fig. 4(a) by applying the correction profiles obtained through the immersion layer (Fig. 4(c)) and in air without immersion (Fig. 4(d)). The corrected scans demonstrate more homogeneous intensity distribution than the raw scan in Fig. 4(a), which means that it is mostly the influence of the instrument function rather than scattering-related losses which caused the $I(z)$ decrease visible in Fig. 4(a) for larger depths. Figure 4(g) derived from the corrected scan from Fig. 4(e) for the

instrument function correctly found with immersion layer demonstrates much more homogenous OAC distribution than the uncorrected OAC map in Fig. 4(b). Finally, Fig. 4(h) shows the OAC map for the incorrect calibration procedure performed in air. In this case the OAC map again shows pronounced artefactual inhomogeneities, although this artefactual inhomogeneity differs from that in Fig. 4(b) obtained without any correction. In all cases in Fig. 4 the OAC maps are reconstructed using the spatially-resolved Vermeer's method (with accounting of noise and incomplete decay [28]). These examples demonstrate high efficiency of the proposed calibration procedure, correctly performed with immersion.

The next example shown in Fig. 5 relates to another OCT system with is time-domain rather than spectral-domain OCT. It has another type of flexible endoscopic probe with a laterally narrower visualization field. The results of utilization of similar calibration procedures are demonstrated in Fig. 5.

Figure 5(a) shows the initial B-scan for the same silicone phantom as in the previous figures. The uncorrected OAC map directly derived from the raw B-scan is shown in Fig. 5(b) with the artefactual elevated OAC-level in the central part of the scan. The correction-profile map obtained though the immersion water layer is shown in Fig. 5(c) and demonstrates pronounced dependence not only in the axial but also in the lateral direction with pronounced right-left asymmetry. The latter fact would be hardly possible to take into account in theoretical expressions but experimentally this complex form of the calibration function is readily reconstructed. The corrected structural OCT scan and the derived OAC map found after application of the instrument function from Fig. 5(c) are shown in Figs. 5(d) and 5(e), respectively. The OAC again is reconstructed using Vermeer's approach with correction for the incomplete decay according to approach [28], the application of this approach is well justified for the used homogeneous sample. As expected, the post-correction OAC distribution in Fig. 5(e) is appreciably more homogeneous in contrast to the uncorrected OAC in Fig. 5(b), where the inhomogeneity of the instrument function results in the appearance of artefactual increased OAC in the vicinity of focal region. Therefore, the presented examples for both spectral-domain and time-domain OCT setups demonstrate the operability and efficiency of the proposed calibration procedures. Moreover, even asymmetric forms of instrument functions can be readily found using the same procedures.

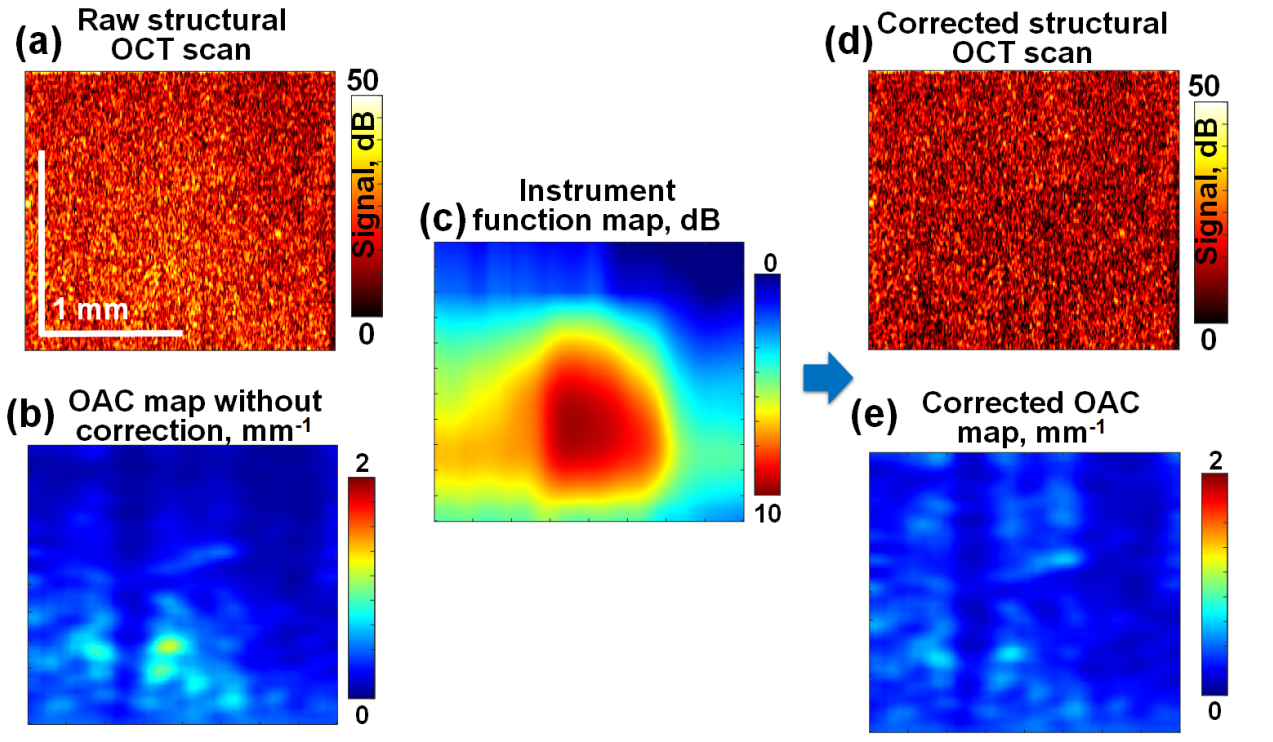

Fig. 5 Demonstration of the correction procedure applied to a time-domain OCT device. (a) The raw B-scan of a spatially homogeneous silicone sample and (b) the reconstructed OAC map based Vermeer's approach [14] (with correction for incomplete signal decay and noise background [28], but without correction for the instrument function). (c) the instrument function reconstructed by the proposed method, (d) corrected structural OCT scan obtained from the initial scan (a) using the instrument function (c); (e) the corrected OAC map, in which the artefactual inhomogeneities of OAC visible in the uncorrected OAC map (d) are significantly suppressed. Notice that in this example for the time-domain OCT the correction profile is increasing at larger depths due to pronounced influence of focusing (see the increased signal intensity in the lower part of panel (a)). This is in contrast to the correction profiles decreasing at larger depths that were shown in Fig. 2 for the spectral domain OCT.

4 Conclusions

In view of rather promising diagnostic prospects, OCT-based estimation of optical attenuation attracts increasing attention of researches. The corresponding studies concern both particular diagnostic applications of OAC in biomedical problems (e.g., [29−31]), as well as further development/perfection of OAC estimation methods [12−15, 18]. Special attention is paid to the adequate accounting and compensation of possible distortions in the reconstructed OAC maps caused by the instrument function of the OCT setup. In particular, the role of OCT-beam focusing and the sensitivity loss (roll-off effect) typical of spectral-domain OCT systems is widely discussed in the literature [12−14]. However, theoretical expressions accounting for the influence of such instrument-related effects require sufficiently complete knowing of the OCT-setup parameters, which is not always possible. In view of this, alternative experimental methods of obtaining correction profiles for OAC estimation are of evident importance. An instructive example is Ref. [18], where the correction profile was determined by utilizing a specially prepared homogeneous phantom with known scattering properties predicted using Mie theory.

However, since creation of phantoms with controllable properties is rather non-trivial and laborious task, it is very desireable to develop a simpler experimental approach, for which absolute values of a phantom sample are not required at all and purely relative measurements are sufficient. In this study we described such a simple but efficient experimental method for obtaining correction profiles to determine the unknown instrument function of OCT setup using only relative measurements. We demonstrated that it can be equally applied to either spectral-domain or time-domain OCT setups. Even insufficiently known construction features of OCT setup resulting in lateral inhomogeneity of the sought depth-dependent correction profiles can also be readily accounted for using the proposed calibration method. Also unknown depth-dependent coefficients (that may be introduced in the OCT setup by the manufactures to improve the visual impression of the ontained scan) would also be eliminated by the described method for correct estimation of OAC. Thus, the proposed approach and above presented demonstrations of its efficiency for improvement of OAC reconstruction from OCT scans should be very beneficial for a broad range of diagnostic applications of multimodal OCT.

Acknowledgement

The study was supported by the Russian Science Foundation (grant No. 22-12-00295-П).

Disclosures

All authors declare that there is no conflict of interest in this paper.

References

1. R. Leitgeb, F. Placzek, E. Rank, L. Krainz, R. Haindl, Q. Li, M. Liu, M. Andreana, A. Unterhuber, T. Schmoll, and W. Drexler, "Enhanced medical diagnosis for dOCTors: a perspective of optical coherence tomography," Journal of Biomedical Optics 26(10), 100601 (2021).
2. A. Mariampillai, B. A. Standish, E. H. Moriyama, M. Khurana, N. R. Munce, M. K. K. Leung, J. Jiang, A. Cable, B. C. Wilson, I. A. Vitkin, and V. X. D. Yang, "Speckle variance detection of microvasculature using swept-source optical coherence tomography," Optics Letters 33(13), 1530 (2008).
3. A. Zhang, Q. Zhang, C.-L. Chen, and R. K. Wang, "Methods and algorithms for optical coherence tomography-based angiography: a review and comparison," Journal of Biomedical Optics 20(10), 100901 (2015).
4. A. Moiseev, S. Ksenofontov, M. Sirotkina, E. Kiseleva, M. Gorozhantseva, N. Shakhova, L. Matveev, V. Zaitsev, A. Matveyev, E. Zagaynova, V. Gelikonov, N. Gladkova, A. Vitkin, and G. Gelikonov, "Optical coherence tomography-based angiography device with real-time angiography B-scans visualization and hand-held probe for everyday clinical use," Journal of Biophotonics 11(10), e201700292 (2018).
5. K. V. Larin, D. D. Sampson, "Optical coherence elastography – OCT at work in tissue biomechanics [Invited]," Biomedical Optics Express 8(2), 1172 (2017).
6. V. Y. Zaitsev, A. L. Matveyev, L. A. Matveev, A. A. Sovetsky, M. S. Hepburn, A. Mowla, and B. F. Kennedy, "Strain and elasticity imaging in compression optical coherence elastography: The two-decade perspective and recent advances," Journal of Biophotonics 14(2), e202000257 (2021).
7. M. A. Kirby, I. Pelivanov, S. Song, Ł. Ambrozinski, S. J. Yoon, L. Gao, D. Li, T. T. Shen, R. K. Wang, and M. O'Donnell, "Optical coherence elastography in ophthalmology," Journal of Biomedical Optics 22(12), 1 (2017).
8. E. V. Gubarkova, A. A. Sovetsky, L. A. Matveev, A. L. Matveyev, D. A. Vorontsov, A. A. Plekhanov, S. S. Kuznetsov, S. V. Gamayunov, A. Y. Vorontsov, M. A. Sirotkina, N. D. Gladkova, and V. Y. Zaitsev, "Nonlinear elasticity assessment with optical coherence elastography for high-selectivity differentiation of breast cancer tissues," Materials 15(9), 3308 (2022).
9. D. Zhu, J. Wang, M. Marjanovic, E. J. Chaney, K. A. Cradock, A. M. Higham, Z. G. Liu, Z. Gao, and S. A. Boppart, "Differentiation of breast tissue types for surgical margin assessment using machine learning and polarization-sensitive optical coherence tomography," Biomedical Optics Express 12(5), 3021 (2021).

10. M. Niemczyk, D. R. Iskander, "Statistical analysis of corneal OCT speckle: a non-parametric approach," Biomedical Optics Express 12(10), 6407 (2021).
11. L. A. Matveev, A. A. Sovetsky, A. L. Matveyev, I. A. Vitkin, M. Assaad, and V. Y. Zaitsev, "Refined speckle contrast estimation in OCT based on compensation of scattering-related distortions of speckle pattern parameters," Laser Physics Letters 22(1), 015601 (2025).
12. S. Chang, A. K. Bowden, "Review of methods and applications of attenuation coefficient measurements with optical coherence tomography," Journal of Biomedical Optics 24(09), 1 (2019).
13. P. Gong, M. Almasian, G. Van Soest, D. M. De Bruin, T. G. Van Leeuwen, D. D. Sampson, and D. J. Faber, "Parametric imaging of attenuation by optical coherence tomography: review of models, methods, and clinical translation," Journal of Biomedical Optics 25(04), 1 (2020).
14. K. A. Vermeer, J. Mo, J. J. A. Weda, et al.H. G. Lemij, and J. F. De Boer, "Depth-resolved model-based reconstruction of attenuation coefficients in optical coherence tomography," Biomedical Optics Express 5(1), 322 (2014).
15. B. Ghafaryasl, K. A. Vermeer, J. Kalkman, T. Callewaert, J. F. De Boer, and L. J. Van Vliet, "Analysis of attenuation coefficient estimation in Fourier-domain OCT of semi-infinite media," Biomedical Optics Express 11(11), 6093 (2020).
16. E. P. Sherstnev, P. A. Shilyagin, D. A. Terpelov, V. M. Gelikonov, and G. V. Gelikonov, "An improved analytical model of a spectrometer for optical coherence tomography," Photonics 8(12), 534 (2021).
17. A. A. Sovetsky, A. L. Matveyev, L. A. Matveev, P. A. Chizhov, and V. Y. Zaitsev, "Simple "Digital Phantom" for testing attenuation-imaging methods in optical coherence tomography," Journal of Biomedical Photonics & Engineering 10(2), 020302 (2024).
18. L. Scolaro, R. A. McLaughlin, B. R. Klyen, B. A. Wood, P. D. Robbins, C. M. Saunders, S. L. Jacques, and D. D. Sampson, "Parametric imaging of the local attenuation coefficient in human axillary lymph nodes assessed using optical coherence tomography," Biomedical Optics Express 3(2), 366 (2012).
19. V. V. Tuchin, D. Zhu, and E. A. Genina (Eds.), "Handbook of tissue optical clearing: new prospects in optical imaging: New Prospects in Optical Imaging," CRC Press, Boca Raton (2021). eBook ISBN: 9781003025252.
20. V. V. Tuchin, "Tissue optics and photonics: light-tissue interaction," Journal of Biomedical Photonics & Engineering 1(2), 98–134 (2015).
21. F. Bergmann, F. Foschum, L. Marzel, and A. Kienle, "*Ex Vivo* determination of broadband absorption and effective scattering coefficients of porcine tissue," Photonics 8(9), 365 (2021).
22. V. Y. Zaitsev, A. L. Matveyev, L. A. Matveev, E. V. Gubarkova, A. A. Sovetsky, M. A. Sirotkina, G. V. Gelikonov, E. V. Zagaynova, N. D. Gladkova, and A. Vitkin, "Practical obstacles and their mitigation strategies in compressional optical coherence elastography of biological tissues," Journal of Innovative Optical Health Sciences 10(06), 1742006 (2017).
23. E. V. Gubarkova, E. B. Kiseleva, M. A. Sirotkina, D. A. Vorontsov, K. A. Achkasova, S. S. Kuznetsov, K. S. Yashin, A. L. Matveyev, A. A. Sovetsky, L. A. Matveev, A. A. Plekhanov, A. Y. Vorontsov, V. Y. Zaitsev, and N. D. Gladkova, "Diagnostic OCT and OCT-Elastography for differentiation of breast cancer subtypes: comparative study," Diagnostics 10(12), 994 (2020).
24. A. A. Sovetsky, A. L. Matveyev, L. A. Matveev, G. V. Gelikonov, and V. Y. Zaitsev, "Mapping large strains in phase-sensitive OCT: Key role of supra-pixel displacement tracking in incremental strain evaluation," Journal of Biomedical Photonics & Engineering 8(3), 030304 (2022).
25. Y. M. Alexandrovskaya, E. M. Kasianenko, A. A. Sovetsky, A. L. Matveyev, and V. Y. Zaitsev, "Spatio-temporal dynamics of diffusion-associated deformations of biological tissues and polyacrylamide gels observed with optical coherence elastography," Materials 16(5), 2036 (2023).
26. C. K. N. Patel, A. C. Tam, "Optical absorption coefficients of water," Nature 280(5720), 302–304 (1979).
27. C.-L. Tsai, J.-C. Chen, and W.-J. Wang, "Near-infrared absorption properties of biological soft tissue constituents," Journal of Medical and Biological Engineering 21(1), 7–14 (2001).
28. J. Liu, N. Ding, Y. Yu, X. Yuan, S. Luo, J. Luan, Y. Zhao, Y. Wang, and Z. Ma, "Optimized depth-resolved estimation to measure optical attenuation coefficients from optical coherence tomography and its application in cerebral damage determination," Journal of Biomedical Optics 24(03), 1 (2019).
29. P. Gong, S. Es'haghian, K.-A. Harms, A. Murray, S. Rea, F. M. Wood, D. D. Sampson, and R. A. McLaughlin, "In vivo label-free lymphangiography of cutaneous lymphatic vessels in human burn scars using optical coherence tomography," Biomedical Optics Express 7(12), 4886 (2016).
30. A. Moiseev, E. Sherstnev, E. Kiseleva, K. Achkasova, A. Potapov, K. Yashin, M. Sirotkina, G. Gelikonov, V. Matkivsky, P. Shilyagin, S. Ksenofontov, E. Bederina, I. Medyanik, E. Zagaynova, and N. Gladkova, "Depth-resolved method for attenuation coefficient calculation from optical coherence tomography data for improved biological structure visualization," Journal of Biophotonics 16(12), e202100392 (2023).
31. A. A. Sovetsky, K. S. Yashin, R. D. Zinatullin, A. L. Matveyev, V. Y. Zaitsev, and L. A. Matveev, "Optical coherence tomography-based in vivo automatic detection of brain tissue malignancy using optical attenuation coefficient and refined speckle contrast: preliminary results," Laser Physics Letters 22(6), 065601 (2025).

Prediction of Automated Evaporation of Soft Biotissues of Different Types by Continuous CO_2 Laser Radiation

Alexander K. Dmitriev, Alexey N. Konovalov*, Vladimir N. Kortunov, and Valery A. Ulyanov
NRC "Kurchatov Institute", 1 Academician Kurchatov Sq., Moscow 123182, Russian Federation
*e-mail: ank27.ift@mail.ru

Abstract. The study of laser evaporation of biological tissues and the creation of computational models of this process is an important scientific task for the development of predictive modeling and preoperative planning approaches in robotic laser surgery. Laser evaporation of soft water-containing biotissues with significantly different structure and strength characteristics was studied in the process of two-coordinate laser scanning of continuous CO_2 laser radiation. Samples of soft tissues from pigs *in vitro* (myocardium, liver, skeletal muscle, aorta) were used. It is shown that the dependence of the laser evaporation depth on the radiation power for these tissues is well approximated by a linear function. The proportionality coefficients between the maximum evaporation depth and the radiation power for all tissues, with the exception of the aorta, practically coincide with the calculated coefficient of 175 μm/W, obtained on the basis of the evaporation model of soft tissue evaporation for scanning parameters: scanning speed v = 15 mm/s, laser beam diameter 180 μm, distance between lines 150 μm. It is shown that despite the strong differences in soft tissue structure and strength characteristics (more than two orders of magnitude), the average deviation of the calculated value of the evaporation depth from the measured value for all tissues is several tens of percent and depends on the excess over the evaporation threshold. The developed approach can be used for predictive modeling in preoperative planning using scanning systems based on continuous CO_2 lasers.

Keywords: CO_2 laser; automated scanning; biotissue; structure; strength characteristics; depth of evaporation; predictive modeling.

Paper #9264 received 6 Apr 2025; revised manuscript received 25 May 2025; accepted for publication 14 Aug 2025; published online 11 Sep 2025. doi: 10.18287/JBPE25.11.030302.

1 Introduction

Robotics in surgery is one of the directions of development of modern medicine [1–3]. It is assumed that robotic surgery will reduce the risks of the human factor and shorten the time of operations, increase the precision of surgical intervention and the effectiveness of treatment, and accelerate postoperative rehabilitation of patients.

One of the tools widely used for high-precision and minimally invasive laser surgeries are CO_2 laser-based devices equipped with scanning systems. Such devices allow for the automation of the laser radiation exposure process [4]. The most common use of such devices is for the so-called ablative (local tissue evaporation) and non-ablative (local tissue heating) laser skin resurfacing [5,6]. Such technology is considered to be the gold standard in dermatological surgery. Currently, active research is being conducted on the use of scanning laser systems in relation to the tasks of obtaining precision cuts of complex shape of a given depth and evaporation of a given area of arbitrary shape on the surface of biotissue. Scanning systems allow precise control of laser radiation parameters in the impact zone. They ensure high speed and accuracy, safety and reproducibility of operations using CO_2 lasers [7]. This significantly expands the possibilities and prospects for their use in surgery.

One of the directions of development of robotic laser surgery is predictive modeling for preoperative planning purposes [8, 9]. This approach is based on experimental and numerical modeling of laser exposure processes using various *in vivo* or *ex vivo* biomodels. In Ref. [10], the selection of modes and prediction of the depth of automated laser incision of soft tissues is proposed to be

carried out on the basis of an experimental database. To create such a database, chicken muscle tissue *ex vivo* was used. In Refs. [11, 12], to obtain a given depth of laser evaporation of soft and bone tissues, it is proposed to use simplified mathematical models for predicting the depth of the cut based on experimental data on animal tissues. In Ref. [13], a 3D model based on a single-layer perceptron network is proposed to predict the creation of a cavity in tissue during laser ablation. Thus, to solve problems of prediction and optimizing laser ablation of biotissues, there is a tendency to use approaches based on experimental databases. This is due to the rapid development of information technologies and various data processing methods, including neural network-based methods. Another reason is the difficulty of direct physical modeling of laser ablation of biotissues. This is due to the fact that various interrelated processes occur in the laser exposure zone: absorption/scattering of radiation, thermal conductivity, chemical processes, explosive boiling, generation of acoustic and shock waves, etc.

Approaches to modeling physical processes during laser ablation of biotissues have been developing over several decades. In Refs. [14, 15], an analysis of laser ablation of soft biotissues by pulsed radiation for different wavelengths is carried out. For assessments, a thermal model is used and the overheating of water in soft tissues is taken into account. In Ref. [15], calculation expressions are given for the threshold intensity of ablation of biotissues and the depth of ablation by a short laser pulse. A logarithmic dependence of the ablation depth on the radiation intensity was obtained. In this work, the literature data on the depth of pulsed ablation of biotissues for different wavelengths are analyzed and compared with the proposed calculation formula. In some cases, good agreement between the experimental data and the calculated dependence was observed. In Ref. [16], the influence of the strength characteristics of soft biological tissues on the efficiency of their ablation by a single CO_2 laser pulse was investigated. *In vitro* tissues of animal myocardium, aorta, liver and skin were used. The water content in these tissues was approximately the same (70−80%), but the tensile strength differed by one to two orders of magnitude (the lowest in the liver, the highest in the skin). A direct relationship has been established between the efficiency of pulsed ablation (mass removal per pulse) and the strength characteristics of these tissues. It has been shown that under conditions significantly exceeding the threshold, the greatest ablation efficiency is in the liver, 3 times less in the myocardium, and 7 times less in the aorta. It is concluded that not only water but also strength properties play an important role in soft tissue ablation with a pulsed CO_2 laser. In Ref. [17], a significant influence of strength properties on the threshold of pulsed laser ablation of soft tissues was theoretically predicted.

It should be noted that the majority of studies are devoted to laser ablation of biotissues in short pulse mode. Such impacts create excess pressure, leading to tissue rupture. In this regard, the strength properties of tissues play an important role in the process of their laser ablation with short pulses. There are far fewer studies that examine the effects of continuous laser radiation on biotissue. Moreover, there are few works that model the cutting depth and the depth of evaporation of the tissue zone during two-dimensional scanning of continuous laser radiation. There is a well-known theoretical work [18], which presents a model of laser ablation of biotissues for continuous radiation with a stationary position of the laser beam. The model is based on thermal conductivity and the energy required for water evaporation. Based on the heat conductivity equation, relationships were obtained for the ablation threshold (when the temperature is equal to the boiling point of water for an exposure time of ∞) for the radiation intensity and exposure time required to begin ablation.

Previously, we proposed a semi-empirical model of laser evaporation of soft biotissues using continuous CO_2 laser radiation during two-coordinate beam scanning [19]. This model showed good agreement with experimental data on the evaporation of model samples based on aqueous solution of agar and samples of pig heart muscle *in vitro*. The model is based on energy balance, assuming that the key factor in energy balance is tissue water evaporation. The paper suggests that the proposed model can be used to predict the evaporation of other soft tissues with high water content during two-dimensional scanning of CO_2 laser radiation.

However, the applicability of the evaporative mechanism of tissue removal by continuous CO_2 laser for different soft tissues has not been definitively substantiated. This is due to the fact that soft tissues, despite similar thermophysical characteristics, have different structures. The different composition of the organic matrix and its structure leads to the fact that the strength properties of soft tissues differ significantly. For example, the tensile strength of soft tissues can differ by more than two orders of magnitude [16, 20, 21], while the maximum difference in thermophysical characteristics is tens of percent. In this regard, the question arises about the applicability of the evaporation model for soft tissues with very different strength characteristics under continuous laser radiation.

The aim of this work is to study the depth of evaporation of soft water-containing biotissues with very different strength characteristics during two-coordinate laser scanning of continuous CO_2 laser radiation, to predict the depth of evaporation based on the evaporation mechanism and to determine the limits of applicability of this approach.

2 Methods and Materials

For automated surface laser evaporation of biomodels, the setup was used, consisting of a laser unit, an articulated-mirror manipulator and a 2- coordinate galvanic scanner JS1105 Galvo Scanner (Sino-Galvo Technology Co., China) coupled to it. The setup is based on a single-mode CO_2 laser C-20A (Coherent, USA) with a power of up to 20 W with high-frequency (HF) pumping of the active medium. A detailed description of the setup is given in Ref. [22].

Table 1 Some characteristics of biological tissues [16, 20, 21, 23−25].

	Thermophysical			Mechanical and structural	
Type of tissue	**Thermal conductivity k, W/m·K**	**Heat capacity C, J/kg·K**	**Density ρ, g/cm^3**	**Tensile strength σ_p, N/mm^2**	**Peculiarities of the structure of biotissue**
Skeletal muscle	0.45	3450	1.04	0.07 (along the fibers)	An aggregate of parallel muscle fibers in connective tissue.
Myocardium	0.71	3730	1.06	0.04	Three-dimensional structure of densely packed muscle fibers.
Liver	0.52	3600	1.06	< 0.04	An aggregate of liver lobules and hepatocytes.
Aorta	0.63	3960	1.04	2	A set of elastic functional shell layers.

The scanner control unit and our specially developed software allowed us to set any shape of the evaporation area within 20 mm × 20 mm, the speed of the laser beam within 1–50 mm/s, and the required filling density of the evaporated surface by laser hatching. The surface scanning area is a set of parallel lines (hereinafter, hatching lines). The required density of filling the evaporated area of the surface by laser hatching was ensured by changing the distance between the hatching lines.

The following soft tissue samples of pigs *in vitro* of different types with high water content (70−80%) were used as biomodels: cardiac muscle (myocardium), liver, skeletal muscle 4−5 mm thick and aorta 3−3.5 mm thick. These biotissues are similar in water content and thermophysical characteristics, but differ significantly in structure and strength characteristics (Table 1). The biotissues were used for 48 h post mortem. Between experiments, all samples were stored in a closed Petri dish at a temperature of 0−4 °C.

In experiments on automated evaporation of biomodel surface areas, a single scan of a rectangular area measuring 8.5 mm × 11.6 mm was performed. The distance between the hatching lines was 150 μm. A lens with a focal length of 50 mm was used. The radiation was focused on the surface of the biomodel. The focal spot size was 180 μm at a level of 86%. In the experiments, the evaporated zone of biotissues was studied depending on the power of laser radiation at a constant scanning speed of 15 mm/s.

After scanning, the samples were frozen in a refrigerator at −15 °C. Then, transverse sections of the scanning area were obtained in these samples. The cut was made with a blade through the center of the evaporated zone perpendicular to the surface of the sample and in a direction perpendicular to the direction of the laser scanning lines. The evaporation depth of the samples was measured using photographs of cross-sections of the evaporation zone. The evaporation depth was determined for 5 samples at fixed values of power, scanning speed and hatching density. Then the obtained values were averaged and the standard deviation was found.

3 Results

Fig. 1 shows cross-sections of the evaporated zone of different types of biological tissues at a radiation power of 6.5 W and a scanning speed of 15 mm/s. It can be seen that the section of the evaporated zone has a sawtooth shape. This is due to the incomplete overlap of individual cuts when scanning the laser beam. Also, additional irregular unevenness of the evaporated zone is caused by the heterogeneity of biotissues and the peculiarities of non-stationary processes of mass removal from the zone of laser radiation exposure [26, 27]. In Fig. 1, it can be seen that for skeletal muscle, the shape of the “teeth” is irregular, some of the “teeth” stick together, and their surface is loose. A similar picture was observed for the heart muscle and liver. For the aorta, the shape of the evaporated zone has clearer outlines, and the “teeth” are more regularly distributed across the evaporated zone. It is obvious that such a qualitative difference in surfaces is caused by the fact that the aorta is a much stronger tissue compared to others. Under the saw-tooth surface of the evaporated tissue zone, a zone with a whitish tint was observed, which is associated with tissue coagulation. This zone was not observed for the aortic tissue, since the original aortic tissue already has a light whitish color.

As in work [19], the result of evaporation of biotissues during laser scanning was characterized by the maximum depth H_{max}. The characterization of the scanning result by maximum depth is caused by the difficulty of determining the average evaporation depth $\langle H \rangle$ from photographs of sections. The H_{max} value was averaged over sections of 5 samples under the same scanning conditions. Fig. 2 shows the measured depths of evaporation of skeletal muscle and aorta depending on the power of laser radiation. As can be seen, these dependencies are linear. A similar pattern was observed for the other biological tissues. Moreover, the maximum evaporation depth was obtained for skeletal muscle, and the minimum evaporation depth was obtained for the aorta. On average, the evaporation depth for skeletal muscle was 42% greater than for aorta. For other tissues, the difference in evaporation depth was smaller.

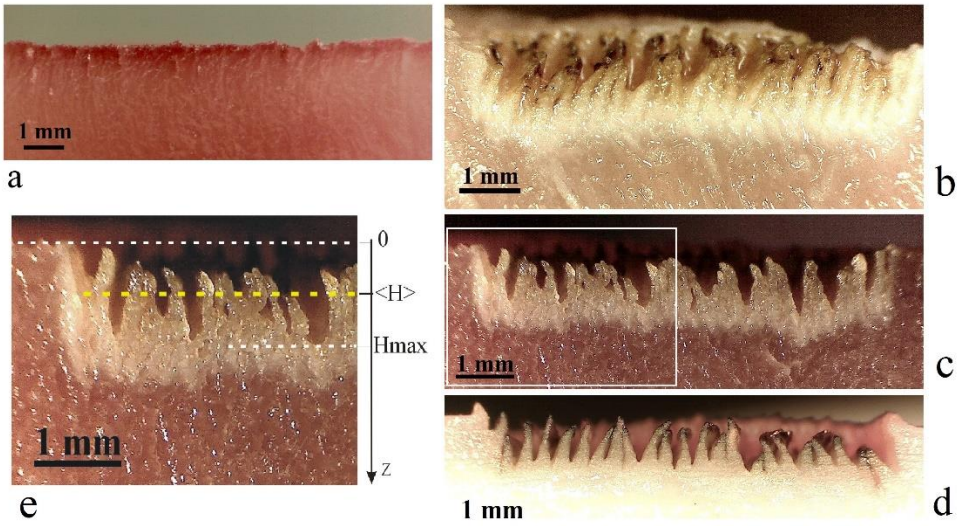

Fig. 1 Photographs of cross-sections of biological tissues before and after laser exposure at a radiation power of 6.5 W and a scanning speed of 15 mm/s. (a) Cross-section of skeletal muscle before laser irradiation; (b−e) cross-sections after laser irradiation; (b) skeletal muscle, muscle fibers were located vertically; (c) skeletal muscle, muscle fibers are directed horizontally along the scanning line of the laser beam; (d) aorta; (e) enlarged scale for the evaporation zone of skeletal muscle, which is indicated by the frame in panel (c). <*H*> − average evaporation depth.

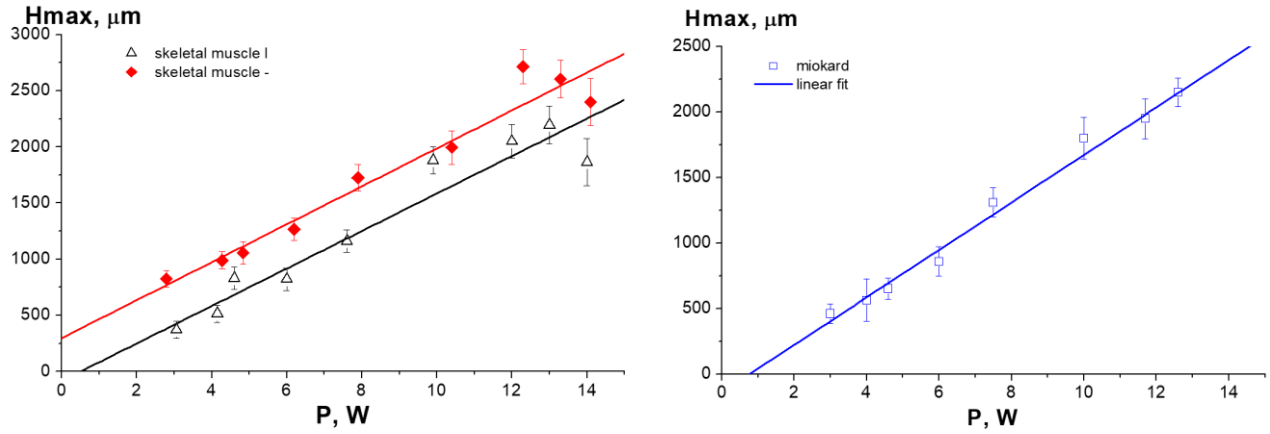

(a) (b)

Fig. 2 Dependence of the maximum depth of evaporation of (a) skeletal muscle and (b) myocardium on the power of laser radiation at a scanning speed of 15 mm/s and a distance between strokes of 150 μm. White triangle marks – fibers along the laser beam (vertically (|)); red rhomb marks – fibers horizontally (-) and along the scanning line of the laser beam.

As follows from Fig. 2(a), there is a noticeable difference in the depth of evaporation of skeletal muscle depending on the location of muscle fibers relative to the scanning trajectory of the laser beam. When the fibers are located along (|) the laser beam, the evaporation depth is less than the depth when the fibers are located horizontally (-) (perpendicular to the laser beam). At low radiation power, H_{max} differs by more than 2 times for different fiber arrangements, whereas at higher power, this difference is 25%. This indicates that not only water evaporation but also tissue matrix rupture, which depends on the arrangement of the fibers, plays a role in tissue mass removal. The lower depth of evaporation with a vertical arrangement of fibers can be explained by the fact that under excess water vapor pressure, muscle fibers do not break, but split. After the radiation exposure stops, the unbroken fibers “stick together”. When the fibers are arranged horizontally, excess pressure causes them to rupture and be carried away from the impact zone along with water vapor. These mechanisms of laser evaporation of anisotropic tissue require more careful consideration using histological methods.

For each studied biotissue, the coefficients of the linear dependence $H_{max} = a + b \cdot P$ were found using the least squares method. The results are presented in Table 2. Almost all linear dependencies have a close coefficient b in the range of 164–181 μm/W. The exception is the aorta, for which b is noticeably smaller.

Table 2 Parameters of soft tissue evaporation by continuous CO_2 laser radiation.

№	Biotissue	*a*, μm	*b*, μm/W	dH_{max}, %	*Pc*, W
1	Myocardium	−129 ± 59	181 ± 6	0.2−19	2.1
2	Liver	109 ± 100	176 ± 13	0.2−32	2.1
3	Skeletal muscle (-)	297 ± 140	169 ± 15	2.7−68	6.5
4	Skeletal muscle (|)	−60 ± 170	164 ± 18	2.3−42	1.4
5	Aorta	83 ± 54	125 ± 6	5−30	1.1

The coefficient *a* differs significantly more for different tissues. In our opinion, this is due to the fact that the coefficient *a* is more closely related to the tissue evaporation threshold. In this paper we do not consider the issue of tissue evaporation threshold. It is obvious that near the threshold the dependence of the evaporation depth on the power will not be linear. In this mode, many processes play a role, such as thermal conductivity, near-surface heat outflow from the surface due to surface evaporation of water, diffusion of intra-tissue water, the occurrence of elastic deformations of the tissue in the laser exposure zone, etc. For this reason, the coefficient *a* varies significantly for different tissues. Far from the evaporation threshold, when intensive evaporation of tissue water occurs, its boiling, accompanied by micro-explosions, the water-steam phase transition plays a major role in the energy balance. This is evident in the fact that the proportionality coefficients b between the evaporation depth and power are quite close for different tissues.

In work [19] we developed a semi-empirical evaporation model for calculating the depth of evaporation of soft tissues when scanning with a continuous CO_2 laser beam. According to this model, when scanning a laser beam with a distance between strokes *d*, an evaporated zone is formed on the surface of the tissue, having a structure with maxima and minima with a period *d*. The shape of such an evaporated zone, assuming a Gaussian shape of a separate cut of tissue, is described by the formula:

$$H(x) = \frac{P}{\sqrt{\pi} V \rho Q r_0} \sum_{k=0}^{N} e^{-\left(\frac{x-kd}{r_0}\right)^2}, \qquad (1)$$

where Q = 2.26·10^6 J/kg – specific heat of water vaporization, ρ – water density, P – laser radiation power, V – scanning speed, x – coordinate along the x-axis, directed perpendicular to the direction of laser lines during scanning

It can be seen that the depth of evaporation is proportional to the power *P*. In this case, the proportionality coefficient is determined by the tissue scanning parameters *V* and *d*. In accordance with Eq. (1), we obtained (using the Mathcad program) that at *P* of 1 *W*, *V* of 15 mm/s and a hatching period *d* of 150 μm, the maximum evaporation depth is 175 μm. Thus, the proportionality coefficient b_0 between the maximum evaporation depth H_{max} and the laser radiation power is equaled to 175 μm/W. This is practically identical to the coefficient *b* obtained experimentally for the liver, myocardium and skeletal muscle (see Table 2). For the aorta, this coefficient is significantly less than the calculated value. This is due to the strength characteristics of this tissue. In this case, a significant portion of the invested energy goes not only to the water-steam phase transition, but also to the rupture of the more durable aortic matrix.

In Fig 3, all measured depth values for all studied biotissues are shown on one graph. This graph also shows the calculated linear dependence $H_{max} = b \cdot P$ is equaled to 175 μm/W · P.

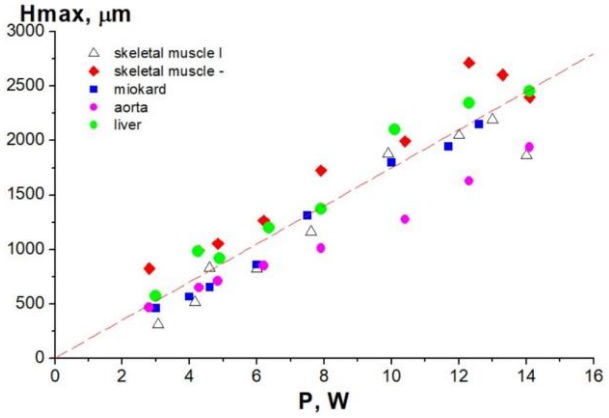

Fig. 3 Maximum depth of evaporation of soft biotissues. The dotted line is the calculated dependence according to the evaporation model of evaporation of soft biotissues as shown in Eq. (1).

Table 2 shows the range of variation in the deviation value dH_{max} of the measured depth H_{max} from the calculated linear dependence $b_0 \cdot P$ for different tissues. The maximum difference between the depth of evaporation of biological tissues and the calculated value is tens of percent. The standard deviation of the measured values of H_{max} for all biological tissues from the calculated linear dependence of H_{max} is 16%. Large deviations (e.g. 68% for skeletal muscle) between calculation and experiment occur in the low power region (up to 3−4 W). This is due to the fact that the calculated dependence does not take into account the evaporation threshold. In the evaporation model presented by us in Ref. [19], it is assumed that laser action occurs far from the evaporation threshold of biological tissue.

Let us estimate how the depth of evaporated biotissue differs from the calculated $H_{max}0 = b_0 \cdot P$ ($b_0 = 175$ μm/W) depending on the laser radiation power. Let for a specific biotissue $H_{max} = a + b \cdot P$. Then the relative deviation of this value from the calculated one will be:

$$\eta \equiv \left|\frac{H_{max}0 - H_{max}}{H_{max}0}\right| = \left|\frac{a}{b_0 * P} + \frac{b - b_0}{b_0}\right|. \quad (2)$$

The magnitude of this deviation is related to two components. The first is due to the fact that the tissue has a non-zero value of the parameter a. This first component decreases with increasing P, i.e. with distance from the threshold of the onset of evaporation. The second component of the deviation η is caused by the difference between the proportionality coefficient b and the calculated value b_0. As already noted, this coefficient for soft tissues is quite close and the value of $(b-b_0)/b_0$ is up to 12% (for skeletal muscle when the fibers are located along the laser beam) and 29% for the aorta.

From Eq. (2) we estimate the boundary power Pc, at which the deviation of the calculated dependence from the measured one will be 30%. Table 3 shows the Pc values for different tissues. For all tissues, the deviation of the evaporation depth dH_{max} from the calculated value is less than 30% when the radiation power Pc is more than 1−2 W. The exception is skeletal muscle, where the muscle fibers are directed perpendicular to the laser beam. In this case, the difference in depth from the calculated value of less than 30% is obtained at radiation powers greater than 6.5 W.

Thus, despite the fact that soft tissues can differ significantly in their strength characteristics (more than 2 orders of magnitude as in the case of the liver and aorta), the depth of evaporation by continuous CO_2 laser radiation far from the evaporation threshold is in good agreement with the evaporation model for soft tissues. The approach developed in Ref. [19] for calculating the depth of soft tissue evaporation during 2D scanning of a laser beam can serve as a good predictive model for preoperative planning using continuous CO_2 laser radiation.

4 Conclusion

The evaporation of soft water-containing biotissues with very different structure and strength characteristics under two-coordinate laser scanning of continuous CO_2 laser radiation has been studied. It is shown that the depth of evaporation of biological tissues is well described by a linear dependence on the laser radiation power. The proportionality coefficients between the maximum evaporation depth and the laser radiation power for all tissues, with the exception of the aorta, practically coincide with the calculated coefficient of 175 μm/W (for a scanning speed v of 15 mm/s and a laser beam diameter of 180 μm), obtained on the basis of the evaporation model of soft tissue evaporation. For the aorta, this coefficient is lower and is (125 ± 6) μm/W. This difference is due to the significantly higher tensile strength of the aorta compared to other soft tissues.

The data analysis showed that despite the significant differences in the structure and strength characteristics of soft tissues, the average deviation of the calculated evaporation depth from the measured value across all tissues is 16%. At the same time, at low laser radiation powers, the deviation of the evaporation depth from the calculated value for a specific tissue can be tens of percent. This is due to the fact that near the evaporation threshold, the dependence of depth on power is nonlinear, which is not taken into account in the evaporation model. It was shown that for all soft tissues studied, with the laser exposure parameters used in the experiment, the deviation of the evaporation depth from the calculated value is less than 30% for a radiation power of more than 1−2 W. The exception is skeletal muscle, where the muscle fibers are directed perpendicular to the laser beam. In this case, the difference in depth from the calculated value of less than 30% is obtained at radiation powers greater than 6.5 W.

Based on the conducted studies, it can be stated that significant differences (by an order of magnitude or more) in the strength characteristics of soft tissues do not lead to an equally strong difference in the depth of evaporation by continuous CO_2 laser radiation. The approach we present can be used to implement predictive modeling in preoperative planning using scanning systems based on continuous CO_2 lasers.

The work was carried out within the state assignment of the NRC "Kurchatov Institute".

Disclosures

All authors declare that there is no conflict of interest in this paper.

References

1. G. Maza, A. Sharma, "Past, Present, and Future of Robotic Surgery," Otolaryngologic Clinics of North America 53(6), 935−941 (2020).
2. J. Han, J. Davids, H. Ashrafian, A. Darzi, D.S. Elson, and M. Sodergren, "A systematic review of robotic surgery: From supervised paradigms to fully autonomous robotic approaches," The International Journal of Medical Robotics and Computer Assisted Surgery 18(2), e2358 (2022).
3. I. O. Gritskov, A. A. Vitoslavskii, K. A. Kryazheva, A. O. Vasilev, K. V. Kolontarev, and D. Yu. Pushkar, "Robotic Systems in Surgery," Biomedical Engineering 55(5), 365−369 (2022).
4. Y. Y. Juo, A. Abiri, J. Pensa, S. Sun, A. Tao, J. Bisley, W. Grundfest, and E. Dutson, "Center for Advanced Surgical and Interventional Technology Multimodal Haptic Feedback for Robotic Surgery," Chapter 17 in Handbook of Robotic and Image-Guided Surgery, M. H. Abedin-Nasab (Ed.), Elsevier, 285−301 (2020).

5. U. Paasch, M. Haedersdal, "Laser systems for ablative fractional resurfacing," Expert Review of Medical Devices 8(1), 67−83 (2011).
6. A. Aslam, T. S. Tina, "Evolution of Laser Skin Resurfacing: From Scanning to Fractional Technology," Dermatologic Surgery 40(11), 1163–1172 (2014).
7. R. Colasanti, L. Giannoni, S. Dallar, V. Liverotti, D. Aiudi, A. Di Rienzo, F. Rossi, and M. Iacoangeli, "Application of a Scanner-Assisted Carbon Dioxide Laser System for Neurosurgery," World Neurosurgery 153, e250−e258 (2021).
8. A. R. Padalhin, "Lasers and Robots: Recent Developments in Transoral Laser and Transoral Robotic Surgery," Medical Lasers 9(2), 103–109 (2020).
9. H. C. Lee, N. Pacheco, L. Fichera, and S. Russo, "When the End Effector Is a Laser: A Review of Robotics in Laser Surgery," Advanced Intelligent Systems 4(10), 2200130 (2022).
10. A. Acemoglu, L. Fichera, I. E. Kepiro, D. G. Caldwell, and L. S. Mattos, "Laser Incision Depth Control in Robot-Assisted Soft Tissue Microsurgery," Journal of Medical Robotics Research 2(3), 1740006 (2017).
11. S. Stopp, D. Svejdar, E. von Kienlin, H. Deppe, and T. C. Lueth, "A new approach for creating defined geometries by navigated laser ablation based on volumetric 3-D data," IEEE Transactions on Biomedical Engineering 55(7), 1872−1880 (2008).
12. L. Fichera, D. Pardo, P. Illiano, J. Ortiz, D. G. Caldwell, and L. S. Mattos, "Online estimation of laser incision depth for transoral microsurgery: approach and preliminary evaluation," The International Journal of Medical Robotics and Computer Assisted Surgery 12(1), 53−61 (2016).
13. G. Ma, R. Prakash, B. Mann, W. Ross, and P. Codd, "3D Laser-and-tissue Agnostic Data-driven Method for Robotic Laser Surgical Planning," in 2023 IEEE/RSJ International Conference on Intelligent Robots and Systems (IROS), IEEE, 8446–8453 (2023).
14. N. Furzikov, "Different lasers for angioplasty: Thermooptical comparison," IEEE Journal of Quantum Electronics 23(10), 1751−1755 (1987).
15. N. P. Furzikov, "Analytical approximation of soft tissue laser ablation," SPIE Proceedings 1353, V. I. Konov, G. J. Mueller, and A. M. Prokhorov (Eds.), 18–26 (1990).
16. J. T. Walsh, T. F. Deutsch, "Pulsed CO2 laser ablation of tissue: effect of mechanical properties," IEEE Transactions on Biomedical Engineering 36(12), 1195−1201 (1989).
17. B. Majaron, P. Plestenjak, and M. Lukač, "Thermo-mechanical laser ablation of soft biological tissue: modeling the micro-explosions," Applied Physics B: Lasers and Optics 69(1), 71–80 (1999).
18. F. Partovi, J. A. Izatt, R. M. Cothren, C. Kittrell, J. E. Thomas, S. Strikwerda, J. R. Kramer, and M. S. Feld, "A model for thermal ablation of biological tissue using laser radiation," Lasers in Surgery and Medicine 7(2), 141–154 (1987).
19. A. K. Dmitriev, A. N. Konovalov, V. N. Kortunov, and V. A. Ulyanov, "Evaporation peculiarities of soft biological tissues in the process of automated 2D-scanning of CO2 laser radiation," Journal of Biomedical Photonics & Engineering, 10(4), 040307 (2024).
20. E. Vlaisavljevich, Y. Kim, G. Owens, W. Roberts, C. Cain, and Z. Xu, "Effects of tissue mechanical properties on susceptibility to histotripsy-induced tissue damage," Physics in Medicine & Biology 59(2), 253–270 (2014).
21. G. A. Holzapfel, G. Sommer, C. T. Gasser, and P. Regitnig, "Determination of layer-specific mechanical properties of human coronary arteries with nonatherosclerotic intimal thickening and related constitutive modeling," American Journal of Physiology-Heart and Circulatory Physiology 289(5), H2048–H2058 (2005).
22. A. K. Dmitriev, A. N. Konovalov, V. N. Kortunov, and V. A. Ulyanov, "Diagnostics of Layer-by-Layer Biotissue Evaporation in the Process of Two-Coordinate Scanning by a Laser Beam for Precision Surgery," Journal of Biomedical Photonics & Engineering 9(2), 020302 (2023).
23. D. J. Taylor, N. P. O. Green, and G. W. Stout, Biological Science, vol. 1, 2nd ed., R. Soper (Ed.), Cambridge University Press, Cambridge (1990).
24. L. Bianchi, F. Cavarzan, L. Ciampitti, M. Cremonesi, F. Grilli, and P. Saccomandi, "Thermophysical and mechanical properties of biological tissues as a function of temperature: a systematic literature review," International Journal of Hyperthermia 39(1), 297–340 (2022).
25. V. Tuchin (Ed.), "Tissue Optics. Light Scattering Methods and Instruments for Medical Diagnosis," 2nd Ed., SPIE Press, Bellingham, WA (2007). PDF ISBN: 9780819481061.
26. V. M. Gordienko, A. N. Konovalov, Yu. Ya. Putivskii, N. N. Kurochkin, and V. I. Savin, "Investigation of the dynamics of laser-induced explosive boiling of water using the autoheterodyning scheme," High Temperature 36(5), 789−795 (1998).
27. A. K. Dmitriev, A. N. Konovalov, V. N. Kortunov, and V. A. Ulyanov, "Doppler diagnostics of laser evaporation of biological tissues," Journal of Laser Applications 34(4), 041201 (2022).

Raman *in Vivo* Analysis of Melanoma Invasion Level

Lyudmila A. Bratchenko[1*], Yulia A. Khristoforova[1], Yulia G. Loginova[2], Alexander A. Moryatov[2], Valery P. Zakharov[1], Oleg I. Kaganov[2], and Ivan A. Bratchenko[1]

[1] Department of Laser and Biotechnical Systems, Samara National Research University, 34 Moskovskoe Shosse, Samara 443086, Russian Federation

[2] Department of Oncology, Samara State Medical University, 89 Chapaevskaya str., Samara 443099, Russian Federation

*e-mail: shamina94@inbox.ru

Abstract. The number of diagnosed melanoma cases is increasing every year, and there is an urgent need for novel screening approaches that may help in the diagnosis and prognosis of melanoma. In this study we propose to utilize conventional Raman spectroscopy for the determination of Clark level of invasion. We collected spectral data from 59 melanoma samples and achieved accuracy of 75% for discrimination of I–II vs. III–V levels of invasion. This study is the first to explore the potential of spectral analysis, utilizing Raman scattering and autofluorescence techniques, for distinguishing melanoma tissues according to their invasion level. Analysis of spectral data was performed with the application of projection on latent structures and discriminant analysis. The most significant for the model is the spectrum bands, associated with autofluorescence. The most informative bands of the Raman component for the constructed discrimination of melanoma tissues by the degree of invasion are the bands of 1385 cm^{-1}, 1445 cm^{-1}, 1487 cm^{-1}, 1565 cm^{-1}, and 1695 cm^{-1}, associated with the presence of pigments (melanin), protein components (e.g., amide bonds, collagen), and lipid structures. The proposed approach may be useful in fast screening analysis for the determination of the best treatment plan for the patient based solely on the analysis of Raman spectra.

Keywords: Clark level; melanoma; Raman spectroscopy; autofluorescence; optical biopsy; invasion, PLS.

Paper #9324 received 18 Aug 2025; revised manuscript received 27 Aug 2025; accepted for publication 27 Aug 2025; published online 30 Sep 2025. doi: 10.18287/JBPE25.11.030303.

1 Introduction

The number of diagnosed melanoma cases is increasing every year, and there is an urgent need for novel screening approaches that may help in the diagnosis and prognosis of melanoma [1]. One of the most common approaches to evaluate the stage of melanoma growth and further evaluate a patient's prognosis is a Clark level. The Clark level of invasion is determined by examining the depth of melanoma's penetration into the skin's layers during a microscopic study. It categorizes the melanoma's spread into five levels (I–V), ranging from the epidermis to the subcutaneous tissue. A pathologist, examining the tissue, uses this information to assess the melanoma's stage and prognosis [2].

Since 1969 Clark and his collaborators had found a link between the level of tumor invasion and the prognosis of patients with cutaneous melanoma. They showed a median survival time of 6.83 years for the patients with level II of invasion and 3.5 years for level V [3, 4]. Thus, the information about Clark level of invasion provides an opportunity to predict an outcome for the patient. In this regard, it would be very helpful in medical practice to determine Clark level of invasion fully in noninvasive manner (in contrast to the pathologist examination).

Today there are numerous methods that may be used for skin tissue analysis: ultrasound imaging [5], magnetic resonance imaging [6], optical coherence tomography [7], optoacoustic imaging [8], scanning electron microscopy [9], fluorescence lifetime imaging [10], and many others. Despite the capabilities of the mentioned approaches, there are several limiting factors that prevent the inclusion of such technologies in medical practice. Such limitations include the high price of equipment

(magnetic resonance imaging, fluorescence lifetime imaging, optoacoustic imaging), very limited depth of analysis (optical coherence tomography), low resolution (ultrasound imaging), etc. [11]. The described methods utilize information about tumor invasion; however, there is an opportunity to measure the chemical composition of the tumor and predict the invasion level based on this information.

One possible way to create a simple and reliable method of tissue noninvasive component analysis is the application of Raman spectroscopy (RS) [12]. RS may provide fast and reliable data about skin tissue composition [13] and offers an opportunity to create handheld portable devices [14]. Application of RS (and its modifications) was mainly demonstrated for the precise diagnosis of skin tumors (both *ex vivo* and *in vivo* [15]); however, application of RS in the determination of the Clark level of invasion was never investigated.

In this study we investigate a possibility to determine Clark level of invasion based solely on the analysis of Raman spectra from the analyzed melanoma tissues. We aimed at differentiation of Clark level I and II melanomas from Clark level III, IV and V. We analyzed *in vivo* melanomas with a portable Raman device and utilized well-known machine learning techniques for the classification of melanoma level of invasion and utilized validation techniques to guarantee the robustness of the proposed approach.

2 Materials and Methods

2.1 Melanoma Tissue Samples and Experiment Preparation

In the current study, *in vivo* analysis of melanoma tissues was performed at the Samara Regional Clinical Oncology Dispensary. Patients were selected using stratified random sampling. The study included 59 people. All subjects were Caucasian with skin phototypes I and II. The Clark invasion level was established based on the histological examination results. The characteristics of the study sample are presented in Table 1. Standardized *in vivo* registration of spectral characteristics of melanoma tissue was performed for each patient. Informed consent was obtained from the patients; all participants were over 18 years of age. The *in vivo* study protocols were approved by Samara State Medical University (Samara Region, Samara, Russia, protocol No 132, 29 May 2013, and clinical studies fall within the Code of Ethics of a Doctor of Russia, approved at the 4th conference of the Russian Medical Association, and within the World Medical Association Declaration of Helsinki).

Table 1 Brief description of the sample.

Group	Clark level	Number of patients	Number of spectra
1	1, 2	26	26
2	3, 4, 5	33	33

2.2 Experimental Portable Raman System

Excitation of Raman scattering spectra of melanoma tissues was performed using a laser module (LuxxMaster LML-785.0RB-04, PD-LD, New Jersey, USA) with a central wavelength of 785 nm. The Raman probe (RPB785, InPhotonics, Massachusetts, USA) focuses the excitation radiation and collects and filters the scattered radiation. The focal length of the Raman probe used was 7.5 mm. A tip with a silicone attachment was used to fix the distance of 7 mm between the probe and the melanoma tissue surface, which made it possible to collect scattered light from the upper layers of the skin (up to 1–2 mm deep). The laser power density on the melanoma tissue surface was about 0.3 W/cm^2 and did not cause damage or discomfort to patients. The collected signal was decomposed into a spectrum using a portable spectrometer (QE65Pro, Ocean Optics, Florida, USA). Spectra were recorded in the range of 800–914 nm with a spectral resolution of 0.2 nm and an exposure time of 20 s with 3 accumulations.

2.3 Processing and Analysis of Experimental Data

The spectra were recorded using the SpectraSuite program (Ocean Optics, Florida, USA). Immediately before recording the spectral characteristics of the studied samples, a preliminary registration of the background signal of the system without a melanoma tissue sample was performed. After that, the background component was automatically subtracted from the subsequent recorded skin spectra using the built-in SpectraSuite algorithm. Each of the obtained spectra is a discrete set of 455 parameters (predictors).

The experimental data are characterized by multicollinearity, high fluorescent background, and multiple overlaps of the spectral contribution of various components of melanoma tissue. Bilinear and nonlinear methods of analysis have proven themselves well for solving the task of discrimination of such spectral data of multicomponent biological samples [16−18]. It should be noted that the analyzed sample has a limited volume of patients with a large number of parameters for each patient. Therefore, the use of nonlinear machine learning methods is complicated by the risk of overfitting the model and is undesirable for the current sample. In the current work, projection bilinear methods are advisable to use to achieve a statistically reliable result. Therefore, the experimental data were subjected to discriminant analysis with projection onto latent structures (PLS-DA). PLS-DA models were constructed using the MDAtools package available within the R studio software [19]. Thus, the work solves the task of supervised classification, where each patient in the sample is characterized by spectral data (parameter matrix) and a priori information about belonging to a group depending on the degree of melanoma invasion (target data vector). In conditions of a limited sample size and a large number of parameters for each patient, it is necessary to strictly control the overfitting of the model to avoid

overestimated discrimination characteristics. Previously, our research group used a combination of the following to achieve a statistically reliable assessment of the feasibility of the analysis method on a limited sample: 1) control of the standard error of the model during cross-validation; 2) several iterations of building and testing the model, followed by averaging of the characteristics; 3) analysis of important variables for the model [20]. Similarly, in the current work, the spectral dataset was divided randomly: 80% of the samples from each group were used to train the model (training set), and 20% of the samples from each group were used to test the model (test set). Then, the training and test sets were preprocessed. Separate preprocessing eliminates the "leakage" of information about the test set into the model. The spectral data were smoothed using the Savitzky-Golay filter (15 filter window width, 1 order of polynomial used for smoothing, and 0 order of derivative to take) and normalized by the Standard Normal Variate (SNV) algorithm. Smoothing using the Savitzky-Golay filter reduces noise and random fluctuations in the spectral data while preserving important spectral features (peaks and their shapes). Normalization using the SNV method eliminates variations in the spectral intensity caused by external factors not related to the chemical composition. Together, these preprocessing methods provide a more accurate and reliable extraction of informative features of the spectra for subsequent statistical analysis and classification. The PLS-DA model was trained on the training set and then used to classify the test set. In total, random partitioning into training and test sets was repeated 10 times. The number of loading vectors in the model construction was selected in accordance with the first local minimum on the model mean square error graph calculated for a different number of components and k-fold cross-validation predictions (k = 6). The analysis of the most significant spectral bands for the constructed models was implemented based on the variable importance distribution in the constructed projection (VIP distribution) [21]. The VIP distribution allows for determination which spectral ranges have the most significant effect on the prediction of the target variable. The allocated spectral ranges demonstrate those areas of the spectrum that are most responsible for variations in the target variable, which helps to understand the chemical or physical properties of the samples.

3 Results and Discussion

Figure 1 demonstrates the mean pre-processed spectra of melanoma tissues characterized by invasion to the papillary dermis (group 1) and melanoma tissues with invasion to the subcutaneous fat (group 2).

Figure 1 shows that the spectral region of 450–1800 cm^{-1} is characterized by two key components: a broadband autofluorescence signal and weak Raman scattering peaks. To date, a number of scientific groups have demonstrated that the combination of Raman scattering and autofluorescence allows for obtaining comprehensive information on the molecular and metabolic state of skin tissues and skin neoplasms [15, 22, 23]. In the recorded spectra in the range of 450–1200 cm^{-1}, autofluorescence dominates and overlaps the weak Raman signal, which limits the analysis of this range to only the fluorescence characteristics of melanoma. Autofluorescence of human skin in the near-IR range is caused by the presence of various fluorophores, such as collagen, elastin, and melanin. Melanoma demonstrates unique fluorescent properties associated with an increased melanin content and oxidative stress [24–27]. At the same time, in the spectral range of 1200–1800 cm^{-1}, the contribution of autofluorescence decreases, which allows for a clearer resolution of Raman peaks. The recorded spectra of melanoma tissues are characterized by the presence of Raman peaks at 1285 cm^{-1}, 1445 cm^{-1}, and 1665 cm^{-1}. It should be noted that the assignment of spectral bands in the spectrum of melanoma tissue to specific substances is quite complex due to the possible spectral contribution of several substances to one specific band. In an earlier work of our research group, a statistically significant relationship was found between the Raman intensity of the spectral regions 1270–1340, 1440–1460, 1540–1560, and 1640–1670 cm^{-1} and the tumor type [14]. In addition, according to the results of the histological examination, the analyzed melanoma tissue samples are characterized by the presence of lymphoid infiltration of varying severity, which can also make a spectral contribution to the recorded melanoma tissue spectra in the bands 1242–1252, 1450, and 1580–1660 cm^{-1} [28, 29]. Thus, the spectral range of 400–1800 cm^{-1} reflects the combination of autofluorescence and Raman spectral features, which provides a comprehensive approach to the study of melanoma tissue. A strong overlap of the spectra of the analyzed groups should be noted. Weak intergroup dispersion makes it difficult to detect spectral differences between melanoma tissues of different invasions "by eye" and confirms the need to use a multivariate analysis method.

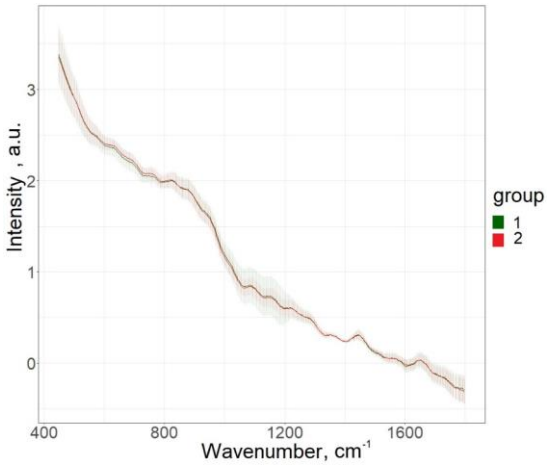

Fig. 1 Mean preprocessed spectra with standard deviation for the group with melanoma invasion from the epidermal layer to the papillary dermis (group 1) and for the group with melanoma invasion to the subcutaneous fat (group 2).

Detection of statistically significant spectral differences in melanoma tissues of different invasions was implemented based on 10 iterations of dividing the spectral base into training and test subsamples with subsequent construction of a PLS-DA model. Figure 2 demonstrates the choice of model parameters using one of the 10 iterations as an example. The distribution of the eigenvalues of the loading vectors demonstrates that the first two loading vectors cover a large share of the explained data variation. At the same time, the model at the iteration under consideration is characterized by a decrease in the mean square error of the model during cross-validation and the absence of a local minimum up to the third loading vector. Thus, for the iteration under consideration of model construction, the 3rd loading vector is optimal, covering the main share of the variation in the original data and not leading to overfitting.

As a result of 10 iterations of model construction, the average characteristics of melanoma tissue discrimination by the degree of invasion for the training data set were: specificity at the level of 0.69, sensitivity 0.67, accuracy 0.68. The average characteristics of the constructed models for the test data were specificity 0.71, sensitivity 0.80, and accuracy 0.75. It should be noted that the models are stable and have good generalization ability, which follows from better indicators of the models for the test sets than for the training ones. The average distribution of the importance of the spectrum variables for 10 iterations of constructing a model of melanoma tissue discrimination by the degree of invasion is shown in Fig. 3.

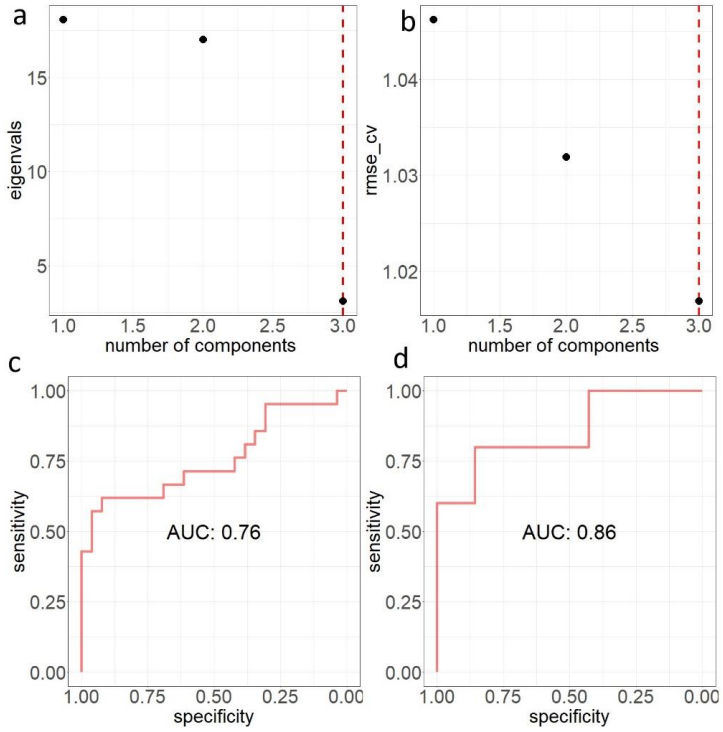

Fig. 2 Characteristics of the discrimination model for melanoma tissues of different invasions for one iteration of dividing the base into training and test sets. (a) Eigenvalues of loading vectors; (b) dependence of the mean square error of the model during cross-validation on the number of loading vectors; (c) characteristics of the constructed discrimination for the training sample; (d) characteristics of discrimination for the test sample.

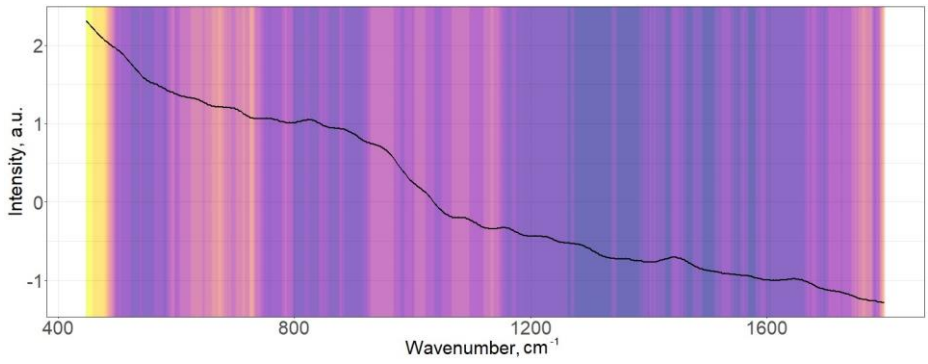

Fig. 3 VIP-distribution of spectrum variables in constructing discrimination of melanoma tissues by the degree of invasion (average result for 10 iterations of model construction).

As follows from Fig. 3, the most significant for the model is the spectrum intensity in the ranges of 450–500 cm^{-1}, 700–770 cm^{-1}, and 1070–1190 cm^{-1}. The greatest spectral contribution to the selected areas is made by the autofluorescent component. The main tissue fluorophores, such as elastin, collagen and NADH, are characterized by fluorescence when excited in the UV or short-wave visible range, whereas the main endogenous fluorophore of melanoma tissue, excited in the near-IR range, is melanin [24, 25]. Moreover, near-IR radiation penetrates tissue well, which allows obtaining information about the deep layers of the skin and pathologically associated changes in them. Therefore, a significant contribution of the autofluorescent component to the model may be due to an increase in the volume fraction of melanocytes with an increase in the stage of invasion and, as a consequence, an increase in the autofluorescent contribution associated with melanin [30]. The most informative areas of the Raman component for the constructed discrimination of melanoma tissues by the degree of invasion are the bands of 1385 cm^{-1}, 1445 cm^{-1}, 1487 cm^{-1}, 1565 cm^{-1}, and 1695 cm^{-1}. In general, peaks in these ranges indicate the presence of pigments (melanin), protein components (e.g., amide bonds, collagen), and lipid structures. Their combination and intensity may indicate characteristic features of melanoma tissue, such as high pigmentation concentration, altered protein structure, and increased metabolic activity. The 1385 cm^{-1} band may be associated with the spectral contribution of amines, nitrogen-containing groups, and amino acids, as well as melanin [31]. The 1445 cm^{-1} band is characteristic of $\delta(CH_2)$ and $\delta(CH_3)$ deformation vibrations in proteins and lipids, as well as amino acids and pigments [32]. This peak is often associated with protein and lipid components of tissues. The Raman band at 1487 cm^{-1} may be associated with pigments such as melanin, as well as carbon-carbon bonds in aromatic systems (e.g., amino acid residues or pigments) [33]. The peak in the 1487 cm^{-1} region may be associated with vibrations of amino acids such as tryptophan or tyrosine, which are important for the synthesis of melanin. This may indicate the activity of metabolic processes associated with pigment formation. The spectral contribution to the 1565 cm^{-1} band is characteristic of pigments, in particular melanin, as well as C=N bonds, which are present in some proteins and pigments [31]. The 1695 cm^{-1} band is associated with amide groups (amide I), characteristic of proteins, in particular with the C=O bond in the alpha-helical structure of the protein; it may also indicate the presence of collagen or other structural proteins [33]. The information content of the highlighted Raman bands for the constructed discrimination is lower relative to the information content of the autofluorescence component. However, taken together, both the autofluorescence component and the Raman component of the spectrum provide the construction of a stable model of discrimination of melanoma tissues by the degree of invasion. To date, the main method of analyzing melanoma invasion is histological analysis [34]. The degree of melanoma invasion Clark level in combination with other criteria, such as Breslow thickness, determined by an experienced pathologist based on histology, is an important prognostic factor for survival and the dynamics of the course of melanoma [35, 36]. The simplicity and availability of classical histological assessment, good clinical confirmation, and the possibility of standardized assessment ensure the widespread use of histology for determining the Clark level. At the same time, the methods of invasion analysis according to Clark, based on histological assessment, require high qualification of a specialist and are associated with possible subjectivity in determining the boundaries of invasion. Modern technologies and additional methods help to increase the accuracy and objectivity of histological assessment of melanoma invasion, which is important for determining the prognosis and choosing treatment tactics for melanoma. For example, the scientific group of M. Prodan et al. [37] and the team of authors Y. Li et al. [38] studied the prognostic significance of gene expression and markers in the analysis of invasiveness and progression of melanoma. Gene and biomarker expression is a powerful tool for assessing the invasiveness and progression of melanoma, allowing to predict tumor aggressiveness, the risk of metastasis, the effectiveness of therapy, and the likelihood of relapse.

It should be noted that melanoma progression is also associated with changes in the arrangement of collagen fibers in the skin. In the work [39], Sean J. Kirkpatrick et al. used the optical elastography method to study the mechanical properties of tissues that correlate with varying degrees of dermal damage by the neoplasm. Thus, the use of various methods for the analysis of melanoma invasion allows not only for more accurate assessment of the stage and risk of metastasis but also helps to better understand the pathological features of melanoma associated with its invasion, which contributes to the development of new therapeutic strategies. Spectral methods can be used for rapid noninvasive analysis of molecular and chemical changes in melanoma tissues of varying invasion, which is inaccessible with traditional histology.

The current study describes for the first time the investigation of the capabilities of spectral analysis based on Raman scattering and autofluorescence analysis for discrimination of melanoma tissues by the degree of invasion. The obtained results demonstrated the prospects for using spectral analysis for noninvasive determination of the degree of melanoma invasion and detection of pathologically associated changes in the component composition of melanoma tissues depending on the degree of invasion. At the next stage of the research, it is planned to increase the sample size of patients in order to build a stable regression between the spectral characteristics of melanoma tissue and the corresponding Clark level.

4 Conclusion

The presented results demonstrate that conventional Raman spectroscopy may be utilized for the in vivo evaluation of Clark level of invasion. The achieved accuracy of 75% for discrimination of I–II vs. III–V levels of invasion allows us to hope for the subsequent successful development of the approach with the subsequent possibility of more accurate determination of the invasion level. In this study we analyzed a limited dataset of Raman spectra from melanomas of different invasion levels, and in future studies the number of analyzed melanoma samples as well as the number of analyzed Raman spectra should be significantly increased (according to clinical procedures limitations, we were able to register only one Raman spectrum per analyzed melanoma sample). The proposed approach may be useful in the evaluation of a patient's prognosis. Moreover, as the registration and analysis of Raman spectra takes a couple of minutes, the evaluation of the patient's prognosis may be performed right on the first screening along with the determination of the neoplasm type based solely on the analysis of Raman spectra. Such an approach will save the time of the analysis and ultimately help the doctor to find the best treatment plan for the patient.

Disclosures

All authors declare that there is no conflict of interests in this paper.

Acknowledgments

This study is supported by R & D "Development of a hardware and software complex for non-invasive diagnostics of neoplasms using YERG-2023-0001 spectroscopy" within the framework of the State Order.

References

1. "Cancer Facts & Figures 2025," American Cancer Society, Atlanta (accessed 4 August 2025). [https://www.cancer.org/content/dam/cancer-org/research/cancer-facts-and-statistics/annual-cancer-facts-and-figures/2025/2025-cancer-facts-and-figures-acs.pdf].
2. D. Barh, A. Carpi, M. Verma, and M. Gunduz (Eds.), Cancer Biomarkers: Minimal and Noninvasive Early Diagnosis and Prognosis, CRC Press, Boca Raton (2017). eBook ISBN: 9780429169304.
3. M. Antohe, A. Coman, G. Turcu, R. I. Nedelcu, A. Brinzea, M. Balaban, A. Moroianu, L. Manea, I. Hulea, E. Balasescu, S. A. Zurac, M. Cioplea, C. Popp, L. Nichita, and D. A. Ion, "The prognostic significance of the clinical and histological parameters in primary cutaneous melanoma patients," Medicine and Pharmacy Reports 95(3), 229–235 (2022).
4. W. H. Clark, L. From, E. A. Bernardino, and M. C. Mihm, "The histogenesis and biologic behavior of primary human malignant melanomas of the skin," Cancer Research 29(3), 705–727 (1969).
5. K. Stawarz, A. Galazka, M. Misiak-Galazka, M. Durzynska, A. Gorzelnik, K. Bienkowska-Pluta, J. Korzon, F. Kissin, and J. Zwolinski, "Advances in skin ultrasonography for malignant and benign tumors of the head and neck: current insights and future directions," Journal of Clinical Medicine 14(7), 2298 (2025).
6. M. Kawaguchi, H. Kato, Y. Noda, K. Kobayashi, T. Miyazaki, F. Hyodo, and M. Matsuo, "Imaging findings of malignant skin tumors: radiological–pathological correlation," Insights Imaging 13(1), 52 (2022).
7. C. Burnette, T. E. Sivesind, and R. Dellavalle, "From the cochrane library: optical coherence tomography for diagnosing skin cancer in adults," Journal of Medical Internet Research Dermatology 6, e41355 (2023).
8. M. Zafar, A. P. Siegel, K. Avanaki, and R. Manwar, "Skin imaging using optical coherence tomography and photoacoustic imaging: a mini-review," Optics 5(2), 248–266 (2024).
9. F. S. L. Quintana, H. L. D. Almeida Jr., C. P. Ruas, and V. M. Jorge, "Scanning electron microscopy of dermatofibroma," Anais Brasileiros de Dermatologia Journal 94(3), 358–360 (2019).
10. Y. Ouyang, Y. Liu, Z. M. Wang, Z. Liu, and M. Wu, "FLIM as a promising tool for cancer diagnosis and treatment monitoring," Nano-Micro Letters 13(1), 133 (2021).
11. L. Rey-Barroso, S. Peña-Gutiérrez, C. Yáñez, F. J. Burgos-Fernández, M. Vilaseca, and S. Royo, "Optical technologies for the improvement of skin cancer diagnosis: A review," Sensors 21(1), 252 (2021).
12. D. Lunter, V. Klang, D. Kocsis, Z. Varga-Medveczky, S. Berkó, and F. Erdő, "Novel aspects of Raman spectroscopy in skin research," Experimental Dermatology 31(9), 1311–1329 (2022).
13. L. Franzen, M. Windbergs, "Applications of Raman spectroscopy in skin research − From skin physiology and diagnosis up to risk assessment and dermal drug delivery," Advanced Drug Delivery Reviews 89, 91–104 (2015).
14. I. A. Bratchenko, L. A. Bratchenko, A. A. Moryatov, Y. A. Khristoforova, D. N. Artemyev, O. O. Myakinin, A. E. Orlov, S. V. Kozlov, and V. P. Zakharov, "In vivo diagnosis of skin cancer with a portable Raman spectroscopic device," Experimental Dermatology 30(5), 652–663 (2021).
15. C. Delrue, R. Speeckaert, M. Oyaert, S. De Bruyne, and M. M. Speeckaert, "From vibrations to visions: raman spectroscopy's impact on skin cancer diagnostics," Journal of Clinical Medicine 12(23), 7428 (2023).
16. V. Mieites, M. G. Fernández-Manteca, I. Santiuste Torcida, F. Madrazo Toca, M. J. Marín Vidalled, and O. M. Conde, "Assessment of blood serum stability with Raman spectroscopy and explanatory AI," Spectrochimica Acta Part A: Molecular and Biomolecular Spectroscopy 340, 126297 (2025).

17. W. Liu, Z. Sun, J. Chen, and C. Jing, "Raman spectroscopy in colorectal cancer diagnostics: comparison of PCA-LDA and PLS-DA models," Journal of Spectroscopy 2016, 1–6 (2016).
18. J. Zhao, H. Lui, S. Kalia, T. K. Lee, and H. Zeng, "Improving skin cancer detection by Raman spectroscopy using convolutional neural networks and data augmentation," Frontiers in Oncology 14, 1320220 (2024).
19. S. Kucheryavskiy, "mdatools – R package for chemometrics," Chemometrics and Intelligent Laboratory Systems 198, 103937 (2020).
20. L. A. Bratchenko, Y. A. Khristoforova, I. A. Pimenova, E. N. Tupikova, M. A. Skuratova, G. A. Dvoynikov-Sechnoy, S. Wang, P. A. Lebedev, and I. A. Bratchenko, "SERS-based technique for accessible and rapid diagnosis of multiple myeloma in blood serum analysis," Light: Advanced Manufacturing 6(2), 284–294 (2025).
21. L. A. Bratchenko and I. A. Bratchenko, "Avoiding overestimation and the "black box" problem in biofluids multivariate analysis by raman spectroscopy: interpretation and transparency with the SP-LIME algorithm," Journal of Raman Spectroscopy 56(4), 353–364 (2025).
22. D. Wu, A. Fedorov Kukk, R. Panzer, S. Emmert, and B. Roth, "In vivo Raman spectroscopic and fluorescence study of suspected melanocytic lesions and surrounding healthy skin," Journal of Biophotonics 17(8), e202400050 (2024).
23. L. A. Bratchenko, Y. A. Khristoforova, A. A. Moryatov, and I. A. Bratchenko, "Raman spectroscopy based diagnosis of dermatofibrosarcoma protuberans: Case report," Photodiagnosis and Photodynamic Therapy 35, 102351 (2021).
24. S. Wang, J. Zhao, H. Lui, Q. He, and H. Zeng, "In vivo near-infrared autofluorescence imaging of pigmented skin lesions: methods, technical improvements and preliminary clinical results," Skin Research and Technology 19(1), 20–26 (2013).
25. S. Kalia, J. Zhao, H. Zeng, D. McLean, N. Kollias, and H. Lui, "Melanin quantification by in vitro and in vivo analysis of near-infrared fluorescence," Pigment Cell & Melanoma Research 31(1), 31–38 (2018).
26. P. T. Tran, P. Tawornchat, B. Kleuser, S. B. Lohan, J. Schleusener, M. C. Meinke, and M. E. Darvin, "Red- and near-infrared-excited autofluorescence as a marker for acute oxidative stress in skin exposed to cigarette smoke Ex Vivo and In Vivo," Antioxidants 12(5), 1011 (2023).
27. M. Emanuelli, D. Sartini, E. Molinelli, R. Campagna, V. Pozzi, E. Salvolini, O. Simonetti, A. Campanati, and A. Offidani, "The double-edged sword of oxidative stress in skin damage and melanoma: From physiopathology to therapeutical approaches," Antioxidants 11(4), 612 (2022).
28. M. Pietruszewska, G. Biesiada, J. Czepiel, M. Birczyńska, P. Moskal, M. Kozicki, E. Hola, A. Garlicki, and A. Wesełucha-Birczyńska, "Lymphocytes studied by Raman microspectroscopy," Chapter 6 in Lymphocytes, E. S. Istifli, H. B. İla (Eds.), IntechOpen (2019). eBook ISBN: 978-1-83881-749-7.
29. M. Pietruszewska, G. Biesiada, J. Czepiel, M. Birczyńska-Zych, P. Moskal, A. Garlicki, and A. Wesełucha-Birczyńska, "Raman spectroscopy of lymphocytes from patients with the Epstein–Barr virus infection," Scientific Reports 14(1), 6417 (2024).
30. W. H. Clark, "From the melanocyte to melanoma to tumor biology," Advances in Cancer Research 65, 113–140 (1194).
31. Z. Huang, H. Lui, X. K. Chen, A. Alajlan, D. I. McLean, and H. Zeng, "Raman spectroscopy of in vivo cutaneous melanin," Journal of Biomedical Optics 9(6), 1198 (2004).
32. B. R. Uslu, B. Ozdil, E. Tarhan, S. Özçelik, H. Aktuğ, and G. Güler, "Vibrational spectroscopy unveils distinct cell cycle features of cancer stem cells in melanoma," Scientific Reports 15(1), 28494 (2025).
33. Z. Movasaghi, S. Rehman, and I. U. Rehman, "Raman spectroscopy of biological tissues," Applied Spectroscopy Reviews 42(5), 493–541 (2007).
34. W. H. Clark, D. E. Elder, and M. Van Horn, "The biologic forms of malignant melanoma," Human Pathology 17(5), 443–450 (1986).
35. A. A. Marghoob, K. Koenig, F. V. Bittencourt, A. W. Kopf, and R. S. Bart, "Breslow thickness and Clark level in melanoma: Support for including level in pathology reports and in American joint committee on cancer staging," Cancer 88(3), 589–595 (2000).
36. O. Vița, A. Jurescu, A. Văduva, R. Cornea, M. Cornianu, S. Tăban, D. Szilagyi, C. Micșescu, B. Natarâș, and A. Dema, "Invasive cutaneous melanoma: Evaluating the prognostic significance of some parameters associated with lymph node metastases," Medicina 59(7), 1241 (2023).
37. M. Prodan, S. Costescu, A. Elagez, S. M. D. Laitin, V. Bloanca, Z. Crainiceanu, E. Seclaman, A.-O. Toma, R. M. Fericean, G. Puenea, and G. V. Cozma, "Molecular markers in melanoma progression: A study on the expression of miRNA gene subtypes in tumoral vs. benign nevi," Current Oncology 31(5), 2881–2894 (2024).
38. Y. Li, J. M. Krahn, G. P. Flake, D. M. Umbach, and L. Li, "Toward predicting metastatic progression of melanoma based on gene expression data," Pigment Cell & Melanoma Research 28(4), 453–463 (2015).
39. S. J. Kirkpatrick, R. K. Wang, D. D. Duncan, M. Kulesz-Martin, and K. Lee, "Imaging the mechanical stiffness of skin lesions by in vivo acousto-optical elastography," Optics Express 14(21), 9770 (2006).

Neural Networks for Medical Data Processing: Segmentation of Fluorescence Lifetime Imaging Microscopy

Ilya Shchechkin[1,2*], Svetlana Rodimova[1], Artem Mozherov[3], Vadim Elagin[1], Nikolai Bobrov[4], Vladislav Shcheslavsky[1], Vladimir Zagainov[4,5], Elena Zagaynova[1,6], and Daria Kuznetsova[1,3]

[1] Privolzhsky Research Medical University, Institute of Experimental Oncology and Biomedical Technologies, 10/1 Minin and Pozharsky sq., Nizhny Novgorod 603950, Russian Federation

[2] N.I. Lobachevsky Nizhny Novgorod National Research State University, 23 Gagarina ave., Nizhny Novgorod 603022, Russian Federation

[3] I.M. Sechenov First Moscow State Medical University, Moscow 119991, Russian Federation

[4] The Volga District Medical Centre of Federal Medical and Biological Agency, 14 Ilinskaya str., Nizhny Novgorod 603000, Russian Federation

[5] Nizhny Novgorod Regional Clinical Oncologic Dispensary, 11/1 Delovaya str., Nizhny Novgorod 603126, Russian Federation

[6] Lopukhin Federal Research and Clinical Center of Physical-Chemical Medicine of Federal Medical Bio-logical Agency, 1a Malaya Pirogovskaya str., Moscow 119435, Russian Federation

*e-mail: Iliahasa1992@gmail.com

Abstract. Fluorescence lifetime imaging microscopy (FLIM) is a powerful tool for visualizing the distribution of fluorescence lifetimes of fluorophores within a tissue, and is used for optical metabolic imaging. However, processing the large volumes of data generated by FLIM can be time-consuming and challenging for an untrained operator. Convolutional neural networks (CNNs) have demonstrated its effectiveness for tissue image and FLIM segmentation, making them a promising tool for automated analysis of FLIM images. The article presents a method for segmenting FLIM images of liver tissue during the regeneration using a CNN based on the UNet++ architecture. The CNN was trained to detect cell boundaries and nuclei, and the resulting masks were used to approximate the fluorescence decay curves for the FLIM-image data. The results show that the CNN is effective in segmenting FLIM images of cells and tissues, and obtaining fluorescence decay curves. The use of CNNs and other machine learning methods in medical image segmentation and analysis will improve and speed up diagnosis and reduce diagnostic errors.

Keywords: deep learning; segmentation; convolutional neural networks; FLIM; liver regeneration; multiphoton microscopy.

Paper #9278 received 30 May 2025; revised manuscript received 22 Jul 2025; accepted for publication 2 Aug 2025; published online 21 Sep 2025. doi: 10.18287/JBPE25.11.030304.

1 Introduction

Fluorescence lifetime imaging microscopy (FLIM) is a powerful tool for visualization of the distribution of fluorescence lifetimes of fluorophores within a tissue. It enables researchers not only to differentiate fluorophores, but also, more importantly, to probe their environment, since the fluorescence lifetime of a fluorophore depends on the pH, viscosity, temperature and other physicochemical parameters of the region of the medium in which it is located. One of the most important applications of FLIM is for optical metabolic imaging. This is based on measurements of the decay kinetics of endogenous fluorophores such as NAD(P)H and FAD, which participate in redox reactions in a cell and, accordingly, reflect its metabolic status [1].

To describe the decay of NAD(P)H fluorescence, bi-exponential or tri-exponential approximation models are usually used, where the parameters t_1, t_2 and t_3 correspond to the lifetimes of the free, bound and phosphorylated forms of NAD(P)H, respectively, and their contributions are described by the relative amplitudes a_1, a_2 and a_3. Changes in the NAD(P)H fluorescence decay curves can therefore serve to indicate metabolic changes: while an increase in a_1 correlates with an increase in anaerobic glycolysis, an increase in a_2 is associated with an increase in oxidative phosphorylation, and a change in a_3 corresponds to changes in the intensity of the synthetic processes in the cells. FLIM generates a large amount of information – the times of registration of photons, their number, as well as data on the coordinates of where the photons are recorded. Processing such large volumes of data can be time-consuming and challenging for an untrained operator.

Neural networks are increasingly being used in medical data analysis due to their ability to learn complex patterns and relationships in large data sets. In particular, convolutional neural networks (CNNs) have demonstrated significant success in tissue image and FLIM segmentation [2, 3].

A CNN is a type of deep learning algorithm that can automatically learn features from images and classify them into different categories. This type of algorithm is particularly well suited to image segmentation problems, where the goal is to divide an image into different regions based on their contents. CNNs have previously been shown to be effective in segmenting liver tissue as seen in multiphase CT images [4].

Liver tissue segmentation is an important task in medical imaging because it enables the detection and diagnosis of early metabolic changes associated with liver diseases such as hepatocellular carcinoma (HCC) [4]. Traditional tissue segmentation methods rely on manual annotation, which is time-consuming and prone to human error. FLIM, on the other hand, produces large data sets that may contain ambiguous objects to assess, which can make processing difficult for the operator.

A promising task is to develop an algorithm for automatic image analysis of FLIM microscopy to improve the clinical diagnosis of metabolic changes in tissues in the analysis of various conditions, disease development, tumor growth, and treatment response. In the case of scientific research, in turn, the development of a method for analyzing large amounts of data is required, which can be solved by developing automated algorithms.

The objective of the work is to develop an algorithm for automated analysis of FLIM images for subsequent software development.

FLIM image analysis using neural networks can be performed in various ways. Using neural networks to calculate the fluorescence decay parameters for all pixels in an image, or by segmenting and then calculating the decay parameters either based on an approximation, in SPCImage, or based on the results of parameter calculations using neural networks, or by approximating the decay curves using a separate curve approximator. In this paper, we consider the development of an algorithm for analyzing FLIM images of liver tissue during regeneration against the background of pathology, based on the previously presented in Ref. [5]. CNN-based automated FLIM analysis methods have been applied for the first time to a complex *in vivo* model.

2 Materials and Methods

2.1 FLIM Data Processing

To study the possibility of employing automated analysis of FLIM images using CNN, it was decided to analyze the effectiveness of automatic processing of images obtained from FLIM data arrays for various study samples derived with this method.

Models of liver regeneration with pathologies (fibrosis and steatosis) were selected as such samples.

Data from the studied samples had previously been processed manually and had also had metabolic changes confirmed on the basis of other methods (histology, molecular analysis) [6]. From comparisons with the manually processed data, conclusions were drawn regarding the feasibility of such automated processing.

Since specific fluorescence parameters obtained from manual and automatic processing may differ markedly from each other due to limitations of fitting, it was decided to compare the ability to detect identical patterns of changes in metabolic status at different time points, rather than to use absolute values, for the variants of manual and automatic processing. The coincidence of global changes in metabolic parameters (relative contributions to the mean time) was thus considered as a sign of the effectiveness of the automatic analysis.

The criterion for change in the metabolic status of each studied object was taken as any significant difference between the fluorescence lifetime parameters (t_1, t_2, t_3, a_1, a_2, a_3) at different time points of the study.

FLIM images were labeled (segmented) using ImageJ (Fiji) into three classes, class 1 representing the cell boundary, class 2 the nucleus boundary, class 0 everything else. To train a CNN to detect the cells, three mask variants were used: cell borders, complete cells, background without cells.

To carry out automated analysis, a convolutional neural network was trained, for which the UNet++ architecture was chosen that used a multi-component loss function consisting of the BCE, Focal and Dice functions. The CNN was trained in a three-channel format, receiving all previously designated mask options as its input. The following quality metrics were used: area under the curve (AUC) and the F_1-metric.

A separate CNN was also trained to identify cell nuclei and subsequently to exclude them from the analysis. BCE was used as the loss function; the area under the curve (AUC) and F_1-metric were used as quality metrics.

The images were additionally filtered by brightness to exclude bright areas (vitamin A and lipofuscin) from the analysis. Using the Otsu method with two thresholds, its own thresholds were automatically selected for each image, since there is a difference in intensity among the images.

The resulting predictions were used for cell-by-cell segmentation of the corresponding images. The segmentation results were then used as fields to perform cell-by-cell analysis of the fluorescence decay of each image using an exponentially modified Gaussian function, effectively describing bi-exponential and tri-exponential decay models. For each cell, the coefficients of the fluorescence decay curve equation were calculated, on the basis of which the fluorescence lifetime parameters could be determined.

Visual Studio Code (Microsoft, Washington, U.S.) was used as the analysis environment; Python (Python Software Foundation, Delaware, U.S.) was used as the programming language.

2.2 Model of Liver Regeneration

Wistar rats (28 individuals) were used as model objects. To model pathologies, two options were chosen: fibrosis was induced by intraperitoneal injection of a 30% oil solution of CCl4; steatosis was induced by a high-calorie fatty diet, 60% fat in the total diet of the animal. Induction of liver regeneration was initiated by 70% partial hepatectomy, followed by monitoring the regeneration process on days 3 or 7 after hepatectomy, with FLIM imaging at both stages.

To train the CNN, 330 FLIM images of rat liver tissue at various stages of regeneration were used.

The animals were kept before and after the operation in accordance with the rules adopted by the European Convention for the Protection of Vertebrate Animals; and according to the National Institutes of Health Guide for the Care and Use of Laboratory Animals (NIH Publications no. 8023, revised 1978) and also in compliance with the ARRIVE guidelines. The local ethics committee at the Privolzhsky Research Medical University (protocol №15; date: 23.09.2022) approved all the animal procedures.

2.3 CNN Training

A convolutional neural network model was selected for cell-by-cell image segmentation. Threshold segmentation methods are not suitable for this model due to the high intensity heterogeneity, which is associated with the presence of different objects within the same intensity boundaries. Two architectures, UNet and UNet++, were selected as possible options for segmentation [6]. The UNet architecture is a standard variant of biomedical image segmentation due to its high accuracy and ease of implementation, in turn, its modification UNet++, according to literary sources, is one of the most accurate segmenters for biomedical images, although it has a large volume of parameters and training time [7]. Unlike monolithic transformers or context-focused models, like DeepLab, which is better for natural images or ResUNet better for volumetric data, UNet++ offers adaptive precision-speed control and seamless extensibility.

ReLU and ELU were considered as activation functions. BCE, Focal, and Dice were considered as error functions. Various combinations of these options were tested. Training was conducted over 1000 epochs in 10 steps. The F_1 score (Dice metric) was used to evaluate the quality of segmentation.

The UNet++ model, which uses ELU as an activation function and a multicomponent error function, was found to be more computationally complex than the UNet model with ReLU and the BCE error function. As a result, the size of the UNet++ model increased by a factor of 3, from about 35 Mbits for UNet to about 100 Mbits for UNet++. Similarly, the training time for the UNet++ model also increased significantly.

Comparison of architectures is presented in Table 1.

Table 1 Comparison of accuracy of different combinations of segmentation techniques.

Architecture	Activation function	Loss function	F_1-metric
UNet	ReLU	BCE	0.619
UNet++	ReLU	BCE	0.637
UNet++	ELU	BCE	0.649
UNet++	ELU	BCE+Focal	0.664
UNet++	ELU	BCE+Dice	0.671
UNet++	ELU	Dice+Focal	0.689
UNet++	ELU	BCE+Focal+Dice	0.703

Images for CNN training were augmented; areas containing the objects under study were selected from the images, after which the areas were cropped and re-reflected. In this way, a higher resolution image was obtained, individual sections of which were used as different images to increase the volume of training material and the density of objects in the image. Thus, 988 images were accumulated.

The collected images were divided into training and validation sets. The training set was assigned 70% of the images, while the validation set received 30%. Previously accumulated images of normal liver tissue samples were used as a test set.

These images, with applying standard image augmentation techniques (height and width shift, reflection, rotation, horizontal and vertical flip, zoom), were used to train a convolutional neural network based on the UNet++ architecture using a multi-component loss function.

The UNet++ architecture is an encoder-decoder network that nests smaller-depth encoder-decoder layers to reduce the semantic gap between the encoder and decoder feature maps.

Hyperparameters were selected for neural network training. Adam was used as an optimization algorithm

with a learning rate of 0.0001. Due to the limited amount of memory, the batch size was set to 10. Dropuot was used as a regularization method. Early stopping of learning was not used. As a loss function, used to control the quality of model training, a multicomponent function was used; it is a sum of BCE, Focal and Dice loss functions.

The BCE loss function calculates the binary cross entropy, compares the predicted result for each pixel with the real value of 0 or 1, and then calculates a score that penalizes differences between the real and predicted values.

The Focal loss function is a modified version of the BCE function for use in cases with extreme class imbalance.

The Dice loss function is based on calculating the overlap between the predicted and true classes.

The result of using UNet++ is a semantic segmentation map, which should be divided into different objects of the same class using the instance segmentation method.

The classic 'watershed' algorithm was used as an instance segmentation method; this algorithm works by filling a space with known boundaries (cell edge segmentation mask) based on individual markers (whole cell segmentation mask), until the moment of overlapping, at which division into segments occurs. The parameters used by the algorithm (markers of objects, distance between objects) were selected automatically. No significant over- or under-segmentation was detected during image analysis. If there were too small objects on the masks, they were deleted.

The CNN for determining cell boundaries was trained for 1000 epochs, of 10 steps each; the multi-component loss coefficient was 0.6; Focal Loss was 0.075; Dice Loss was 0.22, with an F_1 (Dice) metric of 0.7 (precision was equaled to 0.64 and recall was 0.8), IoU of 0.51, accuracy of 0.76 and AUC of 0.9.

The CNN for kernel detection was trained for 1000 epochs; the F_1 (Dice) metric was 0.65 (precision was equaled to 0.36 and recall was 0.96), IoU of 0.4, accuracy of 0.96 and AUC of 0.98.

The relatively low accuracy of the segmenter is associated with the identification of previously unmarked objects, which was confirmed during manual image verification.

In the case of nuclear detection, a large number of false positive results indicate the detection of rounded low-intensity objects, these may be the lipid droplets or tissue damage. Segmented nuclei or similar objects are removed from the analysis, regardless of whether they are nuclei or other objects of no interest.

In this way, high-accuracy models were trained.

2.4 Segmentation

Using the watershed algorithm, the resulting masks were segmented to obtain individual cell masks for the image. Next, a combined mask was obtained for each cell, including only the cytoplasm of cells of a certain brightness and excluding the nuclei and areas of vitamin A (or lipofuscin) of increased brightness.

The masks were then used as ROIs to approximate the fluorescence decay curves for the FLIM-image data corresponding to this mask, based on an exponentially modified Gaussian function.

For steatosis, 11367 individual decay curves were obtained.

For fibrosis, 9607 individual decay curves were obtained.

Manual processing of this volume of images resulted in 5370 and 3138 decay curves for the steatosis and fibrosis variants, respectively.

2.5 Curve Fitting

The approximation of the curves to calculate the fluorescence decay parameters was carried out based on an exponentially modified Gaussian function, the equivalent form of which is suitable for describing the decay of exponentials:

$$f(x;h;\mu;\sigma;\tau) = \frac{h\sigma}{\tau}\sqrt{\frac{\pi}{2}}exp\left(\frac{1}{2}\left(\frac{\sigma}{\tau}\right)^2 - \frac{x-\mu}{\tau}\right)\times \\ \times erfc\left(\frac{1}{\sqrt{2}}\left(\frac{\sigma}{\tau} - \frac{x-\mu}{\tau}\right)\right).$$

where h – Gaussian amplitude; μ – mean Gaussian value; σ – Gaussian standard deviation; λ – exponent values; τ – relaxation time of the exponent, which is calculated:

$$\tau = \frac{1}{\lambda},$$

and *erfc* is a complete function error:

$$erfc(x) = 1 - erf(x) = \frac{2}{\sqrt{\pi}}\int_x^\infty e^{-t^2}dt.$$

The FLIM parameters were calculated on the basis of the values: h, and λ obtained during the approximation, based on the functions:

$$t_n = \frac{1}{\lambda_n} = \tau_n,$$

$$a_n^{absolute} = \frac{h_n}{t_n},$$

$$a_n^{relative} = \frac{100*a_n^{absolute}}{\sum a_n^{absolute}},$$

$$t_{mean} = \sum a_n \cdot t_n.$$

The initial parameters of the approximation model corresponded to the values obtained for normal liver tissue during manual processing. The a_1, a_2, and a_3 parameters were 60%, 30%, and 10%, respectively, while the t_1, t_2, and t_3 parameters were 0.4, 2.5, and 6 ns, respectively. The parameters were limited to a 50% range of the set value.

The chi-squared metric was used as a metric of approximation accuracy, with the maximum possible threshold value of 1.5.

2.6 Image Processing

Examples of FLIM images are presented in Fig. 1. The stages of operation of the segmenter are also presented in Fig. 1.

When studying metabolic changes in tissues using the FLIM method, three forms of NAD(P)H are used: the free, bound and phosphorylated forms. These are represented by the following decay parameters: their relative contributions to the total decay time a_1, a_2, and a_3 and their absolute values of decay time t_1, t_2, and t_3, respectively. These parameters are calculated by approximating each decay curve based on an exponential Gaussian function for the 3 components. In this case, the parameter $a_3(t_3)$ actually makes only a very small contribution to the approximation of the function, but at the same time it can change the distribution of the two remaining parameters. Therefore, this parameter is an important marker of changes in metabolic status, as it is associated with the phosphorylated form of NADPH, which is involved in the synthetic function of the tissue [7]. Thus, it is important to perform FLIM decay parameter distribution analysis for both the two-component and three-component automatic analysis options (Fig. 2).

It was shown that the decay tails differ for 2 and 3 component approximation variants. The images show that the tail for the three-component approximation fits the data better, although not significantly (Fig. 2).

As a result of the analysis, it was shown that the parameter values for options with two and three components at time points: 0, 3, 6, 9, and 12 weeks of steatosis development, for parameters a_1 and a_2 are similar, which indicates a weak influence of the use of parameter $a_3(t_3)$ on the result of the analysis of the remaining components, which in turn allows the use of a three-component analysis option in the future without loss of accuracy (Fig. 3A, Fig. 4B).

Using the average results of the metabolic parameters for each image is a more representative option for analysis due to the significant leveling of outliers and, in some cases, a reduction of the scatters, but the option of cell-by-cell analysis is more representative of the entire sample (Fig. 3B, Fig.4B).

The results of the analysis are presented in Figs. 2 and 3, Table SI and Table SII.

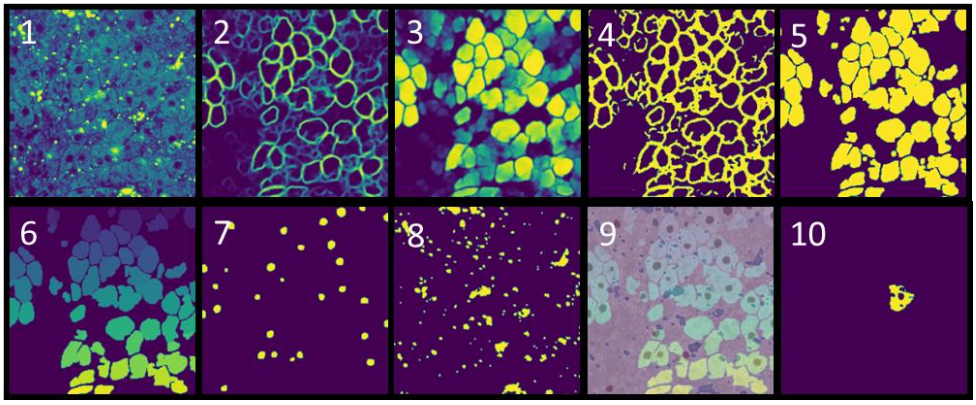

Fig. 1 Stages of image processing to obtain cell masks: 1 – FLIM image; 2 – detected cell boundaries; 3 – detected cells; 4 – boundaries selected relative to the threshold; 5 – cells selected relative to the threshold; 6 – processed cells separated by the watershed algorithm; 7 – detected cell nuclei; 8 – bright areas of inclusions in the image; 9 – joint mask for the image; 10 – mask for one cell, excluding nucleus and bright inclusions.

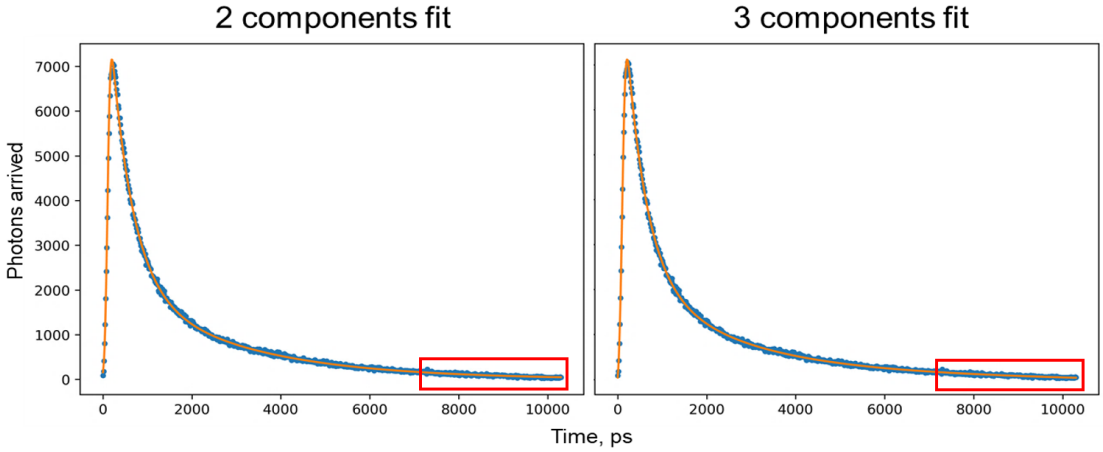

Fig. 2 Results of automatically fitting procedure for 2 and 3 components fitting, for the same sample: blue dots − real fluorescence decay data; orange curve − curve of the approximation function of real data; red box − tail part of the function, for the position of which the third component is responsible.

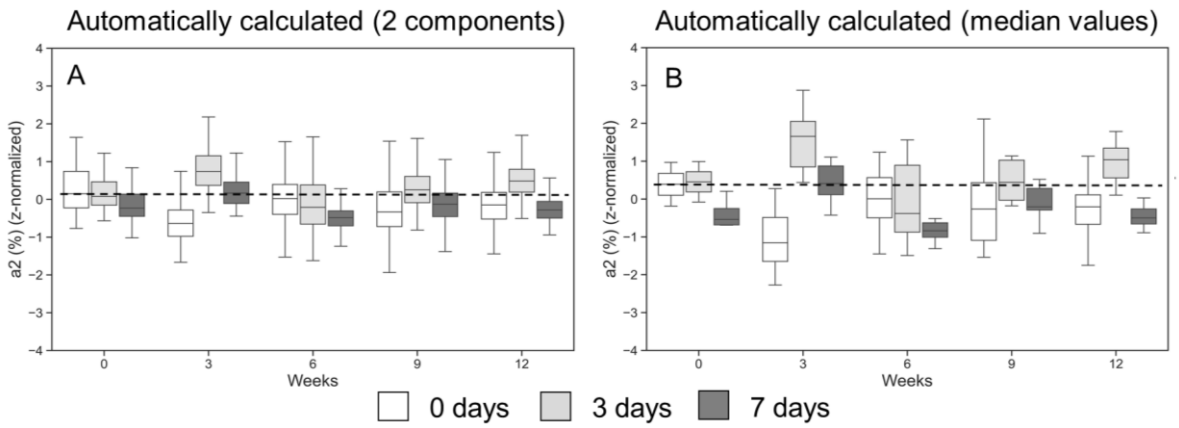

Fig. 3 Graphs of z-normalized values of parameter a_2 for fluorescence decay for (A) automatically calculated steatosis with 2 components fitting, (B) automatically calculated steatosis with median values for each image analyzed. The dotted line is the median of the data for 0 days and 0 weeks.

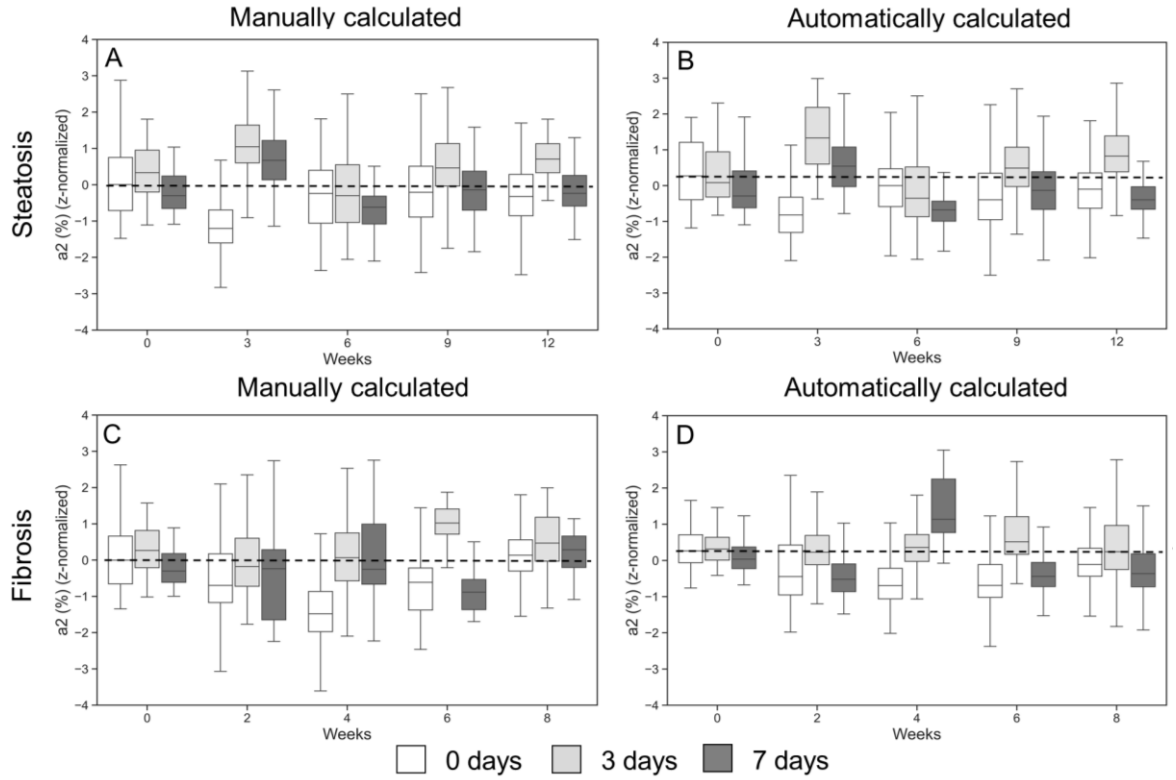

Fig. 4 Graphs of z-normalized values of parameter a_2 for fluorescence decay for different models of metabolic shift, calculated manually or automatically: (A) Manually calculated steatosis, (B) Automatically calculated steatosis, (C) Manually calculated fibrosis, (D) Automatically calculated fibrosis. The dotted line is the median of the data for 0 days and 0 weeks.

3 Results

Our assessment of the possibility of using the automatic method for analyzing FLIM images was carried out using data cell-by-cell, for the automatic version, and by field, for the manual analysis version; the fields conditionally correspond to cells, although they covered 10–20% of the cytoplasm.

When processing steatosis data, the dispersion (Q3–Q1, since the data are not normally distributed) were statistically significantly different, with a *p*-value of 0.01395 (Mann-Whitney *U*-test, since the data are not normally distributed), whereas the dispersion of the automatically processed data was smaller. Since liver tissue steatosis is a diffuse disease that manifests equally throughout the liver tissue, a decrease in dispersion during processing indicates an increase in the constancy of finding objects with similar characteristics, and may also be the result of a significant increase in the number of objects processed [8].

Fibrosis data with automatic processing have the same dispersion as with manual processing, with a *p*-value of 0.5112. Since in fibrosis, liver tissue is heterogeneous and characterized by the presence of fibrous septa, areas of necrosis and pathological regeneration nodes, stable results are unlikely due to the presence of a large number of different metabolic conditions in hepatocytes, which is also leads to an increase in outliers.

The automatically processed data contains more outliers, which is the result of a decrease in data dispersion. In the graph, to remove outliers, the automatic processing data was filtered by the 5th and 95th percentiles; the data dispersion remained unchanged.

For the automatic data processing option, the patterns of changes at different time points did not differ from those obtained with manual processing, as shown by our statistical tests.

The values of the parameter contributions, i.e. the parameters a_1, a_2 and a_3, differ relatively for automatic and manual calculation by 4.628 ± 3.474%, which is an insignificant difference. The difference in absolute values is due to the difference in the approximation procedure between the SPCImage and the approximation process based on the exponentially modified Gaussian function, which constantly selects components of greater length. The difference in absolute values does not affect the results of analysis due to equivalently changes in contributions between different metabolic statuses and their overall equality.

To assess the compliance of the automatic and manual processing options, a test of the compliance of the mutual distribution of various points of the regeneration process against the background of pathology was carried out. All variants of metabolic states were compared with each other using the Dunn test with Benjamini-Hochberg multiple comparison correction, since the data distribution was statistically significantly different from normal. During the comparison, a matrix was obtained, which indicated the differences between the variants of metabolic states or their absence. During such a comparison for the automatic version of curve analysis and when comparing the results with the manual processing option, error matrices were obtained on the basis of which the precision, recall and F_1 metrics were calculated.

It was shown that for the variant of steatosis pathology development, precision is 0.802, recall is 0.975, F_1 is 0.880, and for the variant of cirrhosis development, precision is 0.731, recall is 0.895, F_1 is 0.805.

The results of the analyses are presented in Fig. 4, Table SI and Table SII.

4 Discussion

Neural networks are currently widely used to facilitate, accelerate, and automate the processing of large volumes of data, including for the analysis of FLIM images.

One example of a CNN-based tool for tissue segmentation is U-SegNet, a full convolutional neural network that has been used to segment brain tissue in MRI images. U-SegNet is a hybrid of two widely used deep learning segmentation architectures, U-Net and SegNet, and has been shown to outperform traditional (manual) brain tissue segmentation methods [3].

Another example is GNN-SEG, a graph-based neural network method also used for brain tissue segmentation; this approach uses to capture the spatial relationships between different brain regions [9].

In addition, a deep learning approach has been proposed for liver and tumor segmentation in CT images using ResUNet [4, 10, 11].

There is a CNN for wound segmentation, which has achieved high accuracy and efficiency, and is applicable to the segmentation of four different types of wound [12].

A neural network model has also been developed to classify stem cells of mesenchymal origin, based on their biomechanical properties [13].

A deep 3D neural network has also been applied to segment brain structures. It used self-monitoring modules to analyze 3D MRI images [14, 15]. The manual segmentation of such magnetic resonance images relies on the use of a highly trained operator to isolate different types of brain structure. The use of neural networks helps automate this process and increases the accuracy and efficiency of segmentation of the brain structures. Applying segmentation to neonatal brain tissue has also been explored for this task [16].

Applicable to FLIM microscopy, research [2] demonstrated the use of a denoising convolutional network to improve the signal-noise ratio (SNR) of the FLIM technique, based on a fast acquisition FLIM system that processes analog signals with large SNRs obtained with the use of highly-efficient pulse modulation.

In addition, for FLIM analysis, Hu et al. proposed an automatic method for segmenting FLIM cell images using multi-resolution community detection (MCD); the method is effective for such segmentation [17].

Another study has demonstrated machine learning methods for the label-free detection of microglia, based on FLIM [15]. The study showed that machine learning methods can be used to better interpret endogenous fluorescent cellular signals in order to characterize microglia, and that this approach can also be extended to other cell types.

In this work, we used the U-Net++ convolutional neural network, which is capable of determining the boundaries of objects with high accuracy. This method has previously shown the value of such accuracy in segmenting medical images of various origins: CT, MRI, microscopy [18].

Our work has demonstrated the high efficiency of applying deep learning methods to segmenting FLIM images; it being shown that automatic image processing not only preserves the characteristics of manual processing in terms of quality, but even surpasses it in coverage of the studied material and in the stability of the results. Similar results have been observed in other studies [19]. In this regard, the use of automatic methods

for analyzing FLIM images is therefore a suitable solution for processing large volumes of data and for express studies of individual samples.

In addition to the possibility of rapid assessment of the liver condition [6, 7, 20], the FLIM method has also proven effective for determining the boundaries of tumor resection [21] and for evaluating the effectiveness of stem cell differentiation in different directions [22, 23]. The algorithm we have developed, in turn, makes it possible to simplify, accelerate and unify the process of processing FLIM data at the cellular level with high spatial and temporal resolution, eliminating the human factor. In particular, the processing time was reduced from 5−15 min to 5−15 s. In the future, software will be developed to improve the usability of the algorithm and create a universal effective tool for a range of applications both in laboratory research and in the clinic.

Using CNNs to analyze medical data has several advantages. First, they can facilitate, speed up, and automate the processing of large volumes of such data, which can be time-consuming and error-prone if done manually. Second, they can improve the accuracy and consistency of medical diagnoses because of their ability to learn from large data sets and generalize these in a way that can be applied to new cases. Third, they can reduce the workload of healthcare professionals, allowing them to focus on more complex tasks that require human expertise [24].

5 Conclusion

FLIM microscopy is widely used to study metabolic changes at the cellular and subcellular levels of various cells and tissues in various physiological and pathological conditions. In this regard, the development of new methods for automating FLIM image processing is an important aspect of the development of diagnostic methods.

A promising direction for solving this problem is the use of neural networks for automatic segmentation of objects of interest on FLIM images and their subsequent analysis.

In this work, we show that the application of neural networks to the task of analyzing metabolic changes in liver tissue during regeneration with pathology corresponds to the quality of the results processed manually. The automated algorithm makes it possible to speed up, standardize and unify the analysis. Although the obtained results look promising, the methods of machine learning and artificial intelligence have their limitations, primarily related to the human factor. The results obtained by the neural network contain artifacts embedded in the learning process, which can only be eliminated by increasing the training sample and introducing a strict data preprocessing protocol. At the same time, the speed of obtaining results, although significantly higher than with manual processing, does not include the time spent on training the neural network and preprocessing the data. In turn, the results of the approximator require fine-tuning.

The obtained results allow us to perform an analysis of metabolic activity, tested, at the moment, only on the model of liver regeneration against the background of pathology, which will allow, in the future, to develop software based on the developed algorithm to create a tool for researches and clinic.

Funding

The work was supported by the Russian Science Foundation Grant №23-15-00421 (metabolic imaging and FLIM analysis), the Russian Science Foundation Grant №24-75-10007 (development of automatized segmentation approach).

Disclosures

The authors declare no conflicts of interest.

Data Availability

Data underlying the results presented in this paper are not publicly available at this time but may be obtained from the authors upon reasonable request.

References

1. W. Becker, “Fluorescence lifetime imaging – techniques and applications,” Journal of Microscopy 247(2), 119–136 (2012).
2. V. Mannam, Y. Zhang, X. Yuan, T. Hato, P. C. Dagher, E. L. Nichols, C. J. Smith, K. W. Dunn, and S. Howard, “Convolutional neural network denoising in fluorescence lifetime imaging microscopy (FLIM),” in Multiphoton Microscopy in the Biomedical Sciences XXI, A. Periasamy, P. T. So, K. König (Eds.), SPIE Proceedings 11648, 116481C (2021).
3. P. Kumar, P. Nagar, C. Arora, and A. Gupta, “U-Segnet: Fully convolutional neural network based automated brain tissue segmentation tool,” 25th IEEE International Conference on Image Processing (ICIP) (IEEE, 2018), 3503–3507 (2018).
4. F. Ouhmich, V. Agnus, V. Noblet, F. Heitz, and P. Pessaux, “Liver tissue segmentation in multiphase CT scans using cascaded convolutional neural networks,” International Journal of Computer Assisted Radiology and Surgery 14(8), 1275–1284 (2019).
5. E. A. Shirshin, M. V. Shirmanova, A. V. Gayer, M. M. Lukina, E. E. Nikonova, B. P. Yakimov, G. S. Budylin, V. V. Dudenkova, N. I. Ignatova, D. V. Komarov, V. V. Yakovlev, W. Becker, E. V. Zagaynova, V. I. Shcheslavskiy, and M. O. Scully, “Label-free sensing of cells with fluorescence lifetime imaging: The quest for metabolic

heterogeneity," Proceedings of the National Academy of Sciences of the United States of America 119(9), e2118241119 (2022).
6. S. Rodimova, N. Bobrov, A. Mozherov, V. Elagin, M. Karabut, I. Shchechkin, D. Kozlov, D. Krylov, A. Gavrina, V. Zagainov, E. Zagaynova, and D. Kuznetsova, "Optical biomedical imaging reveals criteria for violated liver regenerative potential," Cells 12(3), 479 (2023).
7. S. Rodimova, D. Kuznetsova, N. Bobrov, V. Elagin, V. Shcheslavskiy, V. Zagainov, and E. Zagaynova, "Mapping metabolism of liver tissue using two-photon FLIM," Biomedical Optics Express 11(8), 4458 (2020).
8. F. Nassir, R. S. Rector, G. M. Hammoud, and J. A. Ibdah, "Pathogenesis and prevention of hepatic steatosis," Gastroenterlogy and Hepatology 11, 167–175 (2015).
9. C. Wu, Z. Feng, H. Zhang, and H. Yan, "Graph neural network and superpixel based brain tissue segmentation," Proceedings of International Joint Conference on Neural Networks (IJCNN) (2022).
10. H. Rahman, T. F. N. Bukht, A. Imran, J. Tariq, S. Tu, and A. Alzahrani, "A deep learning approach for liver and tumor segmentation in CT images using ResUNet," Bioengineering 9(8), 368 (2022).
11. H. Zhang, K. Luo, R. Deng, S. Li, and S. Duan, "Deep learning-based CT imaging for the diagnosis of liver tumor," Computational Intelligence and Neuroscience 2022, 3045370 (2022).
12. D. Ramachandram, J. L. Ramirez-GarciaLuna, R. D. J. Fraser, M. A. Martínez-Jiménez, J. E. Arriaga-Caballero, and J. Allport, "Fully automated wound tissue segmentation using deep learning on mobile devices: Cohort study," Journal of Medical Internet Research Mhealth Uhealth 10(4), e36977 (2022).
13. E. M. Darling, F. Guilak, "A neural network model for cell classification based on single-cell biomechanical properties," Tissue Engineering Part A 14(9), 1507–1515 (2008).
14. C. Laiton-Bonadiez, G. Sanchez-Torres, and J. Branch-Bedoya, "Deep 3D neural network for brain structures segmentation using self-attention modules in MRI images," Sensors 22(7), 2559 (2022).
15. M. A. K. Sagar, K. P. Cheng, J. N. Ouellette, J. C. Williams, J. J. Watters, and K. W. Eliceiri, "Machine learning methods for fluorescence lifetime imaging (FLIM) based label-free detection of microglia," Frontiers in Neuroscience 14, 931 (2020).
16. Y. Ding, R. Acosta, V. Enguix, S. Suffren, J. Ortmann, D. Luck, J. Dolz, and G. A. Lodygensky, "Using deep convolutional neural networks for neonatal brain image segmentation," Frontiers in Neuroscience 14, 207 (2020).
17. D. Hu, P. Sarder, P. Ronhovde, S. Orthaus, S. Achilefu, and Z. Nussinov, "Automatic segmentation of fluorescence lifetime microscopy images of cells using multiresolution community detection—a first study," Journal of Microscopy 253(1), 54–64 (2014).
18. Z. Zhou, M. M. Rahman Siddiquee, N. Tajbakhsh, and J. Liang, "UNet++: A nested U-Net architecture for medical image segmentation," in Deep Learning in Medical Image Analysis and Multimodal Learning for Clinical Decision Support 11045, 3–11 (2018).
19. M. T. Duong, J. D. Rudie, J. Wang, L. Xie, S. Mohan, J. C. Gee, and A. M. Rauschecker, "Convolutional neural network for automated FLAIR lesion segmentation on clinical brain MR imaging," American Journal of Neuroradiology 40(8), 1282–1290 (2019).
20. E. V. Potapova, V. V. Shupletsov, V. V. Dremin, E. A. Zherebtsov, A. V. Mamoshin, and A. V. Dunaev, "In Vivo time-resolved fluorescence detection of liver cancer supported by machine learning," Lasers in Surgery and Medicine 56(10), 836–844 (2024).
21. M. V. Shirmanova, V. I. Shcheslavskiy, M. M. Lukina, W. Becker, and E. V. Zagaynova, "Exploring tumor metabolism with time-resolved fluorescence methods: from single cells to a whole tumor," Chapter 3 in Multimodal Optical Diagnostics of Cancer, V. V. Tuchin, J. Popp, and V. Zakharov (Eds.), Springer Cham, 133–155 (2020). eBook ISBN: 978-3-030-44594-2.
22. A. V. Meleshina, V. V. Dudenkova, A. S. Bystrova, D. S. Kuznetsova, M. V. Shirmanova, and E. V. Zagaynova, "Two-photon FLIM of NAD(P)H and FAD in mesenchymal stem cells undergoing either osteogenic or chondrogenic differentiation," Stem Cell Research & Therapy 8(1), 15 (2017).
23. S. A. Rodimova, A. V. Meleshina, E. P. Kalabusheva, E. B. Dashinimaev, D. G. Reunov, H. G. Torgomyan, E. A. Vorotelyak, and E. V. Zagaynova, "Metabolic activity and intracellular pH in induced pluripotent stem cells differentiating in dermal and epidermal directions," Methods and Applications in Fluorescence 7(4), 044002 (2019).
24. N. Shahid, T. Rappon, and W. Berta, "Applications of artificial neural networks in health care organizational decision-making: A scoping review," PLoS ONE 14(2), e0212356 (2019).

Construction of a Predictive Model for Assessing the Porosity of TiNi Materials Based on Sintering Parameters of Samples

Viktor V. Nikolaev[1], Tatiana B. Lepekhina[1], Georgii V. Malkin[1], Natalya A. Krivova[1], Denis A. Grigoriev[1], Alexander S. Garin[1], Ekaterina S. Marchenko[1,2], Maxim D. Khomenko[3], and Yury V. Kistenev[1*]

[1] Tomsk State University, 36 Lenin Ave., Tomsk 634050, Russian Federation
[2] Institute for Problems of Chemical and Energetic Technologies of the Siberian Branch of RAS, 1 Sotsialisticheskaja str., Biysk 659332, Russian Federation
[3] NRC "Kurchatov Institute", 1 Kurchatov Sq., Moscow 123182, Russian Federation
*e-mail: yuk@iao.ru

Abstract. Additive manufacturing of TiNi alloys has developed significantly in recent years. Such growth is due to the unique properties of the resulting designs − superelasticity, bending strength − stretching, corrosion, chemical and thermodynamic stability. In addition, three-dimensional (3D) printing technology significantly expanded the scope of use of this material in various applied areas from biomedicine (for printing implants and bone tissue engineering), to, for example, the automotive and aerospace industries. Despite the fact that 3D printing technology already has commercial solutions that allows producing complex-shaped structures, this area is in the stage of development. Of a particular interest is the optimization of printing process and the development of a quality control system (achieving the required parameters of porosity, roughness, minimizing defects such as cracks, contamination, delamination, surface and subsurface heterogeneities, surface quality, shrinkage, etc.). In this paper, an original non-destructive method for assessing the sintering temperature as an indirect measure of porosity of a material using optical coherence tomography (OCT) and machine learning methods is proposed. Random Forest Regression approach was used to predict depth maps and spatial statistics from the sintering temperature. The Random Forest model based on the first- and the second-order texture metrics of OCT images provided R^2 of about 0.95 for sintering temperature prediction.

Keywords: TiNi; porosity; biocompatibility; optical coherence tomography; machine learning.

Paper #9280 received 13 Jun 2025; revised manuscript received 3 Aug 2025; accepted for publication 21 Aug 2025; published online 28 Sep 2025. doi: 10.18287/JBPE25.11.030305.

1 Introduction

Alloys based on the intermetallic nickel-titanium compound (TiNi) have gained widespread use due to their unique combination of physical and mechanical properties, which allow successful resolution of various technical and medical challenges [1]. Shape memory effect, superelasticity, high corrosion resistance and biocompatibility make these materials highly attractive for creating devices and structures with enhanced or fundamentally new functionalities [2, 3]. Current technologies allow producing both monolithic and porous structures based on TiNi, each possessing its own set of functional and mechanical characteristics [4]. Porous TiNi alloys are of particular interest due to their extensive use in medicine, facilitated by their hysteresis properties similar to human biological tissues and their developed three-dimensional porous structure morphologically akin to bone tissue. Such characteristics contribute to effective biological integration of implants [1]. Powder metallurgy

methods have produced porous TiNi-based products applied in various medical fields, including oncology, dentistry and maxillofacial surgery [5, 6].

In calcium-hydride reduction method of TiNi-based powder production [7], initial titanium and nickel compounds are reduced by calcium (most commonly in the presence of calcium hydride), resulting in the formation of TiNi intermetallic powder. TiNi powder produced by this method typically exhibits a complex phase composition: in addition to the main TiNi phase (present in two structural states – high-temperature B_2 phase and martensitic B19'), secondary intermetallic phases enriched with titanium (Ti_2Ni) and nickel ($TiNi_3$) are detected, along with metastable phases such as Ti_3Ni_4 and oxide inclusions like Ti_4Ni_2 (O,N,C – oxycarbonitride).

The initial powders define the structural parameters and physical-mechanical properties of porous materials obtained by powder metallurgy techniques. The diffusion sintering method of ready-made TiNi powder allows producing material with a more homogeneous phase-chemical composition compared to materials synthesized by self-propagating high-temperature synthesis (SHS) or reactive sintering using titanium and nickel powders [8, 9]. A general tendency in sintering is a decrease in overall porosity with increased sintering conditions. Elevated sintering temperature enhances particle diffusion bonding (growth of "necks" between particles), leading to pore shrinkage and thus reducing the total porosity of the material [10]. Simultaneously, pore enlargement may occur as smaller pores partially merge into larger ones, as observed by the authors of study [11], where increasing sintering temperature from 950 °C to 1000 °C raised the average pore size from approximately 36 to 182 μm.

Reducing the size of the initial powder particles promotes more intense sintering and increased material density – a finer powder yields lower residual porosity compared to coarser powder under otherwise equal conditions [10]. Isothermal holding time has a similar effect: extending sintering time usually enhances the degree of sintering and reduces porosity due to further growth of contacts between particles. For example, a decrease in porosity from ~41% to ~39% when holding time increased from 2 to 6 min was shown [12].

TiNi-based alloys are extremely sensitive to melting temperature regimes: even slight variations in melting point or heating/cooling rates can profoundly influence the microstructure of the porous alloy, its physic-mechanical properties, and characteristics of martensitic transformations [1]. Therefore, control of thermal parameters during sintering – especially the exact maintenance of melting temperatures – determines the properties of porous TiNi-based materials.

Porosity is one of the key factors affecting the biocompatibility of materials with body tissues. Biocompatibility is the ability of a material to integrate with the patient's tissues without causing any adverse clinical reactions [13]. In addition, this applies to the stimulation of cellular and tissue reactions to achieve engraftment. Important biocompatibility characteristics ensuring the engraftment of implants are the absence of inflammation, necrosis and severe oxidative stress in the implantation area [14]. Biocompatibility is largely determined by the surface structure of the implant. Biocompatible materials should not cause pathological processes or enhance complications, should not have a carcinogenic effect on the body [15]. Porosity affects cell survival, providing space for their attachment and migration [5, 16]. The optimal pore size, which forms a rough surface of the biomaterial, has a positive effect on morphology and proliferation [17, 18]. It is widely recognized that pore size and porosity affect significantly the progression of osteogenesis [19]. The interconnected pore network provides sufficient permeability for the exchange of nutrients and metabolic waste between cells and the extracellular matrix (ECM). This promotes the osteogenesis process, including cell colonization, differentiation and ECM deposition [20].

When fabricating implants intended to replace lost bone areas or entire bone, it is necessary to consider the mechanical properties of biomaterials, which should match the mechanical properties of bone. Such implants should have high corrosion resistance to prevent implant wear. In Ref. [21], Ti scaffolds were fabricated in two porosity ranges (50% and 70%), so their mechanical properties could mimic those of cortical and trabecular bone. It was concluded that scaffolds with a pore size range of 45 to 106 μm have the best micro-architecture suitable for early stages of cell attachment. 3D titanium scaffolds with a pore size of 600 to 700 μm and a porosity of 70% to 90% was found to demonstrate favorable prospects for osteogenesis and restoration of bone defects [22].

The fundamental characteristic of porosity is the relative pore area. Some authors determine the pore volume, or construct a pore size distribution. For example, for an optical microscope, the pore area can be estimated relative to the total area of the sample. However, this characteristic does not take into account the pore depth distribution, and an approximate determination of the focus at the same point of different samples can affect the final result.

Various data processing methods are used for porosity analysis. A new model for predicting the porosity of TiNi alloy based on the Support Vector Machine (SVM) was proposed [23]. Gaussian process regression [24], multiple linear regression, random forest [25], and convolutional neural network [26] were used to predict porosity in material manufacturing. In a previous study [27], we used optical coherence tomography (OCT) to investigate the porosity of TiNi samples. Porosity is a fundamental property of the material that manifests as texture in an OCT scan, whereas sintering temperature is a process parameter that is not directly visualized. OCT was proven to be an alternative technique for evaluating the porosity of TiNi biomaterials. Researchers trained the SVM with a radial basis function kernel classifier based on the first- and the second-order statistics of OCT data to distinguish groups of TiNi samples. The classifier provided an accuracy of $95 \pm 5\%$ for two groups of TiNi samples

classification. This work demonstrated the effectiveness of machine learning (ML) methods for analysis the porosity of TiNi biomaterials, and it can be used to analyze the porosity of other biomedical materials as well. The combination of OCT and ML has been little studied and is not practically presented in the literature. Therefore, this study is relevant and promising.

Thus, the purpose of this work is to develop a predictive model for assessing the porosity of TiNi based on different sintering temperatures of the samples.

2 Materials and Methods

2.1 TiNi Preparation

Production of porous TiNi samples was carried out using diffusion liquid-phase sintering of TiNi powder grade PV–N55T45 (Fig. 1, Table 1), previously obtained by the calcium-hydride reduction method. Before sintering, the powder was dried in a laboratory vacuum oven at a temperature of 150–170 °C and residual pressure of 10^{-4} Pa for 4 h to remove adsorbed gases and moisture. The powder was then loaded without pressing into quartz tubes of 15 mm a diameter and a length of 100 mm, ensuring an initial bulk porosity of approximately 70%, necessary to achieve the optimal structure of the porous material.

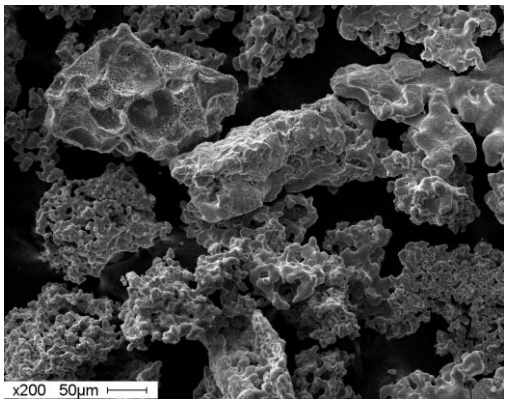

Fig. 1 Micrograph of powders: TiNi powder grade PV–N55T45.

The ends of the quartz tubes filled with powder were sealed with porous TiNi plugs produced by SHS. Subsequently, the tubes were placed into the working chamber of an electric vacuum furnace SNVE–1.31/16–I4 (Fig. 2).

Diffusion liquid-phase sintering was conducted at the following temperatures: 1230, 1240, 1250, 1260 and 1270 °C. Throughout the entire sintering process, the working chamber maintained a pressure of about $6.65 \cdot 10^{-4}$ Pa and the average heating rate of the samples was 10 °C/min. Upon reaching the target temperature, the samples were held isothermally for 15 min, after which heating was stopped, and the furnace was cooled to room temperature over 3 h. The sintered samples were then removed from the working chamber and extracted from the quartz tubes for further analysis.

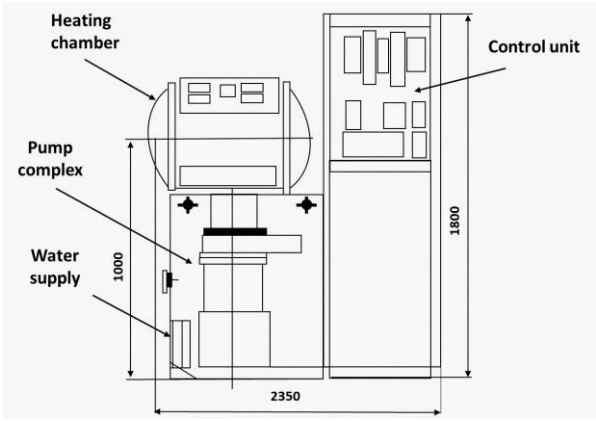

Fig. 2 Schematic diagram of the SNVE-1.31/16-I4 vacuum furnace.

2.2 OCT Protocol

The measurements were conducted using optical coherence tomograph GANIMEDE-II (Thorlabs, USA), which includes a basic scanning module OCTG-900 and super-luminescent diode with an operating wavelength of 930 ± 50 nm.

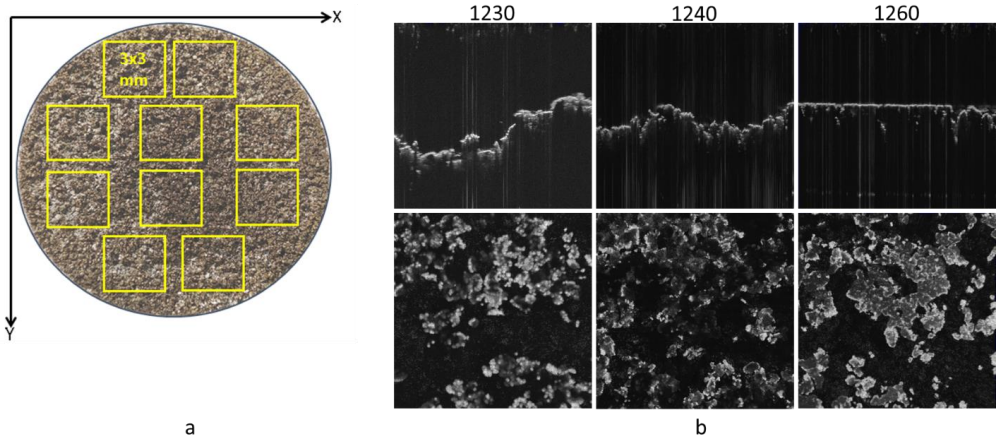

Fig. 3 (a) Schematic demonstration of disjoint scanning areas on the TiNi surface with size 3×3 mm, (b) examples B-scans (top) and C-scans (bottom) for test samples.

On the surface of the investigated sample TiNi, 3×3 mm area was highlighted using software ThorImageOCT 5.0.1, which was scanned with penetration depth up to 2.9 mm and the voxel size of 6×6×2.9 μm (the last parameter is the depth, *Z*-coordinate). Then the scan area was moved 10 times in parallel along the horizontal plane *XY* (Fig. 3(a)).

The scanning procedure was repeated on the lower edge of the sample. For a group of 5 samples sintered at different temperatures, 100 regions were scanned for all groups (in total, 500 regions). Examples of source data of images are shown in Fig. 3(b).

2.3 Data Preprocessing

For the analysis of TiNi sample's surfaces, a depth map method was applied. For every OCT A-scan from investigated area, *Z*-coordinate of its intensity maximum was determined, which corresponds to the boundary between air and metal at a point on a sample surface (Fig. 4).

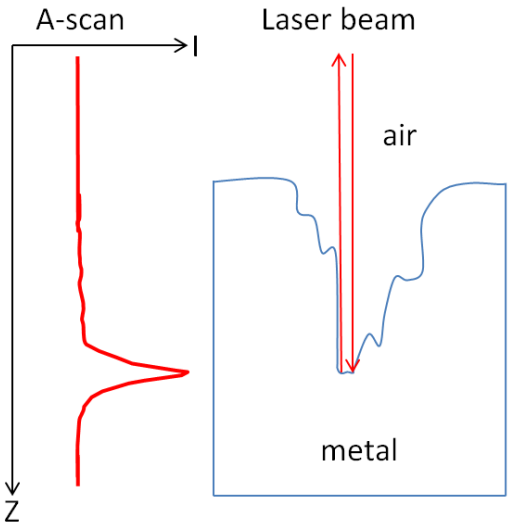

Fig. 4 Schematic representation of an OCT A-scan for TiNi sample and its intensity maximum, which corresponds to the boundary between air and metal.

For the *Z*-coordinates of the intensity maximum, their distribution was constructed and a 5-percentile value was calculated in the initial area corresponding to the boundary of the sample surface. Then, the maximal pore depth for all groups of samples was found, which was 1470 μm. Considering this, the depth map, which is a 3D surface, where *XY*-coordinates corresponded to A-scan positions on the area, *Z*-coordinate − pore depth at a given point, was constructed. To reduce the noise, median and Gaussian filters were applied to the depth map.

2.4 Statistical Analysis and Data Processing

The porosity (%) of a depth slice can be calculated as follows:

$$Porosity = 100 * \frac{S_P}{S_T}, \quad (1)$$

where S_P – the total pore area, S_T – the total slice area. For the quantitative description of the depth map, the first- and the second-order statistics were calculated. The following distinctive characteristics of the first-order statistics were used:

$$\text{Mean: } \nu = 2.94 * \sum_{i=0}^{k-1} i * p_i, \quad (2)$$

$$\text{STD: } \sigma = 2.94 * \sqrt{\sum_{i=0}^{k-1} p_i * (i-\nu)^2}, \quad (3)$$

$$\text{Shannon entropy: } H = -\sum_{i=0}^{k-1}(p_i * \log(p_i)), \quad (4)$$

$$\text{Kurtosis: } \gamma_2 = \frac{\mu_4}{\sigma^4} - 3, \quad (5)$$

$$\text{Skew: } A_s = \frac{\mu_3}{\sigma^3}, \quad (6)$$

where ν – the first raw moment of the mean values of pore depth in the studied area, k – the number of values for a single depth map element, p_i – the probability of depth's value equal to $i * 2.94$ μm (i is the number of step along *Z*-coordinate grid), σ – the standard deviation (STD) from the mean value ν, μ_3 – the third central moment, μ_4 – the fourth central moment. The *n*-th order raw moment is following:

$$\nu_n = E[X^n], \quad (7)$$

the *n*-th order central moment is:

$$\mu_n = E[(X - E[X])^n], \quad (8)$$

where E – the mathematical expectation, X – the random value.

The gray-level co-occurrence matrix (GLCM) for every depth map was built to calculate the second order statistics. The GLCM is following:

$$P_{i,j} \equiv P_{\Delta x,\Delta y}(i,j) = \sum_{x=1}^{n}\sum_{y=1}^{m} \begin{cases} 1, & \text{if } I(x,y)=i \text{ and } I(x+\Delta x,y+\Delta y)=j \\ 0, & \text{otherwise} \end{cases}, \quad (9)$$

where P – GLCM with size (k,k), $(\Delta x, \Delta y)$ – offset from the considered pixel, when GLCM constructing, $I(x,y)$ – the value of the *Z*-coordinates corresponding to the boundary between air and metal.

For the second-order statistics, the following parameters were considered:

$$\text{Correlation: } \rho = \sum_{i,j=0}^{k-1} P_{i,j} * \left[\frac{(i-\nu_i)(j-\nu_j)}{\sqrt{\sigma_i^2 \sigma_j^2}}\right], \quad (10)$$

$$\text{Entropy: } H = \sum_{i,j=0}^{k-1} -P_{i,j} * \log(P_{i,j}), \quad (11)$$

$$\text{Contrast: } k = \sum_{i,j=0}^{k-1} P_{i,j} * (i-j)^2, \quad (12)$$

$$\text{Dissimilarity: } D = \sum_{i,j=0}^{k-1} P_{i,j} * |i-j|, \quad (13)$$

$$\text{Homogeneity: } Q = \sum_{i,j=0}^{k-1} \frac{P_{i,j}}{1+(i-j)^2}, \quad (14)$$

$$\text{Angular Second Moment (ASM): } A = \sum_{i,j=0}^{k-1} P_{i,j}^2, \quad (15)$$

$$\text{Energy: } E = \sqrt{ASM}, \quad (16)$$

where $P_{i,j}$ – elements of the GLCM, ν_i and ν_j – mean values of the GLCM elements along i-line and j-row, respectively.

The statistical significance of differences was analyzed using the nonparametric Mann-Whitney test.

3 Results

The examples of photographs from 5 different groups (for 5 different temperatures) of TiNi samples are shown in Fig. 5(a). Each sample was studied according to the OCT protocol presented in the Materials and Methods section. There are two variants of processing C-scans in this analysis. The first one is based on manual selection surface depth. After that, area near surface was used and 95% quantiles were calculated [27] (see examples in Fig. 5(b)). The second one is based on 2D depth map calculation (the examples are shown in Fig. 5(c)).

Demonstration of the porosity distribution by depth constructed for each sample group, using the algorithm described in the Materials and Methods section, is shown in Fig. 6. At depths larger than 800 μm, the porosity is insignificant.

The cumulative sum for this function is the volume of pores, which do not fall within the optical shadow region. The first and the second-order statistics were presented in Fig. 7 and Fig. 8.

The TiNi samples produced at 1230 °C and 1240 °C have less pronounced changes compared to those of 1260 °C and 1270 °C (Fig. 7).

Correlation analysis revealed the relationship between the texture features of OCT images and their potential role in porosity assessment (Fig. 9). A strong negative correlation is observed between homogeneity and GLCM entropy ($r = -0.97$) having the obvious meaning: more homogeneous materials have less texture variability. Contrast and dissimilarity features form a cluster with high mutual correlation ($r > 0.95$) and are negatively related to the entropy ($r \approx -0.75$), confirming their sensitivity to pore boundaries. Energy, ASM parameters demonstrate an almost linear dependence ($r = 0.94$), which indicates the admissibility of excluding duplicate features when building models. Interestingly, GLCM correlation is weakly related to other metrics ($|r| < 0.33$), indicating its unique contribution to the description of textural features. The revealed dependencies are consistent with theoretical expectations: an increase in porosity leads to an increase in contrast and entropy with a decrease in homogeneity, which confirms the adequacy of the selected features for non-destructive testing.

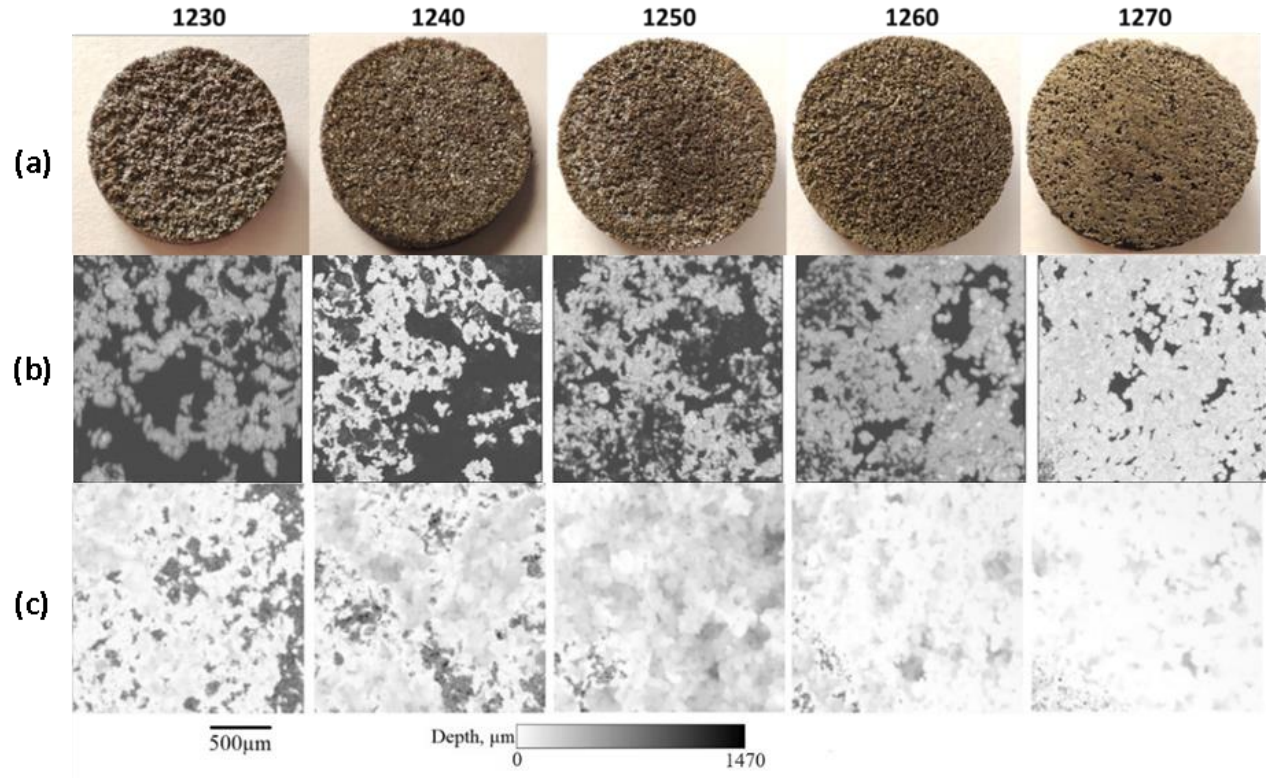

Fig. 5 (a) Photos of the TiNi samples at different temperatures, (b) normalized section of the samples surface, (c) corresponding depth maps.

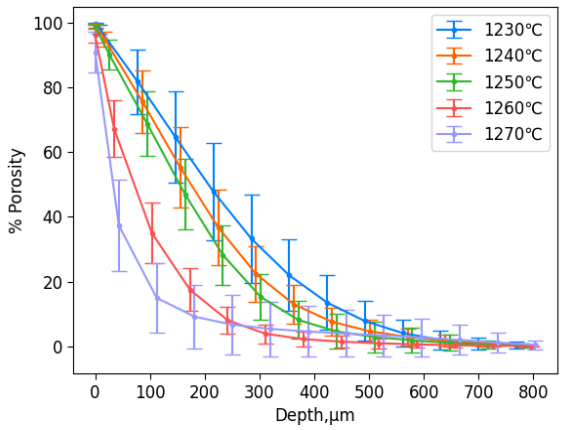

Fig. 6 Dependence of pore area on the depth.

The TiNi sample production temperature values were used to predict the final material properties. The prediction was made based on the first and the second-order statistics calculated for the OCT depth map. Random Forest Regressor (RFR) was selected due to its inherent advantages for our dataset: the relationship between OCT features (e.g., texture metrics, speckle contrast) and porosity is often non-linear, which RFR captures effectively through decision trees. In RFR, the ensemble approach with bootstrapping reduces variance and helps prevent overfitting, critical for our limited sample dataset size. Also, RFR provides native feature importance scores. The training set consisted of 400 depth maps, 80 images from each class. The data were split into training and testing sets in the ratio of 80%/20%. Then, the prediction models were tested using the *K*-fold cross-validation approach. This procedure was repeated 5 times, so that each part of the data from one sample was included in the test set only once. The RFR prediction accuracy is presented in Table 1. The feature vector had a dimensionality of 6 (the first-order statistics), 7 (the second-order statistics), and 13 (both order statistics).

To find informative features, the feature importance, method for RFR from the scikit learn package was used, based on finding a partition of the decision tree with the minimum Gini index. To estimate the mean and variance of informative values, predictive models were trained 10 times. As can be seen from Fig. 10(b), the most informative features are the second-order ones – entropy, energy, ASM. However, the high dispersion index indicates the heterogeneity of the obtained results. In Fig. 10(b), the dispersion values are significantly smaller, indicating greater stability of the results obtained. The average value makes the greatest contribution to the information content. In Fig. 10(c) the results are consistent with Fig. 10(b).

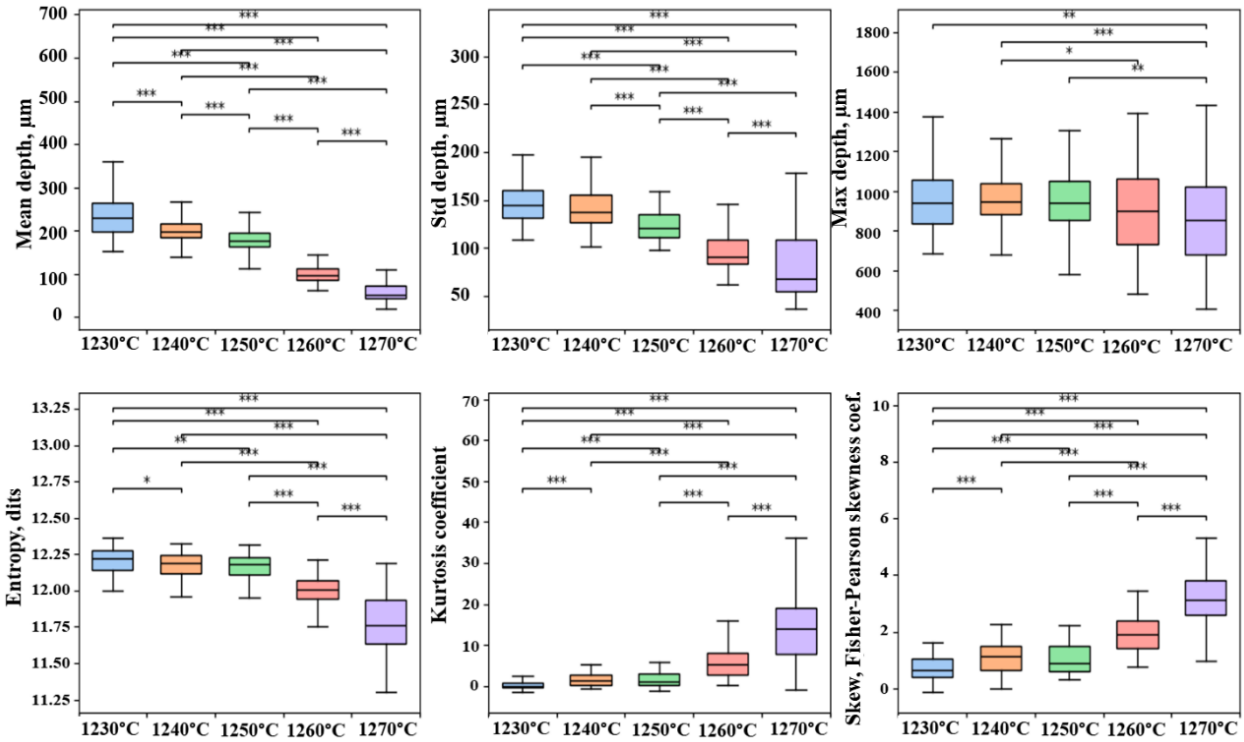

Fig. 7 Distribution of the first order statistics of the depth maps of OCT images. *p<0.05, **p < 0.01, ***p < 0.001 are the significance levels among groups by Mann-Whitney test.

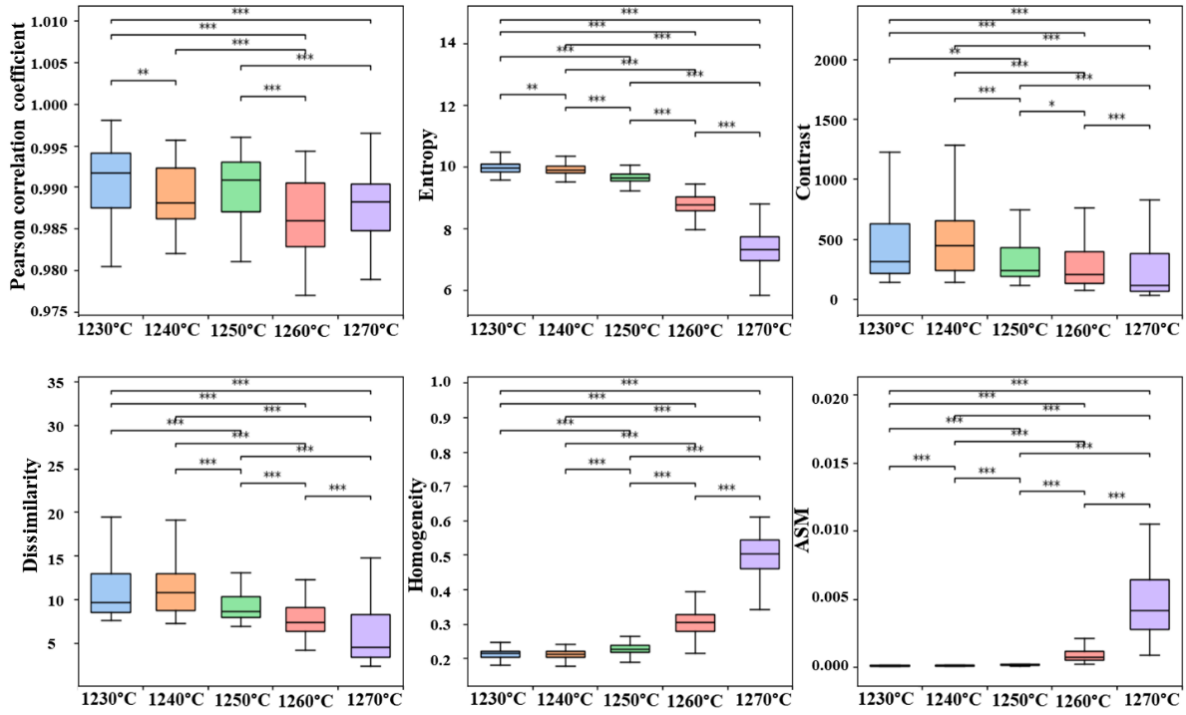

Fig. 8 Distribution of the second order statistics of the depth maps of OCT images. *p<0.05, **p < 0.01, ***p < 0.001 are the significance levels among groups by Mann-Whitney test.

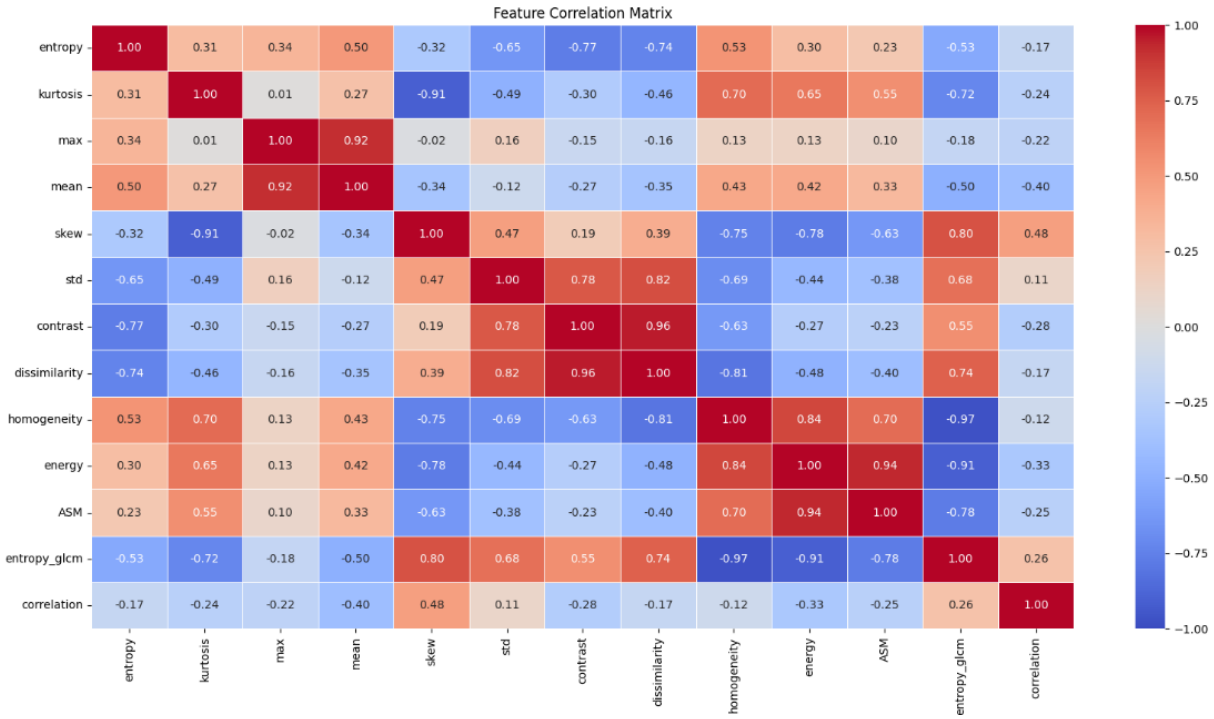

Fig. 9 Correlation matrix for the first and the second order statistics.

Table 1 Accuracy of RFR for the first, the second, and both order statistics.

	First order statistics		**Second order statistics**		**Both**	
	R^2	**MAE (°C)**	R^2	**MAE (°C)**	R^2	**MAE (°C)**
Accuracy (mean ± STD)	0.958 ± 0.046	4.141± 0.651	0.955 ± 0.051	3.671 ± 0.642	0.955 ± 0.052	3.571 ± 0.659

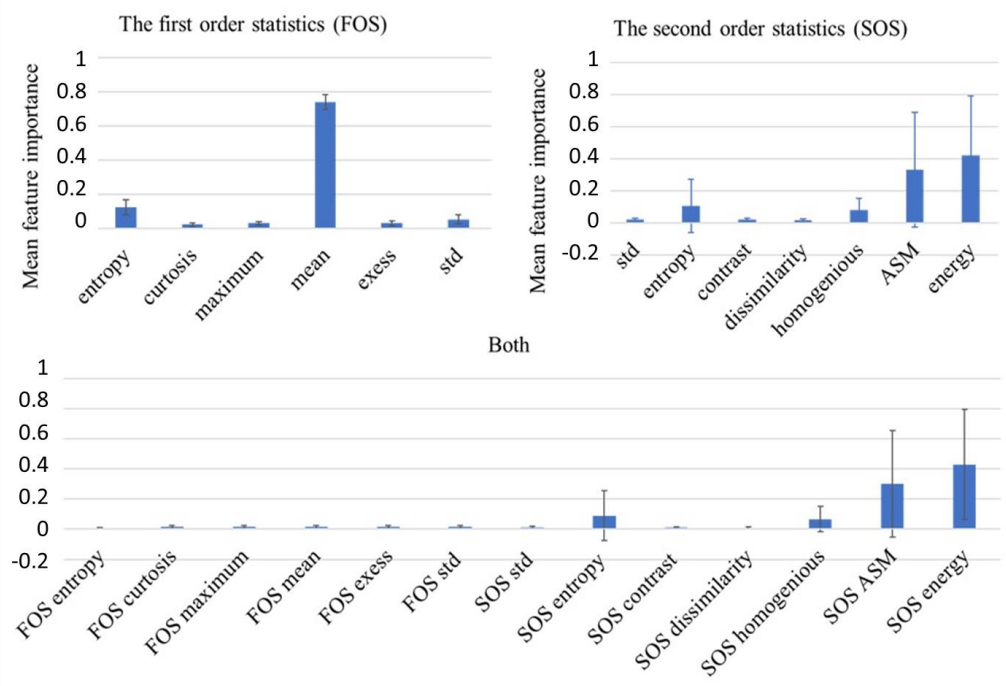

Fig. 10 Feature importance for the first and the second order statistics.

4 Discussion

According to Fig. 7, the mean depth gradually decreases depending on the increase in sintering temperature. Samples with a sintering temperature of 1230 °C have a large average depth, while samples with a sintering temperature of 1270 °C have a minimum average depth. Therefore, it can be assumed that samples with a sintering temperature of 1230 have deeper pores and may be more porous than others. These conclusions can be confirmed by referring to Figs. 5(a) and 5(b), which show that the surface of the sample with a sintering temperature of 1230 °C is more porous than the surface of the sample 1270 °C. It can also be noted that pores maximal depth of all temperature groups is approximately at the same level. However, samples with a sintering temperature of 1270 °C have the lowest maximal depth and statistically significantly differ from almost of other groups. Therefore, by varying the sintering temperature, it is possible to achieve different porosity of the samples, which must be taken into account in manufacturing TiNi implants.

The strengths of the RFR method are the evaluation of complex dependencies (dependence of porosity on sintering temperature, many characteristics required as a result of constructing regression), work on a small amount of data (in our case, 5 groups of 100 images were used), robustness to outliers. Since we propose to describe the depth map with a few key parameters (e.g. average depth, entropy, etc.), RFR data model predicted them better than linear models, which makes it possible to capture complex dependencies without overfitting. RFR offers a compelling trade-off between accuracy and simplicity of sintering temperature-based predictions. While deep learning may outperform it in scenarios with large datasets, the interpretability and low computational cost of RFR makes it well-suited for industrial applications with limited training data. Future work could hybridize RFR with physics-based constraints.

5 Conclusion

The presented results demonstrate that OCT can be used in systems of quality control of porous metal alloy manufacturing. The texture parameters derived from OCT images can be linked to crucial material properties such as porosity, defects (e.g., cracks), and surface or subsurface inhomogeneities. RFR-based approach using OCT depth maps and their the first and the second order statistics was proposed to predict TiNi samples sintering temperature. The RFR model achieves R^2 value of 0.95 for reconstruction of the first- and the second-order OCT image texture metrics. This method provides a robust, interpretable alternative to deep learning approaches for small and medium datasets.

Acknowledgments

The investigation was supported by Russian Science Foundation with the grant № 24-63-00049, https://rscf.ru/en/project/24-63-00049/.

Disclosures

All authors declare that there is no conflict of interest in this paper.

References

1. V. E. Gunter, V. N. Khodorenko, and T. L. Chekalkin, "Medical materials and shape memory implants", Publishing House of MIT, Tomsk (2011). ISBN:9785985890365.
2. J. Zhu, Q. Zeng, and T. Fu, "An updated review on TiNi alloy for biomedical applications," Corrosion Reviews 37(6), 539–552 (2019).
3. W. Cai, Y. F. Zheng, X. Meng, and L. C. Zhao, "Superelasticity in TiNi alloys and its applications in smart systems," Materials Science Forum 475, 1915–1920 (2005).
4. S. H. Mohammed, S. H. Shahatha, "Shape memory alloys, properties and applications: a review," AIP Conference Proceedings, AIP Publishing 2593(1), 020008 (2023).
5. V. Shishkovsky, L. T. Volova, M. V. Kuznetsov, Yu. G. Morozov, and I. P. Parkin, "Porous biocompatible implants and tissue scaffolds synthesized by selective laser sintering from Ti and NiTi," Journal of Materials Chemistry 18(12), 1309–1317 (2008).
6. Z. Wang, Y. Tan, and N. Li, "Powder metallurgy of titanium alloys: a brief review," Journal of Alloys and Compounds 965, 171030 (2023).
7. S. G. Anikeev, N. V. Artyukhova, M. I. Kaftaranova, V. N. Khodorenko, E. V. Yakovlev, A. B. Markov, V. V. Promakhov, and O. R. Mamazakirov, "The influence of electron-beam treatment on the structure of a TiNi powder alloy obtained by calcium-hydride reduction," Journal of Surface Investigation: X-ray, Synchrotron and Neutron Techniques 15, 1067–1071 (2021).
8. N. V. Artyukhova, Yu. F. Yasenchuk, K. Ji-Soon, and V. É. Gunther, "Reaction sintering of porous shape-memory Titanium−Nickelide-based alloys," Russian Physics Journal 57, 1313–1320 (2015).
9. I. A. Drozdov, "Formation of intermetallics in a porous powder Titanium-Nickel diffusion couple," Powder Metallurgy and Metal Ceramics 34(5,6), 62–70 (1995).
10. C. Velmurugan, V. Senthilkumar, and P. S. Kamala, "Microstructure and corrosion behavior of niti shape memory alloys sintered in the SPS process," International Journal of Minerals, Metallurgy, and Materials 26(10), 1311–1321 (2019).
11. T. Miao, S. Zhan, X. Chen, and L. Hu, "Effect of sintering temperature on microstructure characteristics of porous NiTi alloy fabricated via elemental powder sintering," Materials 17(3), 743 (2024).
12. D. Zhao, Y. Yang, J. Liu, G. Yang, Y. Qin, and D. Yin, "Effect of soaking time on the preparation of porous NiTi alloy during fields-activated micro-sintering and forming technology," in 4th International Conference on New Forming Technology (ICNFT 2015), MATEC Web of Conferences 21, 10007 (2015).
13. D. F. Williams, "On the mechanisms of biocompatibility", Biomaterials 29(20), 2941–2953 (2008).
14. N. Viknianshchuk, A. I. Mishanin, S. I. Tverdokhlebov, and A.S. Golovkin, "Approaches to biomaterials testing according to modern biocompatibility paradigm," Translational Medicine 4(1), 29–40 (2017).
15. M. Bahraminasab, B. B. Sahari, "NiTi shape memory alloys, promising materials in orthopedic applications," in Shape Memory Alloys − Processing, Characterization and Applications, F. M. B. Fernandes (Ed.), 262–278 (2013).
16. J. L. Hernandez, K. A. Woodrow, "Medical applications of porous biomaterials: features of porosity and tissue-specific implications for biocompatibility," Advanced Healthcare Materials 11(9), 2102087 (2022).
17. H. J. Haugen, S. Bertoldi, "Characterization of morphology—3D and porous structure," Characterization of Polymeric Biomaterials, 21–53 (2017).
18. Y. Yasenchuk, E. Marchenko, V. Gunther, A. Radkevich, O. Kokorev, S. Gunther, G. Baigonakova, V. Hodorenko, T. Chekalkin, J. Kang, S. Weiss, and A. Obrosov "Biocompatibility and clinical application of porous TiNi alloys made by self-propagating high-temperature synthesis (SHS)," Materials 12(15), 2405 (2019).
19. S. J. Hollister, "Porous scaffold design for tissue engineering," Nature Materials 4(7), 518–524 (2005).
20. F. S. L. Bobbert, A. A. Zadpoor, "Effects of bone substitute architecture and surface properties on cell response, angiogenesis, and structure of new bone," Journal of Materials Chemistry B 5(31), 6175–6192 (2017).
21. C. Torres-Sanchez, F. R. A. Al Mushref, M. Norrito, K. Yendall, Y. Liu, and P. P. Conway, "The effect of pore size and porosity on mechanical properties and biological response of porous titanium scaffolds," Materials Science and Engineering: C 77, 219–228 (2017).
22. Y. Zhang, N. Sun, M. Zhu, Q. Qiu, P. Zhao, C. Zheng, Q. Bai, Q. Zeng, and T. Lu, "The contribution of pore size and porosity of 3D printed porous titanium scaffolds to osteogenesis," Biomaterials Advances 133, 112651 (2022).
23. Q. S. Yan, "Prediction of porosity of porous NiTi alloy from processing parameters based on SVR," Advanced Materials Research 393, 231–235 (2012).
24. V. Maitra, J. Shi, and C. Lu, "Robust prediction and validation of as-built density of Ti-6Al-4V parts manufactured via selective laser melting using a machine learning approach," Journal of Manufacturing Processes 78, 183–201 (2022).
25. T. Kamal, A. Upadhyaya, and Gouthama, "Machine learning based sintered density prediction of bronze processed by powder metallurgy route," Metals and Materials International 29(6), 1761–1774 (2023).
26. L. Mosser, O. Dubrule, and M. J. Blunt, "Reconstruction of three-dimensional porous media using generative adversarial neural networks," Physical Review E 96(4), 043309 (2017).

27. V. V. Nikolaev, T. B. Lepekhina, G. V. Malkin, A. S. Garin, E. S. Marchenko, A. V. Dubrov, M. D. Khomenko, and Y. Kistenev, "Estimating the porosity of Nickel-Titanium (NiTi) implants using optical coherence tomography and machine learning", Journal of Biomedical Photonics & Engineering 10(4), 112–120 (2024).

Thermomechanical Threshold of Laser Action on the Tympanic Membrane while Maintaining Its Structure

Olga I. Baum[1*], Ekaterina M. Kasianenko[1], Anna V. Zolotova[1,2], Mikhail V. Svistushkin[1,2], and Natalia B. Serejnikova[3]

[1] National Research Centre "Kurchatov Institute", 1 Kurchatov sq., Moscow 123182, Russian Federation
[2] Department of Ear, Nose and Throat Diseases, Federal State Autonomous Educational Institution of Higher Education I.M. Sechenov First Moscow State Medical University of the Ministry of Health of the Russian Federation (Sechenov University), 8 Trubetskaya str., Moscow 119048, Russian Federation
[3] Institute for Regenerative Medicine, Federal State Autonomous Educational Institution of Higher Education I.M. Sechenov First Moscow State Medical University of the Ministry of Health of the Russian Federation (Sechenov University), 8 Trubetskaya str., Moscow 119048, Russian Federation
*e-mail: baumolga@gmail.com

Abstract. Laser-induced modification of the structure and properties of biological tissues is a novel and rapidly advancing approach used for tissue reconstruction without causing destruction or coagulation of the biological material. This work is devoted to determining the threshold values of laser exposure parameters on the tissue of the tympanic membrane (TM) while preserving its integrity and structure. The findings aim to facilitate the extrapolation of principles from established laser-based technologies to new biological tissue types, notably those where cells exist predominantly in a state of normoxia. This work is the first step in the development of a new laser technology − laser regeneration of the TM. In this work, using computer modeling, temperature fields and thermal stress fields, the values of which are close to known values, which have a positive effect on cell proliferation and matrix synthesis, were found. Two laser modes selected for the *in vivo* experiment made it possible to determine the acceptable range of effects on the TM under conditions of maintaining its integrity and to find the threshold for detachment of the TM epithelium while maintaining the structure of its deeper layers.

Keywords: infrared laser; temperature field; thermomechanical stress; tympanic membrane.

Paper #9350 received 1 Sep 2025; revised manuscript received 21 Sep 2025; accepted for publication 22 Sep 2025; published online 2 Oct 2025. doi: 10.18287/JBPE25.11.030306.

1 Introduction

Laser-induced modification of the structure and properties of biological tissues is a novel and rapidly advancing approach used for tissue reconstruction without causing destruction or coagulation of the biological material. The primary indicator of treatment efficacy is the preservation of the tissue's functional characteristics. Prominent examples of such technologies include the method for laser treatment of laryngeal stenosis, which has been developed and successfully implemented into clinical practice [1−3], as well as a technique for laser-based regeneration of joint cartilage [4−10], the efficacy of which has been corroborated by cellular studies [2, 11−13]. This study focuses on identifying the threshold parameters of laser exposure on tympanic membrane (TM) tissue, ensuring the preservation of its structural integrity. The results are intended to support the translation of established laser-based methodologies to novel biological tissues, particularly those in which cells predominantly exist under normoxic conditions.

TM perforation remains a common clinical problem worldwide. Perforations can be classified as acute or chronic. While acute TM perforations typically demonstrate a tendency toward spontaneous closure within 7–10 days, the presence of a chronic defect predisposes patients to middle ear infections and may result in significant hearing impairment. This, in turn,

compromises the patients' quality of life, restricts their ability to communicate and exchange information, and reduces their social activity [14−15].

Currently, alternative methods for closing TM perforations are emerging to replace traditional surgical approaches, such as tympanoplasty and myringoplasty. These include the use of various scaffolds, growth factors, and stem cells. The most common treatment strategies involve a combination of these tissue-engineered materials [16−20].

Currently, laser therapy for tympanic membrane perforation is used only as an adjunctive surgical tool. Studies show that CO_2 lasers can be used for precise de-epithelialization of the perforation edges, facilitating subsequent closure of the lesion. Wani et al. (2021) compared the results of CO_2 laser myringoplasty with traditional tympanoplasty and demonstrated perforation closure in 80% of cases, which is slightly lower than with standard surgery (90–94%). However, the laser minimized the impact on surrounding tissue [21].

Combining laser treatment with biomaterials also demonstrates high efficacy. Kuroda et al. (2024) used the OtoLAM CO_2 laser to prepare perforation margins, followed by application of a two-layer collagen sponge (Terudermis). In this study, the overall perforation closure rate was 69.7%, with the highest success rate observed in traumatic injuries (84.6%) [22].

One of the important findings is the identification of latent epithelial stem or progenitor cells within the TM [23−25]. It has been suggested that their activation contributes to the regeneration of the damaged TM. We hypothesize that laser irradiation may serve as a stimulatory factor for initiating regenerative processes of TM perforation. In the literature, there is a study in which TM tissues with post-traumatic perforations were irradiated using lasers with wavelengths of 630 nm and 860 nm. These processes resulted in the restoration of the TM with adequate proliferation of connective tissue and without excessive formation of fibrous tissue, in contrast to the control group (where laser treatment was not applied) [26].

It has been experimentally demonstrated that low-intensity laser irradiation is an effective tool in regenerative medicine for inducing proliferative and differentiation processes in mesenchymal stromal cells (such as osteoblasts, chondrocytes, and fibroblasts) and progenitor cells [27].

Laser irradiation exerts a complex effect on biological tissues, manifesting not only at the cellular and molecular levels but also at the organ level, where it promotes the normalization of metabolic processes and improves microcirculation. In this context, regeneration is considered as a natural response of living tissue to damage. However, the intensity of reparative processes, their dynamics, and the characteristics of the newly formed tissue are directly dependent on the parameters of the external stimulus [10, 28].

Cells of the organism exhibit high sensitivity to changes in the microenvironment, including temperature fluctuations and mechanical stresses. Laser irradiation, modulated in time and space, is capable of generating pulsed-periodic tissue heating, which induces locally heterogeneous thermal expansion and generates pulsating fields of mechanical stress. These controlled factors create specific conditions for cells, enhancing their proliferative activity and stimulating their biosynthetic functions. Consequently, laser exposure can be considered as a tool for the targeted activation of tissue healing and regeneration processes [2].

Modern studies show that medium-intensity laser radiation can have a combined effect on mesenchymal stem cells (MSCs), combining photobiomodulatory and thermal effects. A number of studies have demonstrated that such a combination has a pronounced stimulating effect on the proliferation and colony-forming activity of MSCs. In particular, it was shown that the fragmental (fractional) thermal effect of laser radiation with a wavelength of $\lambda = 1.56$ μm on the BM of rats *in vivo* makes it possible to increase the content of MSCs by two times [29], and when using a wavelength of 980 nm with simultaneous exposure to light and heat, the number of colonies increases several times compared to the control and more than 3 times compared to isolated thermal exposure [30, 31].

An important tool in this field is computer modeling, which allows for the establishment of therapeutic ranges of radiation parameters. Within these ranges, the desired biological response is achieved while avoiding undesirable side effects. Such models are actively used in research, particularly on hard-to-access biological tissues, thereby reducing the scope of *ex vivo* and *in vivo* experiments [8, 32]

Thus, the objective of this study was first to theoretically determine the range, and subsequently, under *in vivo* experimental conditions, to establish the threshold values of laser exposure parameters on the TM tissue while preserving its integrity and structure, followed by histological confirmation.

2 Materials and Methods

2.1 Theoretical Modeling

The theoretical model is based on the heat conduction equation with a volumetric heat source $G(x,y,z,\tau)$, generated by laser radiation and attenuating with depth according to the Bouguer-Lambert-Beer law with an effective absorption coefficient κ

$$\frac{\partial T(x,y,z,\tau)}{\partial \tau} = a\Delta T(x,y,z,\tau) + G(x,y,z,\tau), \quad (1)$$

where a is the thermal diffusivity coefficient. The density of the incident energy flux on the cross-sectional surface of the cartilaginous tissue exhibits a spatial distribution corresponding to a Gaussian profile, with an effective beam radius $r_0(x)$, that accounts for beam divergence in the transverse direction as it propagates through the media along the x-axis.

$$G(x,y,z,\tau)=P(\tau)\exp\left(-\frac{y^2+z^2}{r_0^2(x)}\right)\frac{\kappa\exp(-\kappa x)}{c\rho}, \quad (2)$$

where $P(\tau)$ denotes the time-dependent laser power, c – the specific heat capacity, ρ – the density. At the interfaces between different media, the boundary condition of constant heat flux density was applied. Temperature gradients give rise to thermoelastic stresses, which can be derived for each temperature profile.

For theoretical consideration, pulse-periodic modes with a pulse duration of 100 ms and a repetition duration of 1 Hz were selected. Dynamics of the maximum temperature on the front and back surfaces of samples with a thickness of 100, 150 and 200 μm were constructed. The irradiation power was from 0.1 to 0.7 W. The data for cartilage were chosen as constants describing the model biological environment, since thin autologous cartilage (100–200 μm) is, in terms of its comparative properties, an acoustically and mechanically adequate model of the native tympanic membrane (TM) [33–36].

Experimental studies [33, 34] and numerical modeling [35] confirm that grafts of this thickness do not have a significant effect on the transfer function and vibrational characteristics of the TM. Clinical data [36] demonstrate their effectiveness in tympanoplasty, providing biomechanical stability without compromising acoustic response. Thus, thin cartilage is justifiably used as an in vitro model for studying the biophysics of TM and testing reconstructive techniques.

In numerical modeling, for the moments of achievement the maximum temperature at the first and last pulses in the series of irradiation, temperature profiles were constructed on the front surface, which were then approximated by Gaussian axially symmetric functions $T(r)$, which led to the discovery of the components of the thermal stress tensor. Solving the thermoelastic problem under this irradiation geometry enables determination of the radial and angular components of the thermoelastic stress tensor, expressed as follows:

$$\sigma_r=\alpha E\left(\frac{1}{b^2}\int_0^b T(r)rdr-\frac{1}{r^2}\int_0^r T(r)rdr\right);$$
$$\sigma_\theta=\alpha E\left(-T(r)+\frac{1}{b^2}\int_0^b T(r)rdr+\frac{1}{r^2}\int_0^r T(r)rdr\right), \quad (3)$$

where b denotes the boundary of the integration domain with respect to the radial coordinate, α – the coefficient of thermal expansion, E – the elastic modulus, $T(r)$ – represents the Gaussian distribution of the temperature profile.

Using Eq. (3), the region of maximum deformations, determined by the difference between the angular and radial components, the maximum value of which has a decisive influence on the cell and its environment, have been calculated.

2.2 In vivo Experiment on Small Laboratory Animals

An experimental study was conducted on laser exposure at a wavelength of 1.56 μm with various power and time parameters on small laboratory animals, approved by the local ethics committee (protocol No. 10−24 dated 04/18/2024).

According to the literature, the chinchilla is an optimal experimental model for the middle ear. Rats and guinea pigs have a small diameter of the external auditory canal, which significantly complicates simultaneous manipulation with endoscope and instruments, or work under a microscope using two instruments [37]. The diameter of the external auditory canal chinchilla is enough for manipulations on the TM using a 4 mm rigid endoscope, which significantly improves the view compared to using microscopic equipment. The diameter of the TM of chinchilla is 7–10 mm. The structure of the TM and auditory ossicles is similar to humans [38–40]. Thus, adult male chinchillas weighing 500–700 g, aged 6 months, were chosen as an experimental model. Males were used due to the lower hormonal variability of males.

All manipulations were performed in a vivarium complex. Before anesthesia, the animals were fasted for 12 h. Then, the chinchillas of both groups were given general anesthesia by intramuscular administration of a solution of Zoletil at a dose of 10 mg/kg and Xylazine (dose 0.15 ml/kg), which corresponds to the minimum dosages used for short-term painful procedures. Before the administration of the drugs, a solution of Atropine sulfate (at a dose of 0.05 mg/kg of animal weight) was administered subcutaneously as premedication 15 min before.

After the animal was anesthetized, using a 0-degree rigid endoscope (Karl Storz, Germany) connected to the video camera console controller (Karl Storz), the TM was examined for its integrity and the absence of inflammation (Fig. 1, Fig. 2).

Fig. 1 Endoscopic examination of the TM.

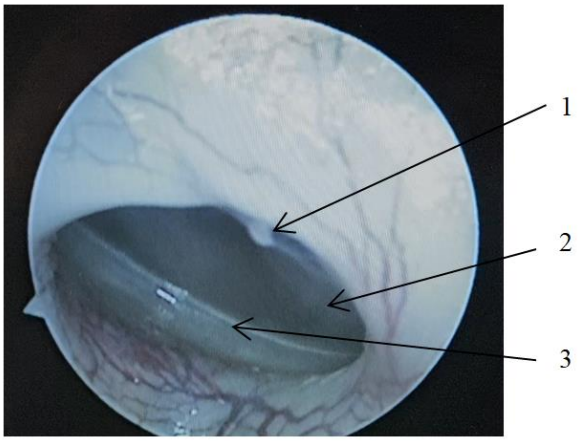

Fig. 2 Chinchilla's tympanic membrane viewed with an endoscope: 1 – umbo, 2 – anteroinferior quadrant of the tympanic membrane of the chinchilla, 3 – annulus tympanicus.

The next step was TM exposition to laser radiation (wavelength of 1.56 μm) using a 600 μm diameter fiber optic in the area of the annulus tympanicus and the umbo (Fig. 3). According to the literature, progenitor cells were found in the indicated areas, forming the TM's own regenerative potential [23–25]. Laser radiation was applied perpendicular to the surface of the tympanic membrane, at a distance of 1 mm from it.

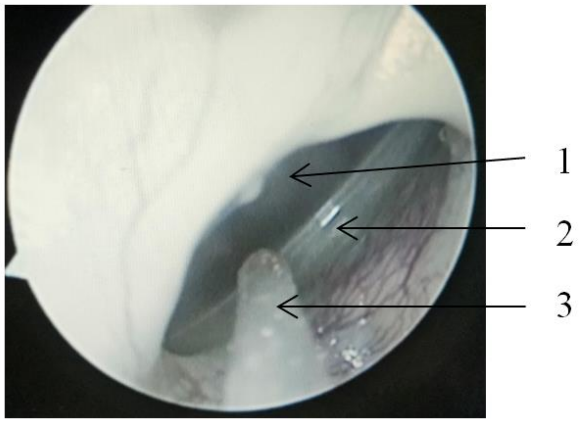

Fig. 3 The laser fiber is guided to the annulus tympanicus of the tympanic membrane: 1 – tympanic membrane, 2 – annulus tympanicus, 3 – optical fiber that delivers laser radiation.

Six animals were divided into 2 groups:

• group 1–3 chinchillas (6 ears), whose TM's were exposed to a laser with a wavelength of 1.56 μm and a power of 0.5 W, with pulses of 100 ms for a total duration of 15 s, power density 56 W/cm² (laser mode №1);

• group 2–3 chinchillas (6 ears), whose TM's were exposed to a laser with a wavelength of 1.56 μm and a power of 0.3 W, with pulses of 100 ms for a total duration of 30 s, power density 100 W/cm² (laser mode №2).

2.3 Control Otoendoscopy

After irradiation of the specified areas of the TM, control otoendoscopy was performed using an endoscope (Karl Storz, Germany).

After that all animals were then removed from the experiment.

Euthanasia was performed using an overdose of anesthetics, which, in accordance with the European Directive 2010/63/EU on the protection of animals used for scientific purposes, is included in the list of applicable methods of euthanasia for rodents. The use of injectable drugs is the fastest, most reliable and optimal method of euthanasia, as it does not cause pain or fear of the animal [41]. Material was taken only after confirmation of the animal's death (absence of pulse, breathing, absence of corneal reflex, inability to hear breathing and heartbeat using a phonendoscope).

2.4 Histological Examination

After the animal was removed from the experiment, the TM preparation was instrumentally isolated under the control of a Carl Zeiss microscope. The obtained samples were fixed in neutral formalin, decalcified in a Biodec R solution, embedded in paraffin, serial sections 4 μm thick were obtained every 50 μm, and stained with hematoxylin and eosin. The samples were studied using standard light microscopy and phase-contrast microscopy in a Leica DM 4000 B LED microscope (Leica Camera AG, Germany) with a Leica DFC 7000 T camera (Leica Camera AG, Germany).

3 Results and Discussion

Using a theoretical model in a numerical experiment for the time of reaching the maximum temperature on the first and last pulses in irradiation series differing in power and total duration, temperature profiles were constructed on the front surface of the irradiation, which were then approximated by Gaussian axisymmetric functions of the form $T(r)$, which made it possible to find the components of the thermal stress tensor. Using Eq. (3), the region of maximum thermal stresses was calculated, determined by the difference between the angular and radial components, the maximum value of which has a decisive influence on the cells and their environment.

Figure 4 shows the theoretical dynamics of the maximum temperature on the front surface of the samples in two modes selected for further *in vivo* experiments. Laser mode No. 1: power 0.5 W, total irradiation duration 15 s; laser mode No. 2: power 0.3 W, total irradiation duration 30 s.

It is shown that the temperature on the back surface of a 100 μm thick sample is lower than the temperature on the front surface by approximately 3%, and for a 200 μm thick sample by 6%. Thermal stresses were calculated for the front surface of the samples – from the side of incident radiation (Fig. 5).

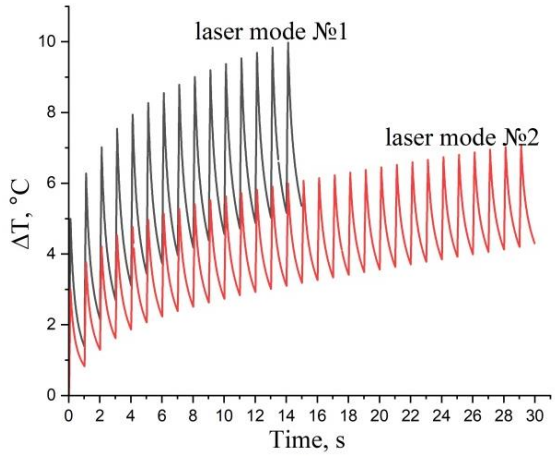

Fig. 4 Theoretical dynamics of change in maximum temperature during irradiation in two laser modes.

The approximation of the temperature profiles was substituted into the equation for the components of the thermal stress tensor and the values of the maximum thermal stresses at the moment of reaching the maximum temperature at the end of the first and last pulses with a duration of 100 ms for the two selected modes were found. Their profiles are shown in Fig. 6. With a power difference of 1.7 times and an irradiation duration of 2 times, the temperature maxima on the first and last irradiation pulses for a more powerful mode differed by 2 times, and for a more gentle one by 2.3 times. At the same time, the corresponding difference in the maximum values of thermal stresses was 1.5 and 1.47 times, which indicates that the dynamics of thermal stresses depend not so much on the absolute values of the temperatures achieved, but on the dynamics of the temperature field propagation.

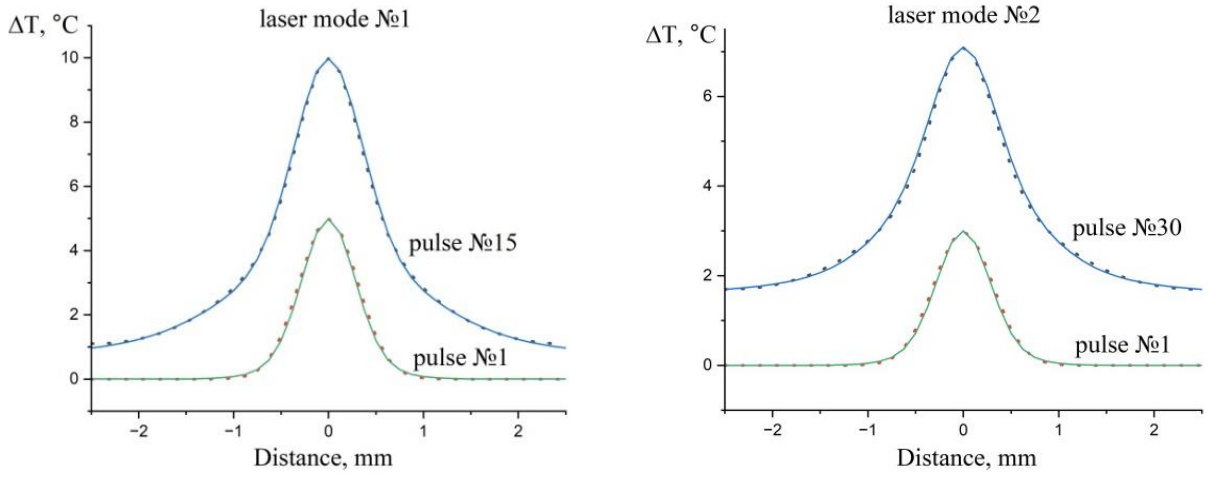

(a) (b)

Fig. 5 Theoretical temperature profiles in a direction perpendicular to the propagation of the light beam (points) and their approximation (lines) for two laser modes at the first and last pulses for two modes: (a) laser mode №1, (b) laser mode №2.

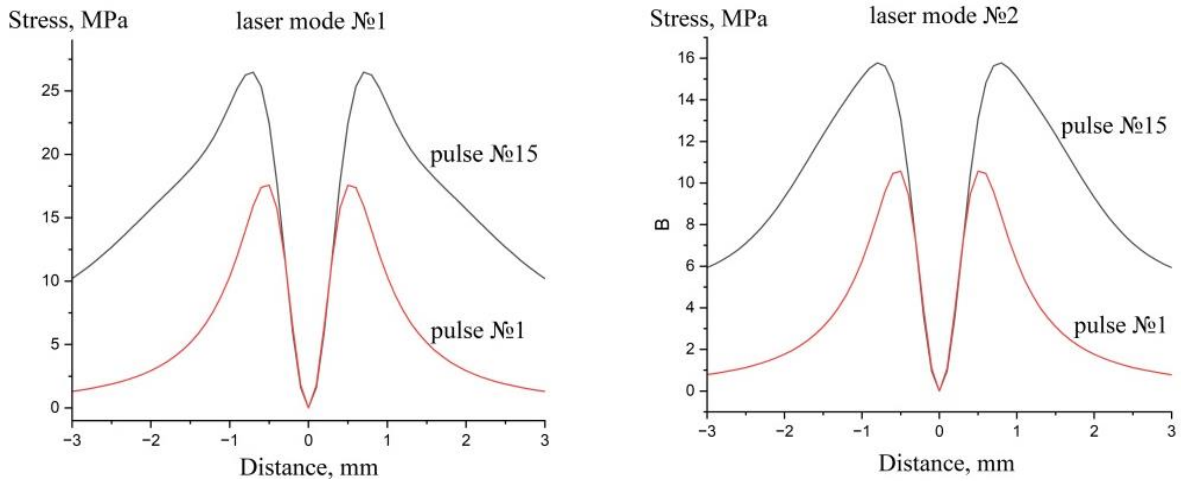

(a) (b)

Fig. 6 Thermal stress for two modes at the first and last pulse of the series: (a) laser mode №1, (b) laser mode №2.

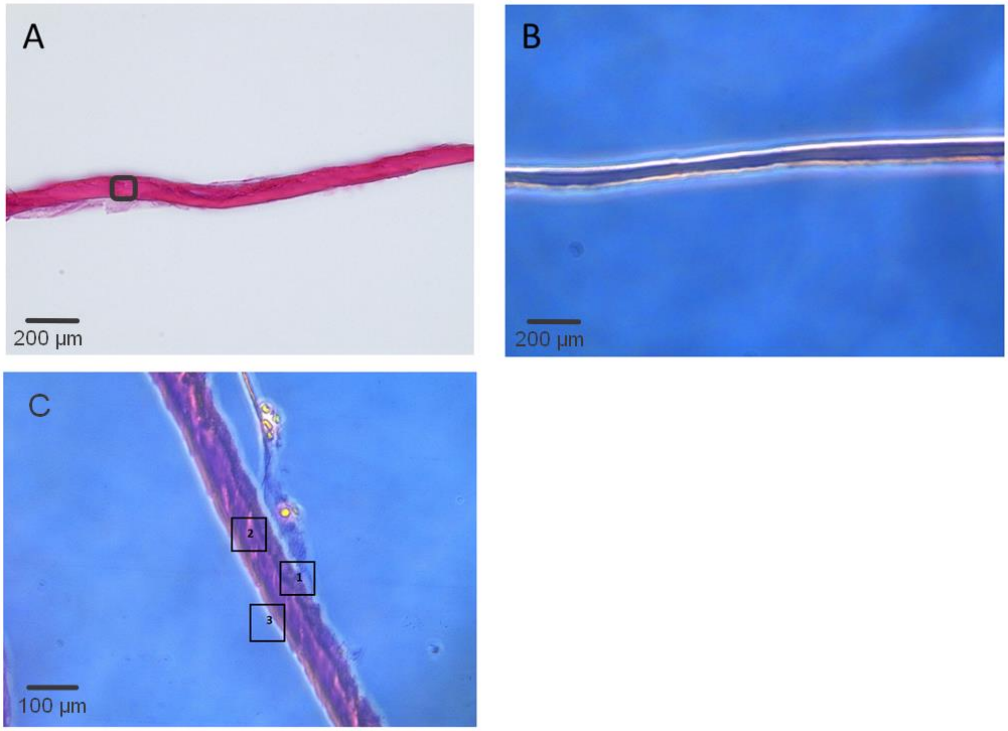

Fig. 7 Tympanic membrane, normal. (A) Hematoxylin and eosin staining. Magnification ×400. (B) Phase-contrast microscopy. Magnification ×400. (C) Phase contrast microscopy (magnification ×630): 1 − external layer (stratified squamous epithelium); 2 – fibrous layer (fibrous connective tissue); 3 − mucous layer (simple epithelium).

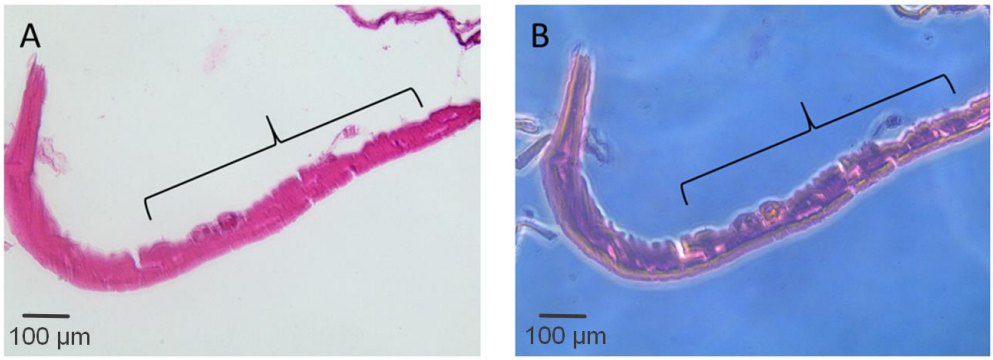

Fig. 8. Tympanic membrane, irradiated area of group 1. Magnification ×630. (A) Hematoxylin and eosin. (B) Phase-contrast microscopy. The curly bracket indicates the laser exposure zone.

The region of maximum thermal stresses has a ring shape and is located on the periphery of the laser spot, moving away from the axis of laser action with each subsequent pulse. Using numerical modeling, two laser action modes were selected from the studied range of modes, in which the values of thermal stresses are close to the values that have a positive effect on cell proliferation and matrix synthesis [2].

Both modes presented above were selected for further *in vivo* experiments, and the irradiation geometry was also selected based on the calculations performed. Thus, in the subsequent *in vivo* experiment, laser radiation was delivered to the target area using quartz optical fiber with a core diameter of 600 μm. The fiber optic tip was positioned in close proximity to the surface of the TM, but excluding physical contact with the tissue. The power density in the treatment zone varied in the range from 56 to 100 W/cm². This power density was chosen taking into account the angular location of the TM inside the chinchilla's ear canal and the impossibility of perpendicularly feeding the optical fiber to the TM surface.

After laser irradiation, control otoendoscopy did not reveal any damage to the TM tissues in any case. During the histological examination, the first stage was to study the areas of the TM outside the irradiation zone. The tissue of the chinchilla TM outside the irradiation points has a normal structure: a layer of multilayer squamous epithelium, a layer of loose fibrous connective tissue, a layer of simple epithelium (Fig. 7). The three-layer structure of the TM is especially clearly visible with phase-contrast microscopy (Fig. 7C).

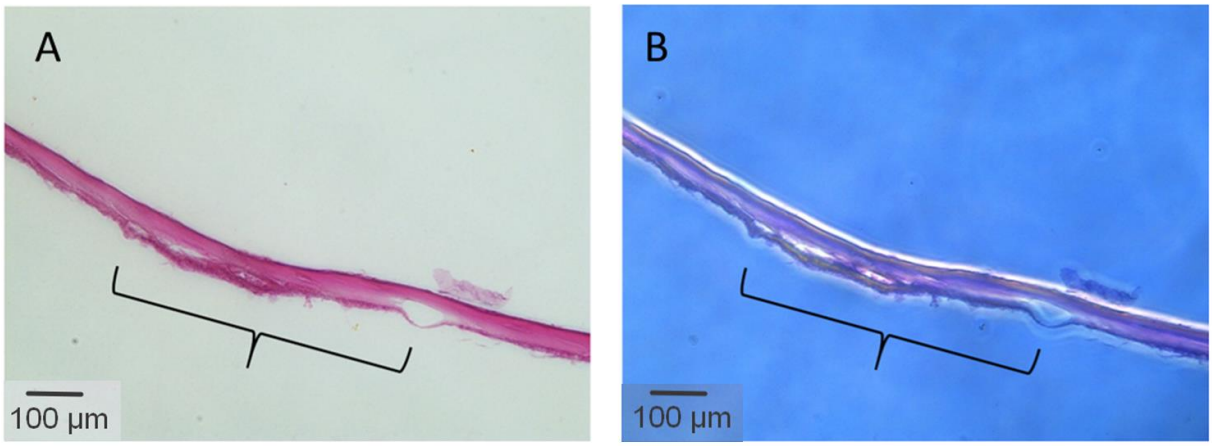

Fig. 9 Tympanic membrane, irradiated area of group 2. (×630). (A) Hematoxylin and eosin. (B) Phase-contrast microscopy. The curly bracket indicates the area of exfoliating epithelium.

The second stage involved studying the irradiated areas of the TM tissue in groups 1 and 2. In group 1 (laser mode №1), the irradiated areas had a foamy structure and were vacuolated, which may indicate the initial stage of laser vaporization (Fig. 8), in which the stratified squamous epithelium is damaged (coagulation necrosis).

In group 2 (laser mode №2), a zone of peeling epithelium is visible in the irradiated areas, which at the same time retains its normal structure (Fig. 9).

4 Conclusions

Based on the theoretical model presented in the work, the dynamics and profiles of the temperature field on the front surface of the irradiated sample and the corresponding profiles of the thermal stress field were constructed. Accordingly, for the moment of reaching the maximum temperature at the end of each pulse with a duration of 100 ms, the thermal stress fields also reach a maximum. The area of maximum thermal stresses has a ring shape and is located on the periphery of the laser spot, moving away from the axis of laser action with each subsequent pulse. Using computer modeling, laser action modes were found in which the values of thermal stresses are close to the values that have a positive effect on cell proliferation and matrix synthesis [2].

Two modes selected for the *in vivo* experiment and differing from each other in power by about 1.7 times and in the total duration of irradiation by 2 times, made it possible to determine the acceptable range of action on the BP under conditions of maintaining its integrity and to find the threshold for detachment of the BP epithelium while maintaining the structure of its deeper layers.

Acknowledgements

The study was supported by the Russian Science Foundation, grant No. 25-15-00341.

Disclosures

All authors declare that there is no conflict of interest in this paper.

References

1. V. M. Svistushkin, S. V. Starostina, L. V. Selezneva, O. I. Baum, E. N. Sobol, Yu. M. Alexandrovskaya, and A. V. Starostin, "The use of modified autografts for plastic closure of laryngotracheal defects: An experimental study," Farmateka 27(5), 72–76 (2020).
2. Yu. M. Alexandrovskaya, O. I. Baum, A. B. Shekhter, E. V. Petersen, O. A. Tiflova, A. K. Dmitriev, V. A. Ulyanov, V. M. Svistushkin, L. V. Selezneva, and E. N. Sobol, "Mechanisms of laser activation of chondrocytes in osteoarthritis healing," Laser Physics Letters 15(8), 085601 (2018).
3. O. I. Baum, Y. M. Soshnikova, E. N. Sobol, A. Ya. Korneychuk, M. V. Obrezkova, V. M. Svistushkin, O. K. Timofeeva, and V. V. Lunin, "Laser reshaping of costal cartilage for transplantation," Lasers in Surgery and Medicine 43(6), 511–515 (2011).
4. Yu. M. Alexandrovskaya, O. I. Baum, A. A. Sovetsky, A. L. Matveyev, L. A. Matveev, E. N. Sobol, and V. Y. Zaitsev, "Spatially-resolved slow dynamics of strains due to residual stresses in cartilaginous implants visualized by phase-sensitive optical coherence tomography," Proceedings of SPIE 11641, 116410S (2021).
5. E. M. Kasyanenko, A. I. Omelchenko, and O. I. Baum, "Deformation response of biological phantoms and cartilage tissue under laser irradiation," Optics and Spectroscopy 131, 1000–1005 (2023).

6. Y. M. Alexandrovskaya, O. I. Baum, A. V. Yuzhakov, V. M. Svistushkin, A. V. Buzmakov, Y. S. Krivonosov, B. S. Roshchin, and D. A. Zolotov, "Infrared laser effect on healthy and ossified costal cartilage: The development of stable load-bearing autoimplants," Lasers in Surgery and Medicine 53(2), 275–283 (2021).
7. V. Y. Zaitsev, A. L. Matveyev, L. A. Matveev, G. V. Gelikonov, D. V. Shabanov, A. A. Sovetsky, A. I. Omelchenko, O. I. Baum, and A. Vitkin, "Optical coherence elastography assesses tissue modifications in laser reshaping of cornea and cartilages," Proceedings of SPIE 10496, 104960G (2018).
8. E. Sobol, O. Baum, A. Shekhter, A. Guller, and A. Baskov, "Laser-induced micropore formation and modification of cartilage structure in osteoarthritis healing," Journal of Biomedical Optics 22(9), 091515 (2017).
9. O. I. Baum, Yu. M. Soshnikova, A. I. Omelchenko, and E. N. Sobol, "Nanoparticles for diagnostics and laser medical treatment of cartilage in orthopaedics," Proceedings of SPIE 8595, 85951K (2013).
10. E. Sobol, A. Shekhter, A. Guller, O. Baum, and A. Baskov, "Laser-induced regeneration of cartilage," Journal of Biomedical Optics 16(8), 080902 (2011).
11. C. R. Tim, C. C. S. Martignago, L. Assis, L. M. Neves, A. L. Andrade, N. C. Silva, N. Parizotto, K. Z. Pinto, and A. C. Rennó, "Effects of photobiomodulation therapy in chondrocyte response by in vitro experiments and experimental model of osteoarthritis in the knee of rats," Lasers in Medical Science 37(3), 1677–1686 (2022).
12. Yu. M. Soshnikova, O. I. Baum, E. M. Shcherbakov, A. I. Omelchenko, A. B. Shekhter, V. V. Lunin, and E. N. Sobol, "Laser radiation effect on chondrocytes and intercellular matrix of costal and articular cartilage impregnated with magnetite nanoparticles," Lasers in Surgery and Medicine 47(3), 243–251 (2015).
13. E. Sobol, N. Vorobieva, O. Baum, A. Shekhter, and A. Guller, "Is it possible to perform laser reshaping without dramatic effect on chondrocytes," Lasers in Surgery and Medicine 43(S23), 911 (2011).
14. Z. Hussain, R. Pei, "Necessities, opportunities, and challenges for tympanic membrane perforation scaffolding-based bioengineering," Biomedical Materials 16(3), 032001 (2021).
15. S. Kanemaru, H. Umeda, Y. Kitani, T. Nakamura, S. Hirano, and J. Ito, "Regenerative treatment for tympanic membrane perforation," Otology & Neurotology 32(8), 1218–1223 (2011).
16. X. Zhao, J. Zhang, P. Tian, and X. Cui, "The latest progress of tympanic membrane repair materials," American Journal of Otolaryngology 43(5), 103408 (2022).
17. M. Aleemardani, Z. Bagher, M. Farhadi, H. Chahsetareh, R. Najafi, B. Eftekhari, and A. Seifalian, "Can tissue engineering bring hope to the development of human tympanic membrane?," Tissue Engineering Part B: Reviews 27(6), 572–589 (2021).
18. R. Kaboodkhani, D. Mehrabani, A. Moghaddam, I. Salahshoori, and H. A. Khonakdar, "Tissue engineering in otology: a review of achievements," Journal of Biomaterials Science 35(7), 1105–1153 (2024).
19. E E. A. Harvey, W. Hong, E. J. Sheehy, R. J. do Amaral, P. Khampang, C. L. Runge, C. O'Leary, F. J. O'Brien, and J. E. Kerschner, "Chronic tympanic membrane perforation repair with a collagen-based scaffold: An *in vivo* model," International Journal of Pediatric Otorhinolaryngology 176, 111807 (2024).
20. R. Najafi, F. Yazdian, M. Pezeshki-Modaress, M. Aleemardani, H. Chahsetareh, S. Hassanzadeh, M. Farhadi, and Z. Bagher, "Fabrication and optimization of multilayered composite scaffold made of sulfated alginate-based nanofiber/decellularized Wharton's jelly ECM for tympanic membrane tissue engineering," International Journal of Biological Macromolecules 253, 127128 (2023).
21. I. Singh, B. S. Patil, and M. Z. Akhtar, "A study to compare the outcomes of CO2 laser assisted myringoplasty versus conventional type1 tympanoplasty in small central tympanic perforations," International Journal of Otorhinolaryngology and Head and Neck Surgery 7(5), 809–814 (2021).
22. K. Kuroda, N. Kuroda, "Statistical evaluation of 231 ears that received tympanic membrane perforation closure using OtoLAM and Terudermis," International Journal of Practical Otolaryngology 07(01), e1–e8 (2024).
23. S. W. Kim, J. Kim, H. Seonwoo, K. J. Jang, Y. J. Kim, H. J. Lim, K. T. Lim, C. Tian, J. H. Chung, and Y. H. Choung, "Latent progenitor cells as potential regulators for tympanic membrane regeneration," Scientific Reports 5, 11542 (2015).
24. L. J. Liew, A. Y. Wang, and R. J. Dilley, "Isolation of epidermal progenitor cells from rat tympanic membrane," in Progenitor Cells. Methods in Molecular Biology, M. V. Joglekar, A. A. Hardikar (Eds.), Springer New York, 247–255 (2019).
25. J. Knutsson, M. von Unge, and H. Rask-Andersen, "Localization of progenitor/stem cells in the human tympanic membrane," Audiology and Neurotology 16(4), 263–269 (2011).
26. S. Maleki, S. K. Kamrava, D. Sharifi, M. Jalessi, A. Asghari, S. Ghalehbaghi, and P. Yazdanifard, "Effect of local irradiation with 630 and 860 nm low-level lasers on tympanic membrane perforation repair in guinea pigs," The Journal of Laryngology & Otology 127(3), 260–264 (2013).
27. A. N. Pereira, C. de P. Eduardo, E. Matson, and M. M. Marques, "Effect of low-power laser irradiation on cell growth and procollagen synthesis of cultured fibroblasts," Lasers in Surgery and Medicine 31(4), 263–267 (2002).
28. E. N. Sobol, T. E. Milner, A. B. Shekhter, O. I. Baum, A. E. Guller, N. Yu. Ignatieva, and V. V. Lunin, "Laser reshaping and regeneration of cartilage," Laser Physics Letters 4(7), 488–502 (2007).

29. R. K. Chailahyan, Y. V. Gerasimov, A. P. Sviridov, A. V. Kondjurin, A. H. Tambiev, and V. N. Bagratishvili, "Effect of IR laser radiation on the multipotent mesenchymal stromal stem cells of rat marrow *in vivo*," Russian Journal of Immunology 3(3–4), 333–337 (2009). [in Russian]
30. R. K. Chailakhyan, A. G. Grosheva, N. N. Vorob'eva, A. P. Sviridov, and V. I. Yusupov, "Laser thermo-photobiomodulation of bone marrow mesenchymal stem cells," Bulletin of Experimental Biology and Medicine 174(4), 523–526 (2023).
31. R. Chailakhyan, A. Grosheva, N. Vorobieva, V. Yusupov, and A. Sviridov, "Combined light and thermal stimulation of bone marrow stem cells," Journal of Lasers in Medical Sciences 15, e8 (2024).
32. O. I. Baum, "Temperature control system for laser reshaping of nasal septum," Journal of Instrument Engineering 58(10), 847–854 (2015). [in Russian]
33. T. Zahnert, K. B. Hüttenbrink, D. Mürbe, and M. Bornitz, "Experimental investigations of the use of cartilage in tympanic membrane reconstruction," Otology & Neurotology 21(3), 322–328 (2000).
34. A. A. Aarnisalo, J. T. Cheng, M. E. Ravicz, and J. J. Rosowski, "Middle ear mechanics of cartilage tympanoplasty evaluated by laser holography and vibrometry," Otology & Neurotology 30(8), 1209–1214 (2009).
35. C. F. Lee, J. H. Chen, Y. F. Chou, L. P. Hsu, P. R. Chen, and T. C. Liu, "Optimal graft thickness for different sizes of tympanic membrane perforation in cartilage myringoplasty: a finite element analysis," The Laryngoscope 117(4), 725–730 (2007).
36. D. Mürbe, T. Zahnert, M. Bornitz, and K. B. Hüttenbrink, "Acoustic properties of different cartilage reconstruction techniques of the tympanic membrane," The Laryngoscope 112(10), 1769–1776 (2002).
37. A. Y. Wang, Y. Shen, J. T. Wang, P. L. Friedland, M. D. Atlas, and R. J. Dilley, "Animal models of chronic tympanic membrane perforation: a 'time-out' to review evidence and standardize design," International Journal of Pediatric Otorhinolaryngology 78(12), 2048–2055 (2014).
38. P. A. Vrettakos, S. P. Dear, and J. C. Saunders, "Middle ear structure in the chinchilla: a quantitative study," American Journal of Otolaryngology 9(2), 58–67 (1988).
39. P. L. Santa Maria, M. D. Atlas, and R. Ghassemifar, "Chronic tympanic membrane perforation: a better animal model is needed," Wound Repair and Regeneration 15(4), 450–458 (2007).
40. D. Bularda, R. Șerban, C. Butnaru, M. Mareș, L. C. Burtan, L. Rădulescu, and C. Mârțu, "Searching for a better animal model for chronic tympanic membrane perforation," Journal of Personalized Medicine 14(5), 513 (2024).
41. N. H. Shomer, K. H. Allen-Worthington, D. L. Hickman, M. Jonnalagadda, J. T. Newsome, A. R. Slate, H. Valentine, A. M. Williams, and M. Wilkinson, "Review of rodent euthanasia methods," Journal of the American Association for Laboratory Animal Science 59(3), 242–253 (2020).